



**HAL**  
open science

## Fluid circulation along an oceanic detachment fault: insights from fluid inclusions in silicified brecciated fault rocks (Mid-Atlantic Ridge at 13°20'N)

Anne Verlaguet, D. Bonnemains, C. Mével, J. Escartin, M. Andreani, F.  
Bourdelle, M-C Boiron, V. Chavagnac

### ► To cite this version:

Anne Verlaguet, D. Bonnemains, C. Mével, J. Escartin, M. Andreani, et al.. Fluid circulation along an oceanic detachment fault: insights from fluid inclusions in silicified brecciated fault rocks (Mid-Atlantic Ridge at 13°20'N). *Geochemistry, Geophysics, Geosystems*, 2021, 22 (1), 10.1029/2020GC009235 . hal-03152490

**HAL Id: hal-03152490**

<https://hal.sorbonne-universite.fr/hal-03152490v1>

Submitted on 25 Feb 2021

**HAL** is a multi-disciplinary open access archive for the deposit and dissemination of scientific research documents, whether they are published or not. The documents may come from teaching and research institutions in France or abroad, or from public or private research centers.

L'archive ouverte pluridisciplinaire **HAL**, est destinée au dépôt et à la diffusion de documents scientifiques de niveau recherche, publiés ou non, émanant des établissements d'enseignement et de recherche français ou étrangers, des laboratoires publics ou privés.

1           **Fluid circulation along an oceanic detachment fault: insights from fluid**  
2           **inclusions in silicified brecciated fault rocks (Mid-Atlantic Ridge at 13°20'N)**

3  
4           A. Verlaquet<sup>1\*</sup>, D. Bonnemaïn<sup>2</sup>, C. Mével<sup>2</sup>, J. Escartín<sup>2,3</sup>, M. Andreani<sup>4</sup>, F.  
5           Bourdelle<sup>5</sup>, M-C. Boiron<sup>6</sup>, V. Chavagnac<sup>7</sup>

6  
7           <sup>1</sup> Sorbonne Université, CNRS-INSU, Institut des Sciences de la Terre, IStEP UMR 7193, F 75005 Paris,  
8           France

9           <sup>2</sup> Marine Geosciences Group, IPGP CNRS UMR 7154, Paris, France

10           <sup>3</sup> Laboratoire de Géologie, UMR 8538, Paris, France

11           <sup>4</sup> Laboratoire de Géologie, Université de Lyon, Lyon, France

12           <sup>5</sup> Univ. Lille, IMT Lille Douai, Univ. Artois, Yncrea Hauts-de-France, ULR 4515 - LGCgE,  
13           Laboratoire de Génie Civil et géo-Environnement, F-59000 Lille, France

14           <sup>6</sup> Université de Lorraine, CNRS, GeoRessources, F-54000 Nancy, France

15           <sup>7</sup> Géosciences Environnement Toulouse (GET), Université Paul Sabatier Toulouse 3, CNRS UMR 5563,  
16           IRD, Toulouse, France

17  
18  
19           \* Corresponding author: [anne.verlaquet@sorbonne-universite.fr](mailto:anne.verlaquet@sorbonne-universite.fr)

20  
21  
22           **Keypoints**

- 23           • MAR 13°20'N corrugated detachment fault is composed of pervasively silicified mafic  
24           breccias overlapped from hangingwall diabases
- 25           • Quartz fluid inclusions record mixing of hangingwall silica-rich brines with footwall  
26           serpentinite-derived fluids (H<sub>2</sub>+CH<sub>4</sub>) in detachment
- 27           • This heterogeneous fluid circulation in shallow detachment fault is inconsistent with  
28           models of detachments channeling deep fluid flow

30 **Abstract**

31 The MAR 13°20'N corrugated detachment fault is composed of pervasively silicified mafic  
32 cataclastic breccias, instead of ultramafics and gabbros commonly found at other detachments.  
33 These breccias record overplating of hangingwall diabases, with syntectonic silicification due to  
34 important influx of silica-iron-rich fluids, able to leach alkalis and calcium. Fluids trapped in quartz  
35 inclusions show important salinity variations (2.1-10 wt.% NaCl eq.) indicating supercritical phase  
36 separation. Fluid inclusions also contain minor amounts of  $H_2 \pm CO_2 \pm CH_4 \pm H_2S$ , with high  $H_2/CO_2$   
37 and  $H_2/H_2S$  ratios, signatures typical of ultramafic-hosted vent fluids. We propose that seawater  
38 infiltrated the hangingwall upper crust at the axis adjacent to the active detachment, reaching a  
39 reaction zone at the dyke complex base (~2 km). At >500°C, fluids become Si-rich during diabase  
40 alteration (amphibolite-facies alteration in clasts), and undergo phase-separation. Brines,  
41 preferentially released in the nearby detachment fault during diabase brecciation, mix with  
42 serpentinite-derived fluids bearing  $H_2$  and  $CH_4$ . Cooling during detachment deformation and fluid  
43 upward migration triggers silica precipitation at greenschist-facies conditions (quartz+Fe-rich-  
44 chlorite+pyrite). Important variations in fluid inclusion salinity and gas composition at both sample  
45 and grain scales record heterogeneous fluid circulation at small spatial and short temporal scales.  
46 This heterogeneous fluid circulation operating at <2 km depth, extending both along-axis and over  
47 time, is inconsistent with models of fluids channeled along detachments from heat sources at the  
48 base of the crust at the fault root. Present-day venting at detachment footwall, including Irinovskoe,  
49 is instead likely underlain by fluid circulation within the footwall, with outflow crossing the  
50 inactive detachment fault near-surface.

51

52 **Keywords**

53 MAR 13°20'N, silicified detachment, fluid inclusions, mafic breccias, phase separation,  
54 hangingwall overplating

55

56

57

58

59 **Plain language summary**

60 Here we present constraints on fluid circulation along the 13°20'N oceanic detachment fault  
61 along the Mid-Atlantic Ridge. Rocks recovered in situ with a deep-sea robot yield mafic breccias,  
62 instead of serpentinized mantle rocks commonly found at other detachments. They likely originate  
63 from the base of the hangingwall dyke complex, brecciated during fault exhumation. These rocks  
64 are intensely silicified (quartz mineralization), resulting from upflow circulation of silica-rich  
65 fluids derived from reactions with mafic rocks in a reaction zone. Fluid inclusion (micrometric  
66 cavities in quartz crystals that trapped circulating fluid) analyses reveal highly-saline fluids likely  
67 formed by phase separation, while traces of hydrogen and methane likely record serpentinization.  
68 We thus propose that seawater infiltrated the crust down to a reaction zone at its base (2 km depth),  
69 where it became silica-rich by rock hydrothermal alteration. Upon brecciation, these silica-rich  
70 brines were released in the detachment where they mixed with fluids coming from footwall rock  
71 alteration. Temperature and pressure drops during fluid upflow promoted intense quartz  
72 crystallization. The active Irinovskoe hydrothermal site, sitting on the detachment fault ~5 km off-  
73 axis, is unrelated to fluid circulation in the detachment plane, and likely linked to a heat source  
74 within the footwall and directly below it.

## 75      **1. Introduction**

76      Low-angle detachment faults are common along slow- and ultra-slow spreading ridges, forming  
77 primarily at ridge sections with reduced melt supply (Buck et al., 2005; Cannat et al., 2006; Escartín  
78 et al., 2008; Tucholke et al., 2008). Rooting deep below the rift valley floor, detachments can  
79 operate over long periods of time (up to a few Myrs), exhume deep-seated materials from the  
80 oceanic lithosphere, and lead to the formation of oceanic core complexes (OCCs). OCCs are often  
81 capped by a fault surface displaying corrugations parallel to spreading. Ridge sections hosting  
82 OCCs tend to be associated with high seismicity rates relative to magma-rich, symmetrical ridge  
83 sections, and often display active hydrothermal venting (Escartín et al., 2008; Son et al., 2014).  
84 The microseismicity along the Northern Atlantic and the Southwest Indian Ridge detachments  
85 (deMartin et al., 2007; Parnell-Turner et al., 2017; Tao et al., 2020) reaches sub-Moho depths  
86 (between ~8 and ~13 km bsf). These results suggest that detachments are associated to a thick  
87 lithosphere, and that brittle deformation may provide potential pathways for fluid circulation  
88 reaching deep levels. Indeed, fault zone rocks from various OCCs along the MAR display evidence  
89 for fluid-rock interactions coeval with deformation. In most cases, the fault zone is characterized  
90 by deformed ultramafics and gabbros recrystallized into talcschists and amphibolites, respectively  
91 (Boschi et al., 2006; Escartín et al., 2003, 2017; Karson et al., 2006; MacLeod et al., 2002; McCaig  
92 et al., 2007; Schroeder & John, 2004). Moreover, active hydrothermal fields are often found on the  
93 OCC surface, with hydrothermal circulation crosscutting pre-existing and/or inactive fault zones,  
94 as observed at Rainbow (Andreani et al., 2014), Ashadze (Ondréas et al., 2012), Logatchev  
95 (Petersen et al., 2009), Lost City (Fruh-Green et al., 2003) or Von Damm (Hogkinson et al., 2015).  
96 To date, however, there is still limited information regarding fluid sources and pathways along the  
97 detachment fault zone at depth, the location and nature of heat sources animating this hydrothermal  
98 circulation, and the possible links between the hydrothermal activity observed at the surface of  
99 these OCCs and the flow along the detachment.

100      The 13°20'N detachment fault, located on the western flank of the Mid-Atlantic Ridge (MAR),  
101 exposes a structurally continuous and corrugated detachment fault surface (e.g, Escartín et al.,  
102 2017; MacLeod et al., 2009; Smith et al., 2006). While morphology is similar to OCCs elsewhere  
103 (Parnell-Turner et al., 2018), sampling of the detachment fault zone reveals unique characteristics.  
104 Indeed, while other detachment faults are composed of deformed and hydrated footwall ultramafics  
105 and gabbros (Boschi et al. 2006; Escartín et al., 2003, 2016; Karson et al., 2006; MacLeod et al.,

106 2002; McCaig et al., 2007; Schroeder & John, 2004), the well-preserved and corrugated 13°20'N  
107 detachment fault zone is composed essentially of highly silicified mafic cataclastic breccias  
108 (Bonnemains et al., 2017; Escartín et al., 2017). These silicified fault breccias likely result from  
109 the overplating of mafic material from the base of the hangingwall dyke complex into the footwall  
110 during fault exhumation (Bonnemains et al., 2017); these rock types have not been reported from  
111 any other studied OCC. The silicified fault zone is ~70 m or thicker, and the mechanisms of strain  
112 localization and fault development leading to a corrugated structure seem to operate independently  
113 of lithologies within the fault zone (e.g., Parnell-Turner et al., 2018). Fault zone silicification is  
114 evidenced by massive quartz precipitation that may result from elevated fluxes of silica-rich fluids,  
115 possibly syntectonic (Bonnemains et al., 2017). This detachment fault surface also hosts the active  
116 Irinovskoe hydrothermal site, where several black smokers discharge high temperature fluids  
117 (Escartín et al., 2017; MacLeod et al., 2009).

118 The 13°20'N silicified fault rocks, and the fluid inclusions trapped in quartz crystals, provide a  
119 unique opportunity to investigate the nature, sources and pathways of fluids circulating within an  
120 active detachment fault zone, and to compare them to fluid circulation feeding the active footwall  
121 Irinovskoe hydrothermal site. Indeed, to date geochemical and fluid inclusion studies have been  
122 conducted on hydrothermally altered rocks from both hangingwall (e.g., Delaney et al., 1987;  
123 Humphris et al., 1998; McCaig et al., 2007, 2010; Tivey et al., 1998; Vanko et al., 2004) and  
124 footwall of detachments (e.g., Andreani et al., 2014; Boschi et al., 2006; Castelain et al., 2014).  
125 However, in these either the link to detachment fault deformation is not established, or the  
126 associated hydrothermal systems post-date detachment activity, as in active and inactive systems  
127 preserved at the footwall of oceanic detachments (e.g., Andreani et al., 2014; Escartín et al., 2017;  
128 Hodgkinson et al., 2015; Ondréas et al., 2012). Thus, studies addressing syntectonic fluid flow at  
129 detachments are scarce, and rely on geochemical data from rock samples, (e.g., McCaig et al.,  
130 2007, 2010), not from fluids.

131 To constrain fluid-rock interactions within an active detachment fault zone, here we present a  
132 study of fluid inclusions trapped in quartz crystals from silicified fault rocks of the 13°20'N OCC.  
133 A microthermometric study was conducted on >100 fluid inclusions from four representative fault  
134 rock samples collected *in situ* at different outcrops throughout the 13°20'N fault zone, and with  
135 varying degrees of silicification. Fluid inclusion composition was also investigated by Raman  
136 spectroscopy. Whole-rock geochemical analyses were performed to constrain nature and

137 composition of the host rocks, and chlorite analyses to constrain the temperature of quartz-chlorite  
138 crystallization. With these results and available geological constraints, we propose a model of  
139 hydrothermal fluid circulation within an active oceanic detachment fault.

140

## 141 **2. Geological background of 13°20'N OCC and sampling**

### 142 **2.1. Geological setting**

143 The 13°20'N oceanic detachment displays a structurally continuous fault surface with prominent  
144 extension-parallel corrugations, exposed at the seafloor, and that roots at the rift valley floor. This  
145 OCC develops on the western flank of the MAR, which spreads at a full rate of 24.6 mm/yr  
146 (MacLeod et al., 2009; Smith et al., 2008), and is likely active based on its morphology, the absence  
147 of late tectonic disruption (Escartín et al., 2017; MacLeod et al., 2009; Mallows & Searle, 2012),  
148 and seismic activity. Microseismicity defines a curved fault plane reaching >10 km below the ridge  
149 axis (Parnell-Turner et al., 2017), reminiscent of that of other detachments such as TAG (deMartin  
150 et al., 2007) or Longqi (Tao et al., 2020). This OCC and its detachment fault were extensively  
151 investigated and sampled during the ODEMAR cruise, using deep-sea vehicles  
152 (<http://www.doi.org/10.17600/13030070>). Main cruise results, geological context, details of fault  
153 rocks are provided elsewhere (Escartín et al., 2017; Bonnemains et al., 2017).

154 The exposed, corrugated detachment fault extends ~7 km in the spreading direction (East-West),  
155 and ~5.5 km perpendicular to the extension (North-South), respectively (Figure 1a; Olive et al.,  
156 2019). The microbathymetric corrugations (Figure 1b) have a relief of up to ~10-20 m, and along-  
157 extension lengths of a few hundred meters to a maximum of 2 km (Parnell-Turner et al., 2018).  
158 While the detachment fault surface is heavily blanketed by sediment and rubble, fault planes crop  
159 out on the flank of these corrugations, showing subhorizontal striations parallel to extension  
160 (Escartín et al., 2017). During the ODEMAR cruise, in situ fault rocks were sampled at seven  
161 outcrops distributed both along- and across-extension throughout the corrugated detachment fault  
162 surface (see numbered circles in Figure 1b). Among these outcrops, Outcrop #1 (Figure 1b) was in  
163 a ~70 m deep structural low within the detachment fault surface, which shows corrugations  
164 throughout. From these observations it was inferred that the fault zone is composed of  
165 anastomosing fault planes developing over a thickness of ~70 m or more (Bonnemains et al., 2017;  
166 Escartín et al., 2017; Parnell-Turner et al., 2018).

167 The activity of the Irinovskoe hydrothermal field was confirmed during the ODEMAR cruise  
168 (Escartín et al., 2017), ~1.8 km from the footwall cutoff (black circle in Figure 1b), at a location  
169 where samples of sulfides indicated recent or active hydrothermalism (Cherkashev et al., 2013;  
170 MacLeod et al., 2009; Pertsev et al., 2012). This site displays two black smoker vents at the summit  
171 of hydrothermal mounds (Active Pot and Pinnacle Ridge) venting fluids at ~365°C, in addition to  
172 several inactive mounds and chimneys (Escartín et al., 2017).

173

## 174 **2.2. Detachment fault rocks: lithology and silicification**

175 A total of 36 fault rocks were recovered in situ from the seven outcrops throughout the 13°20'N  
176 corrugated detachment fault using ROV Victor 6000, and are described in detail by Bonnemains et  
177 al. (2017). All the rocks are cataclastic breccias, with significant heterogeneity in clast abundance  
178 and size, and clast/matrix ratios, even at sample-scale (Figure 2). Most breccias contain solely  
179 mafic clasts (basalt/diabase; Figure 2a-d), and only 2 of the 36 samples display a mixed lithology,  
180 with coexisting mafic and ultramafic clasts (see Figures 1b and 2e-f). Several fault rock samples  
181 display highly localized deformation with striated slip plane surfaces (Figures 2c-e), as well as  
182 complex internal deformation textures, with cataclastic slip zones. Textures record, at the sample  
183 scale, several phases of both localized and distributed, penetrative deformation (Bonnemains et al.,  
184 2017).

185 Fault rocks are variably silicified indicating that (1) silica-rich fluids percolated through the fault  
186 rocks, and that (2) this silicification (and associated fluid flow) was likely heterogeneous at small  
187 spatial (outcrop) scale (Bonnemains et al., 2017). Moderately silicified mafic samples are clast-  
188 supported breccias, and contain clasts of hydrothermally altered mafic rocks with still identifiable  
189 magmatic textures. Most clasts display a relatively coarse doleritic texture underlined by fresh  
190 plagioclase laths (Figure 3b; see Bonnemains et al., 2017 for additional micrographs) indicating a  
191 diabase protolith. We have identified a single sample with a clast showing vesicular texture,  
192 corresponding to extrusive basalt (Figure 3a). Hence, the bulk of the fault material is incorporated  
193 from a dyke complex (Bonnemains et al., 2017), with limited reworking of shallow basalts, and  
194 consistent with an efficient exhumation (Olive et al., 2019).

195 The least silicified diabase clasts show rare relict clinopyroxene, largely replaced by amphibole  
196 of hornblende composition, associated to fresh plagioclase of labradorite composition, and no



197 associated chlorite (detailed mineral compositions in Bonnemains et al., 2017). This secondary  
198 mineral assemblage thus records hydrothermal recrystallization initiated under amphibolite facies  
199 conditions ( $\geq 500$  °C). With increasing silicification, amphibole in clasts turns to actinolite,  
200 plagioclase becomes more albitic while chlorite crystallizes in clasts too, indicating greenschist  
201 facies conditions ( $\sim 300$ °- $500$  °C). Clasts in these low to moderately silicified samples are  
202 surrounded by a matrix of finely crushed material, with newly formed chlorite and scattered quartz  
203 grains ( $<10$  vol.% quartz). Highly silicified mafic samples are matrix-supported breccias with  
204 highly recrystallized clasts whose primary texture is largely obliterated. These breccia clasts are  
205 made up almost exclusively of chlorite and quartz, and are surrounded by a quartz-dominated ( $>90$   
206 vol.% quartz) matrix that also contains chlorite. Of the two samples bearing ultramafic clasts, only  
207 one has been silicified. Abundant sulfides associated with quartz are found in three silicified fault  
208 rocks.

209 Cathodoluminescence imaging of selected samples also shows that quartz grains record  
210 successive fracturing and recrystallization episodes (Bonnemains et al., 2017), thus consistent with  
211 syntectonic quartz crystallization. Silicification and chloritization are closely associated during the  
212 alteration of the  $13^{\circ}20'N$  detachment fault mafic breccias. Indeed, chlorite is absent from the  
213 freshest diabase clasts (Bonnemains et al., 2017), chlorite content is low in moderately silicified  
214 samples and increases significantly with degree of silicification. Chlorite crystals imbricate quartz  
215 ones, or are included within quartz crystals, demonstrating co-crystallization in both clasts and  
216 matrix. Coeval quartz and chlorite crystallization is also unequivocal within late chlorite-filled  
217 veins crosscutting mafic samples. Thus, these microtextures record coeval formation of both  
218 minerals during detachment exhumation, and indicate that silicification occurred at greenschist-  
219 facies conditions (Bonnemains et al., 2017).

220

### 221 **2.3. Samples selected for fluid inclusion and geochemical study**

222 This study is based on a set of 6 representative detachment fault rocks that have been selected  
223 in order to (1) obtain a spatial coverage throughout the  $13^{\circ}20'N$  corrugated surface, and (2) cover  
224 various degrees of alteration and silicification (Table 1; Figure 1). These rocks were sampled in  
225 situ from five fault surface outcrops that are described in detail by Bonnemains et al. (2017; Figure  
226 1b). All silicified samples contain abundant albeit very small fluid inclusions in quartz crystals.

227 Fluid inclusions suitable for this study were identified in 4 samples: three variably silicified  
228 breccias with only mafic clasts (ODM195, ODM155 and ODM218), and one silicified breccia with  
229 mixed mafic-ultramafic clasts (ODM173). We benchmarked geochemical analyses with two  
230 additional unsilicified samples of mafic and mixed mafic-ultramafic material (ODM115 and  
231 ODM217, respectively). Sample texture and mineralogy are summarized in Table 1. These samples  
232 are heterogeneous, showing a complex history with several deformation phases (Bonnemains et  
233 al., 2017), thus subsamples were also taken in some cases at varying distances from slip surfaces,  
234 as indicated below. Furthermore, to obtain representative whole-rock chemical analyses, larger  
235 subsamples were taken for three samples (i.e., ODM218, ODM173 and ODM217), labeled wr  
236 (whole rock) in Tables 2 and S1.

237 ODM115 is a basaltic clast from an unsilicified breccia (Figure 2a). It displays a typical pillow  
238 lava microtexture, with skeletal olivine microphenocrysts, radiating dendritic plagioclase, very  
239 fine-grained clinopyroxene crystals and vesicles (Figure 3a). Vesicles are filled with chlorite, veins  
240 with epidote, and the ground mass contains chlorite and pumpellyite. This quartz-free clast of  
241 extrusive basalt is considered as a reference for mafic material incorporated into the fault zone. It  
242 is the sole unsilicified mafic sample recovered from the fault outcrops.

243 ODM195 is a moderately silicified clast-supported breccia (Figure 2b) with clasts composed of  
244 either chlorite only, or actinolite + plagioclase ± chlorite displaying relict doleritic textures (Figure  
245 3b). The matrix contains crushed sub-millimetric clast fragments surrounded by newly formed  
246 chlorite and 5-10 vol.% of quartz (Figure 3b). Anhedral quartz crystals, typically ~100 µm in  
247 length, are either scattered or in local aggregates in the matrix.

248 ODM155 and ODM218 are two highly silicified, matrix-supported fault breccias (Figures 2c-  
249 d). Both display a striated surface (slip plane) and an underlying well-developed slip zone  
250 (penetrative deformation). No primary mineral is preserved in any of the clasts, which contain  
251 either chlorite + titanite or chlorite + quartz (Figures 3c-d). Rare clasts preserve a primary doleritic  
252 texture (Figure 3c) despite pervasive alteration and mineral replacement, thus indicating a diabase  
253 protolith. Anhedral and subhedral quartz grains surrounded by interstitial chlorite represent >90  
254 vol.% of the matrix. Both samples contain abundant sulfides, ODM155 containing only pyrite,  
255 whereas ODM218 contains pyrite with minor pyrrhotite and chalcopyrite.

256 Three subsamples were taken from ODM218, at varying distance from the slip surface, to  
257 investigate relationships between sample geochemistry and distance to slip planes, which may act  
258 as preferential fluid flow zones. ODM218a is located within 1 cm from the striated slip surface  
259 (Figure 2d), and contains only rare and submillimetric sulfide grains and clasts embedded in a  
260 quartz-rich matrix. When present, clasts are mostly silicified. ODM218b is ~4-5 cm away from the  
261 slip plane, and displays clasts either silicified or quartz-free up to 1 cm in size, in addition to  
262 disseminated quartz grains in the matrix. ODM218c is a fragment dislodged from the lower surface  
263 of the sample and away (~12 cm) from the slip plane, and contains quartz-free clasts surrounded  
264 by a silicified matrix with sulfides. In this set of samples, matrix quartz grain sizes increase with  
265 the distance to the slip plane, and thus ODM218c contains the largest matrix quartz grains.

266 ODM217 is a quartz-free, brecciated talc-amphibole schist displaying a slip surface on one side  
267 and several internal slip zones (Figure 2e). Clasts are either made up of talc and amphibole or  
268 chlorite  $\pm$  titanite (Figure 3e). Matrix mineralogy varies among slip zones, and is made of talc,  
269 serpentine or chlorite (Figure 3e), with disseminated spinels. To account for sample heterogeneity,  
270 two subsamples were taken (Figure 2e). Subsample ODM217a is a chlorite-rich slip zone adjacent  
271 to a striated slip surface, whereas subsample ODM217b is a talc-rich zone a few cm away from  
272 this same slip surface. For whole-rock geochemical analyses, we thus consider the unsilicified  
273 breccia ODM217 as a reference, as it contains both ultramafic and mafic clasts.

274 ODM173 is a matrix-supported breccia (Figure 2f) containing both mafic and ultramafic clasts,  
275 made of talc or chlorite  $\pm$  titanite (Figure 3f). The matrix is made of chlorite and talc, with variable  
276 amounts of quartz at the sample scale, and scattered spinel and sulfides (chalcopyrite + pyrite;  
277 Figure 3f). As for ODM217, we selected two sub-samples to investigate this heterogeneity.  
278 ODM173a displays few small clasts (< 1 mm) surrounded by a silicified matrix made of chlorite  
279 and talc associated with anhedral quartz crystals (<60 vol.% quartz, Figure 3f), whereas clasts in  
280 ODM173b are more abundant and larger (up to 1-2 cm), with only rare quartz grains and minor  
281 chlorite in the matrix. Sulfides are more abundant in ODM173b than in ODM173a.

282

### 283 **3. Methods**

284 To investigate the composition of fluids circulating through the detachment fault zone, and that  
285 are responsible for pervasive silicification, a study of fluid inclusions trapped in quartz crystals was

286 coupled to whole-rock and mineral geochemical analyses (major and trace element). Fluid  
287 inclusion analyses included microthermometry, Raman spectroscopy, and LA-ICP-MS. We also  
288 used SEM-cathodoluminescence to study the growth history of quartz crystals hosting fluid  
289 inclusions. Microthermometric measurements of fluid inclusions determined isochoric  
290 relationships that, coupled with geologically constrained pressure intervals, provided estimates of  
291 fluid inclusion entrapment temperatures. These temperatures were then compared to silicification  
292 temperatures inferred from the composition of chlorite co-crystallized with quartz, using the  
293 geothermometer of Bourdelle et al. (2013).

294

### 295 **3.1. Whole-rock and mineral chemical analyses**

296 Whole rock chemical analyses were performed at the SARM-CRPG (Nancy, France). Major  
297 elements were analyzed by inductively coupled plasma optical emission spectroscopy (ICP-OES)  
298 after fusion with  $\text{LiBO}_3$  and dissolution in  $\text{HNO}_3$ . Trace elements were quantified by inductively  
299 coupled plasma mass spectrometry (ICP-MS) following the procedure described by Carignan et al.  
300 (2001). To account for sample heterogeneity, subsamples were analyzed for ODM218, ODM173  
301 and ODM217 (see section 2.3).

302 Major element composition of chlorite was analyzed by EPMA (CAMECA SX-FIVE,  
303 CAMPARIS, Sorbonne Université, Paris, France). Analytical conditions were 15 kV-10 nA in  
304 WDS mode, for analysis of major elements.  $\text{Fe}_2\text{O}_3$  (Fe),  $\text{MnTiO}_3$  (Mn, Ti), diopside (Mg, Si),  $\text{Cr}_2\text{O}_3$   
305 (Cr), orthoclase (Al, K), anorthite (Ca) and albite (Na) were used as standards for elements in  
306 parentheses. Only chlorite analysis with oxide sum in the 86-89 wt.% range and  $\text{Na}_2\text{O} + \text{K}_2\text{O} +$   
307  $\text{CaO} < 1$  wt.% were considered. Structural formulas were derived on a 14-oxygen basis. Chlorite  
308 analyses with  $\text{Si} \leq 4$  atoms per formula unit, cation sum  $\leq 10.1$  apfu and vacancies  $>0.01$  pfu were  
309 considered. In situ trace element analyses were carried out on 22 chlorites at GeoRessources  
310 (Nancy, France) using LA-ICP-MS. Technical details can be found with results in Table S3.

311

### 312 **3.2. Fluid inclusion analyses**

313 Fluid inclusions analyses were performed on 100  $\mu\text{m}$  thick double-polished sections. Successive  
314 generations of fluid inclusions trapped during quartz crystal growth were first characterized using

315 an Olympus BX-50 transmitted light microscope at IPGP. Inclusions either isolated or clustered  
316 (i.e., distant less than five times their length; Figure 4a) are considered as primary according to the  
317 criteria of Roedder (1984) and Van den Kerkhof and Hein (2001), whereas those located along  
318 trails crosscutting quartz grains are considered as secondary (Figure 4b). The location of the  
319 different generations of fluid inclusions within individual quartz crystals was compared to crystal  
320 growth history as revealed by SEM-cathodoluminescence observations (as in Boiron et al., 1992),  
321 conducted at IStEP - Sorbonne Université (Paris, France) on a Scanning Electron Microscope Zeiss  
322 Supra 55 equipped with an EDS system and an Oxford Instruments cathodoluminescence system.

323 Microthermometric fluid inclusion measurements were carried out at IStEP - Sorbonne  
324 Université under an optical microscope equipped with a Linkam THMSG 600 heating-freezing  
325 stage with temperatures ranging from -196 °C to +600 °C. The stage is controlled by a Linkam  
326 TMS 93 programmer via LinkSys software v.2.15.

327 Cycles of repeated homogenization and ice melting temperature measurements were conducted  
328 on 176 individual inclusions to measure the temperature of phase changes for the gas-to-liquid  
329 homogenization (temperature of homogenization,  $T_h$ ) and for the ice melting point (temperature of  
330 final ice melting,  $T_{m_{ice}}$ ), respectively. Several cycles performed to test reproducibility show that  
331 ice melting and homogenization temperatures were reproducible within 0.1 °C (~0.2 wt.% eq.  
332 NaCl) and 1 °C, respectively. Inclusions yielding non-reproducible measurements systematically  
333 showed complex morphologies and were thus discarded, yielding 119 fluid inclusions for this  
334 study. We performed temperature cycles in the potential range of hydrate melting temperatures,  
335 following Raimbourg et al. (2014), but no gas hydrate was detected. Salinity was estimated from  
336  $T_{m_{ice}}$  using the equation in Bodnar (1993), assuming that the entrapped fluid is a pure H<sub>2</sub>O-NaCl  
337 solution. Isochoric P-T relationships followed by fluid inclusions were derived from  $T_h$  and NaCl  
338 molality, following the equation of Zhang and Frantz (1987), suitable for our P-T and salinity  
339 range.

340 Gas content of fluid inclusions was analyzed with a Dilor-Labram Raman microspectrometer at  
341 GeoRessources (Nancy, France) on a representative set of 83 inclusions. As all studied inclusions  
342 are two-phase, we focused the laser on the gas bubble to determine gas proportions. In these  
343 dominantly aqueous inclusions, H<sub>2</sub>O vapor is by far the dominant gaseous phase. The relative molar  
344 proportions of the remaining minor gases (H<sub>2</sub>, CO<sub>2</sub>, CH<sub>4</sub>, H<sub>2</sub>S) were calculated with accuracy better

345 than 5% (Pasteris et al., 1988) following the procedure described in Dubessy et al. (1989). This  
346 involves band area integration at wavenumbers of each gas and gas specific volume, i.e., Raman  
347 scattering cross-section for each gas and instrument efficiency at the specific wavenumbers  
348 (Frezzotti et al., 2012). To subtract the air signal for N<sub>2</sub>, we conducted blank analyses in the quartz  
349 immediately adjacent to each inclusion.

350 Fluid inclusion chemical composition was analyzed on all inclusions larger than 8 μm (i.e., 24  
351 inclusions) with a LA-ICP-MS at GeoRessources (Nancy, France; see technical details in Table  
352 S3). We analyzed Na, K, Li, Mg, Fe, Mn, Cr, Co, Ni, and calculated absolute concentrations and  
353 limits of detection following Leisen et al. (2012), using Na content derived from  
354 microthermometric T<sub>m,ice</sub> measurements (and calculated salinity) as internal standard. However,  
355 due to the low signal intensity for most measured elements, it was impossible to calculate accurate  
356 fluid inclusion element concentrations; these fluid inclusions were very small, with fluid released  
357 after 1-2 laser shots, and contained low salinity fluids that are therefore very diluted in metallic  
358 elements. While Na is likely the most concentrated cation, it was systematically difficult to detect  
359 by LA-ICP-MS due to ionization problems.

360

## 361 **4. Results**

### 362 **4.1. Chemistry**

#### 363 ***4.1.1. Whole rock analyses***

364 Major element compositions and selected trace element contents for samples described in  
365 Section 2.3 are presented in Table 2 (see Table S1 for full trace element analysis). Chemical data  
366 are compared with published data of mafic and ultramafic rocks recovered at the 13°20'N OCC  
367 (Wilson et al., 2013), and at the 15°20'N Fracture Zone (Godard et al., 2008; Paulick et al., 2006),  
368 although such comparison must be done with care as 13°20'N fault rocks are breccias, and differ  
369 from those at other sites, as presented above.

370 The unsilicified basaltic fault rock clast fragment (ODM115) has a composition similar to that  
371 of MAR basalts. In silicified mafic samples, the concentration of alkalis, Ca and Al (CaO in Figure  
372 5a; Na<sub>2</sub>O and Al<sub>2</sub>O<sub>3</sub> in Figures S1a-b) decreases sharply with increasing Si content, with almost  
373 complete depletion in the highly-silicified samples ODM155 and ODM218. Mg# for basaltic

374 ODM115 and moderately silicified diabase ODM195 are in the range of MAR basalt and diabase  
375 values (Figure 5b). In contrast, Mg# clearly decreases in highly silicified samples ODM155 and  
376 ODM218 (Mg# < 45). Mixed mafic-ultramafic breccias show compositions that are intermediate  
377 between MAR mafic and ultramafic compositions, resulting from mafic and ultramafic material  
378 mixed in variable amounts (Figures 5a-b and S1a-b). As in mafic samples, CaO, Na<sub>2</sub>O and Al<sub>2</sub>O<sub>3</sub>  
379 contents, as well as Mg#, are significantly lower in the silicified sample ODM173 compared to  
380 unsilicified ODM217 (Figures 5a-b and S1a-b). Their SiO<sub>2</sub> content is higher than that of ultramafic  
381 rocks for both the silicified ODM173 and the unsilicified ODM217, which is talc-rich.

382 Cr and Ni concentrations (Figure 5c) in most mafic samples are similar to those of MAR basalts  
383 and diabases, with subsample ODM218b showing slightly higher contents in both Cr and Ni. For  
384 the two samples with both mafic and ultramafic clasts, Cr and Ni contents are intermediate between  
385 those of MAR mafic and ultramafic compositions, reflecting again their mixed lithologies. The  
386 REE patterns (Figure S1c) for all mafic breccias are flat, as observed for MAR basalt and diabase  
387 patterns (Wilson et al., 2013). While the unsilicified basaltic clast ODM115 displays REE-  
388 normalized values consistent with those of MAR mafic rocks, REE concentrations progressively  
389 decrease as silicification increases, but without any pattern modification, likely due to dilution by  
390 quartz crystallization. The two mafic-ultramafic fault rocks display REE patterns between those of  
391 mafic and ultramafic signatures, reflecting their mixed lithologies (Figure S1c).

392 Hence, bulk rock analyses reflect significant heterogeneity of breccia samples, controlled by  
393 both the degree of silicification and the nature of the clasts. However, such analysis only reveals  
394 relative elemental enrichment or depletion. We combine these chemical analyses to textural and  
395 mineralogical observations to constrain effective mass transfer, and to determine if silicification  
396 resulted from significant silica enrichment only, or was associated to efficient leaching of other  
397 elements. Several arguments indicate massive silica influx rather than an important leaching: (1)  
398 dilution effect observed for most trace elements (Figure S1c), (2) preferential preservation of initial  
399 textures with well-defined clast borders, which would have been erased by massive leaching, (3)  
400 the fact that the most silicified breccias are matrix supported (while less silicified ones are clast-  
401 supported), and (4) the preferential crystallization of quartz in the matrix. However, calcium and  
402 alkalis (and part of the aluminum) were almost completely leached from silicified mafic and mixed  
403 mafic-ultramafic samples, and this important decrease with increasing silicification cannot be  
404 explained solely by passive depletion due to quartz crystallization (grey arrows, Figures 5a and

405 S1a-b). Almost complete alkali leaching is also supported by mineralogical composition of all  
406 mafic fault rocks from the seven outcrops (Bonnemains et al., 2017). Indeed, highly silicified  
407 samples contain mainly chlorite and quartz, lacking mineral phases able to host alkalis (i.e., no  
408 plagioclase or amphibole in highly silicified samples ODM218 and ODM155). The decrease in  
409 Mg# for silicified samples (ODM155, ODM218 and ODM173) compared to unsilicified ones  
410 likely reflects iron enrichment, as Mg# would be unaffected by quartz crystallization (Figure 5b).  
411 This is supported by the growth of iron-rich sulfides, essentially pyrite, as confirmed by the low  
412 Cu and Zn content (Table 2).

413

#### 414 ***4.1.2. Chlorite composition***

415 Microprobe analyses show that chlorites from both mafic and mixed mafic-ultramafic samples  
416 contain 40-50 wt.% of FeO+MgO, 30-40 wt.% SiO<sub>2</sub> and 15-25 wt.% Al<sub>2</sub>O<sub>3</sub> (Figure 6a). There is  
417 no systematic difference in chlorite composition between clasts and matrix for each sample (Figure  
418 6a). Chlorites in moderately silicified ODM195 show slightly lower FeO+MgO and higher SiO<sub>2</sub>  
419 contents than highly silicified ODM218, while chlorite composition of highly silicified ODM155  
420 overlaps both samples.

421 Chlorites contain Si apfu in the range 2.7-3.5, Al apfu is 1.5-2.6 and Mg# between 43 and 85  
422 (Table S2). While Si and Al contents are clearly anticorrelated for all chlorites, Si content and Mg#  
423 are roughly correlated in each sample, although more scattered (Figure 6b). The unsilicified basalt  
424 sample (ODM115) has chlorite compositions similar to those from MAR basalts (Alt et al., 1985;  
425 Gillis & Thompson, 1993; Humphris & Thompson, 1978). Chlorite composition in moderately  
426 silicified breccia (ODM195), in both clast and matrix, is comparable to that in diabases  
427 (amphibolite facies; Castelain et al., 2014; Escartín et al., 2003; Figure 6b). For highly silicified  
428 samples (ODM155 and ODM218), chlorites clearly have a lower Mg# compared to ODM195, with  
429 a wider range (about 80-40), although most of them remain comparable to oceanic basalt chlorites  
430 (Figure 6b). Increasing silicification is obviously associated with iron enrichment and silica  
431 depletion in chlorites, a trend also observed by Saccocia and Gillis (1995) and Delaney et al. (1987)  
432 in the MARK area, and by Castelain et al. (2014) in diabase chlorite-quartz veins at the footwall  
433 of the Atlantis Massif detachment (Figure 6b). Indeed, iron-rich chlorites have been described in  
434 oceanic hydrothermal breccias and quartz veins associated with the dyke complex or the dyke-lava



435 transition (Alt et al., 1985; Delaney et al., 1987; Honorez et al., 1998; Humphris et al., 1998; Mottl,  
436 1983; Saccocia & Gillis, 1995).

437 Concerning mixed mafic-ultramafic breccias, chlorites from the unsilicified sample ODM217  
438 show the highest Mg# at ~80. This is expected in rocks containing fragments of ultramafic rocks,  
439 and are mostly comparable to chlorites from other oceanic detachment talcschists and amphibolite  
440 schists (e.g., 15°45'N, Escartín et al., 2003; South Atlantis massif, Boschi et al., 2006; Figure 6b).  
441 Mg# for chlorites in the silicified mixed breccia (ODM173) presents a broader range and lower  
442 values (Mg#~50-80) than those of talcschists (Mg#~80, Figure 6b), similar to the decrease in Mg#  
443 and Si with increasing silicification observed for mafic samples.

444 Concerning trace elements, chlorites from mixed mafic-ultramafic fault rocks are generally  
445 enriched in Cr, Ni, Co, but depleted in Ti, V, Mn compared to chlorites from mafic breccias (Tables  
446 S2 and S3), in line with literature data (e.g., chlorites from diabases and talcschists, Boschi et al.,  
447 2006; Escartín et al., 2003). We note that a few chlorites from highly silicified mafic samples  
448 (ODM155 and ODM218) also show enrichments in Cr, Co, and slight enrichments in Ni (Tables  
449 S2 and S3).

450

#### 451 ***4.1.3. Calculated temperature of chlorite formation***

452 Several chlorite thermometers exist in the literature, based on empirical, semi-empirical, or  
453 thermodynamic approaches. Empirical thermometers cannot be used here as their application is  
454 restricted to the chlorite compositional space used for their calibration (Bourdelle & Cathelineau,  
455 2015). Furthermore, their applicability is questionable as they only consider one substitution, do  
456 not take into account the bulk rock composition, and have no thermodynamic basis (Bourdelle &  
457 Cathelineau, 2015). Thermobarometric models (e.g., Vidal & Parra, 2000; Vidal et al., 2001, 2005,  
458 2006; Walshe, 1986), widely used in metamorphic environments, lack of thermodynamic data for  
459 the Si-rich Al-free chlorite end-member (Figure 6c), therefore precluding their use for our samples.  
460 Indeed, chlorites formed in the fault breccias (Figures 6b-c) have a relatively high Si content (2.7-  
461 3.5 apfu) and some chlorites plot in the clinocllore-sudoite-Al-free chlorite field (Figure 6c). We  
462 thus used the semi-empirical geothermometer of Bourdelle et al. (2013), suitable for all  
463 compositions of chlorite in equilibrium with quartz. This choice is also comforted by the quartz

464 and chlorite co-crystallization in both matrix and clasts during silicification (see 2.2 and  
465 Bonnemains et al., 2017).

466 The geothermometer of Bourdelle et al. (2013) is specifically calibrated for low-temperature  
467 contexts (i.e.,  $T < 350$  °C), through a linear equation linking the chlorite + quartz equilibrium  
468 constant to the temperature of crystallization, taking into account cationic substitutions involving  
469 Si and  $R^{2+}$  contents. For higher-grade contexts, several thermodynamic parameters (as the non-  
470 ideal contribution of the site mixing) cannot be linearized, and a quadratic correction (Bourdelle et  
471 al., 2013) is proposed instead (“Tcorrected” in Table S2). While these “Tcorrected” results should  
472 be cautiously considered (Bourdelle et al., 2013), this involves a small portion of our analyses.

473 Temperatures obtained with this thermometer mostly span the 150-400 °C range (except for a  
474 few outliers which are not considered). We find median temperatures of ~250 °C for the moderately  
475 silicified samples ODM173 and ODM195, and ~275 and ~300 °C for the highly silicified samples  
476 ODM155 and ODM218 respectively (Figure 6d; Tables S2 and S4).

477

## 478 **4.2. Fluid inclusion results**

### 479 ***4.2.1. Distribution and morphology of fluid inclusions***

480 Fluid inclusions are common in quartz from the 13°20'N detachment fault rocks. Those in quartz  
481 crystals from clasts in highly silicified breccias are bigger and better preserved than those in quartz  
482 grains within the matrix, which shows abundant decrepitated inclusions. All inclusions contain  
483 aqueous fluid that is two-phase (liquid-vapor; Figure 4) at room temperature, with a vapor to total  
484 volume ratio ranging from 0.1 to 0.5 (Figure S2). In quartz grains distant from slip planes (>1 cm),  
485 fluid inclusions are abundant and mostly range in size from 8 to 12  $\mu\text{m}$  (Figure 4a). The contour of  
486 primary fluid inclusions is spherical to elongated, sometimes approaching negative crystal shapes  
487 (Figures 4a, d, e, i). No sign of decrepitation (e.g., Roedder, 1984; Touret, 2001) is noticeable,  
488 except in samples within ~1 cm from a slip plane (sample ODM218a), in which inclusions are  
489 small (<5  $\mu\text{m}$ ), very irregular in shape, and often empty and probably decrepitated (e.g., Roedder,  
490 1984). Inclusions in this sub-sample ODM218a were therefore discarded for microthermometric  
491 measurements.

492 Small and elongated fluid inclusions, a few microns thick and a few tens of micron long, are  
493 regularly distributed, defining trails. Their elongation is often slightly oblique to the trail direction  
494 (Figures 4b, c, f, g, h), but their vapor ratio is similar to that of primary inclusions (Figure S2).  
495 These correspond to recrystallized microfractures, and thus postdate primary ones described above  
496 (e.g., Roedder, 1984). These trails do not show any distinct orientation, neither relative to each  
497 other nor at the sample scale (Figures 4f, g). Most of them are intra-grain trails, as they remain  
498 within the limits of quartz grains (Van den Kerkhof & Hein, 2001), with few occurrences  
499 crosscutting grain boundaries (Figures 4f, g). These trails are thus related to quartz fracturing  
500 between successive quartz crystallization episodes as revealed by SEM cathodoluminescence  
501 (Figures 7 and S3; Bonnemains et al., 2017). Therefore, this second set of inclusions can be  
502 classified as “pseudo-secondary”, following the criteria of Roedder (1984).

503

#### 504 **4.2.2. Microthermometry**

505 Ice melting temperature ( $T_{m_{ice}}$ ) measurements indicate that all inclusions, primary and  
506 secondary, contain moderately saline aqueous fluids.  $T_{m_{ice}}$  ranges from  $-6^{\circ}\text{C}$  to  $-1.5^{\circ}\text{C}$  (Figure  
507 S4), yielding equivalent salinities ranging from 2.1 to  $\sim 10$  wt.% eq. NaCl. Most fluid inclusions  
508 studied here thus have a salinity higher than that of seawater (3.2 wt.% eq. NaCl, blue line in Figure  
509 8a; Table 3) with salinity restricted to the 4–6 wt.% eq. NaCl range for all samples but ODM218,  
510 which displays a wider salinity range (2.1–10 wt.% eq. NaCl). We note that the salinity is higher  
511 for subsample ODM218b (from 6.3 to 10 wt.% eq. NaCl) than for subsample ODM218c (from 2.1  
512 to 6.1 wt.% eq. NaCl; Figure 8a).

513 Highly silicified mafic breccias (ODM155, ODM218) present higher homogenization  
514 temperatures (180–350  $^{\circ}\text{C}$ ) than moderately silicified ones, either mafic (ODM195) or mixed  
515 mafic-ultramafic (ODM173; 150–220  $^{\circ}\text{C}$ ; Figure 8a; Table 3). The highly-silicified sample  
516 ODM155 shows a wide range of  $T_h$  values, spreading over  $\sim 130^{\circ}\text{C}$ , whereas the  $T_h$  for all other  
517 samples show more restricted ranges of up to 90  $^{\circ}\text{C}$ . We do not observe any systematic difference  
518 in  $T_{m_{ice}}$  and  $T_h$  between primary and secondary fluid inclusions in any of the samples (Figure 8a).

519 Intra-grain variations of fluid inclusion  $T_h$  and salinities are shown in Figure 8b, where sets of  
520 inclusions from different quartz grains are shown with different colors. The strong variation of  $T_h$   
521 and salinity observed respectively for ODM155 and subsamples OM218b and ODM218c (highly

522 silicified mafic breccias) is thus observed not only at the sample scale, but also at the quartz grain  
523 scale (Figure 8b). SEM-cathodoluminescence observations reveal core-to-rim variations in quartz  
524 luminescence (Figures 7 and S3) that record successive steps of quartz crystallization (Bonnemains  
525 et al., 2017). The location of fluid inclusions displaying scattered microthermometric values on  
526 cathodoluminescence images (Figure 7b, d and S3b, e) suggests that fluid inclusions were trapped  
527 in quartz of varying luminescence, and thus during different quartz grain crystallization phases,  
528 between successive quartz fracturing episodes.

529

### 530 *4.2.3. Composition of fluid inclusions*

531 Fluid inclusions from the 4 fault rock samples studied here are mostly aqueous (i.e., H<sub>2</sub>O-NaCl),  
532 as shown by the absence of gas hydrate detection. Raman spectroscopy analyses of the vapor phase  
533 (i.e., gas bubble) of aqueous fluid inclusions detected minor amounts of H<sub>2</sub>, CO<sub>2</sub>, CH<sub>4</sub> and H<sub>2</sub>S (in  
534 addition to H<sub>2</sub>O) in the highly silicified mafic breccias (ODM155 and ODM218; Table 3; Figure  
535 9). Conversely, only H<sub>2</sub>O vapor was detected in the moderately silicified samples ODM173 and  
536 ODM195, although the high fluorescence observed during Raman analyzes for the latter could have  
537 hidden small gas signal.

538 In sample ODM155, only two out of 17 fluid inclusions (Table 3) were not purely aqueous and  
539 contained traces of CO<sub>2</sub>. On the other hand, 15 out of 28 inclusions from subsample ODM218b,  
540 and the 21 analyzed inclusions of ODM218c, contained traces of gases (other than H<sub>2</sub>O), and  
541 dominated by H<sub>2</sub> (up to 100 mol.% of the H<sub>2</sub>-CO<sub>2</sub>-CH<sub>4</sub>-H<sub>2</sub>S content in 18 inclusions) in addition  
542 to variable proportions of CO<sub>2</sub> (up to 80 mol.% of the H<sub>2</sub>-CO<sub>2</sub>-CH<sub>4</sub>-H<sub>2</sub>S content), CH<sub>4</sub> (up to 12  
543 mol.% of the H<sub>2</sub>-CO<sub>2</sub>-CH<sub>4</sub>-H<sub>2</sub>S content) and H<sub>2</sub>S (up to 12 mol.% of the H<sub>2</sub>-CO<sub>2</sub>-CH<sub>4</sub>-H<sub>2</sub>S content,  
544 in 4 inclusions from ODM218c; Figure 9a). All inclusions display very low H<sub>2</sub>S/H<sub>2</sub> ratios (Figure  
545 9b), similar to those measured in ultramafic-derived hydrothermal vent fluids (Fouquet et al.,  
546 2010), while mafic hosted vents rather show high H<sub>2</sub>S/H<sub>2</sub> ratios. We do not observe any correlation  
547 between gas compositions and microthermometric data (Figure S5).

548 LA-ICP-MS analyses were performed on a set of 24 fluid inclusions, but their small size  
549 precludes calculating reliable concentrations (see 3.2). K +/- Na and Li were detected in 10  
550 inclusions, and associated to the presence of Cr +/- Ni, Co, Mn, Fe, Mg in 7 of them. Despite these  
551 limitations due to inclusion sizes, inclusion fluids in the 13°20'N detachment fault rocks appear to

552 be very diluted fluids. They can thus be assimilated to fluids in the H<sub>2</sub>O-NaCl system, and hence  
553 their salinity can be estimated from the ice melting temperature (Bodnar, 1993).

554

## 555 **5. Interpretation and discussion**

### 556 **5.1. Pressure and temperature conditions of silicification**

#### 557 ***5.1.1. Pressure range deduced from the geological context***

558 Silicification occurred in the detachment plane, affecting cataclastic breccias of mainly mafic  
559 composition. Preserved doleritic textures in moderately silicified breccias indicate that these  
560 diabase rocks were part of the base of Layer 2 (dyke complex) at the hangingwall, underlying the  
561 rift valley floor, and mechanically accreted into the fault zone (Bonnemains et al., 2017).  
562 Geophysical observations along slow-spreading ridges suggest that Layer 2 thickness may vary  
563 between 1 and 2 km (see discussion in Bonnemains et al., 2017 and references therein), while a  
564 recent seismic experiment in this study area reports a Layer 2A thickness on-axis of ~2 km (Simão  
565 et al., 2020). Assuming a rift valley floor depth of ~3000 m, and considering seawater and crustal  
566 rocks densities of 1025 and 3000 kg.m<sup>-3</sup> respectively, the pressure ranges for the base of Layer 2  
567 can be estimated to 600-890 bars for lithostatic pressure, and 400-500 bars for hydrostatic pressure.  
568 Therefore, silicification and coeval fluid entrapment in quartz crystals in the detachment fault zone  
569 necessarily took place between the base of Layer 2 (400-890 bars) and the seafloor (300 bars;  
570 Figure 10).

571

#### 572 ***5.1.2. Temperature of fluid inclusion trapping during silicification***

573 Fluid inclusion isochores derived from microthermometric data (equation of Zhang & Frantz,  
574 1987) represent the P-T relationship along which fluid inclusions were trapped (Figure 10), while  
575 the measured homogenization temperature Th (Figure 8) indicates the rooting temperature of the  
576 isochore on the liquid-vapor curve (from Sourirajan & Kennedy, 1962). Intersection of fluid  
577 pressure ranges (see above) with isochores provides an estimate of the temperature range of  
578 silicification and subsequent fluid entrapment in quartz crystals (Figure 10). For samples ODM195  
579 and ODM173, temperatures of fluid entrapment are in the 160-280 °C range, while for highly  
580 silicified samples ODM155 and ODM218, entrapment temperatures are in the 200-400 °C and 275-

581 425 °C ranges respectively (Figure 10). As these fluid inclusions were trapped at various stages of  
582 quartz syntectonic crystallization (Figures 7 and S3), fluid entrapment temperatures do represent  
583 the temperature interval over which silicification occurred.

584 Significant scatter in isochores for ODM155 reflect Th variability. Indeed, ODM155 (and to  
585 a lesser extent ODM195) exhibits a broad range of homogenization temperatures (~130 °C) at both  
586 sample- and grain-scale, associated to homogeneous salinities (4-6 wt.% eq. NaCl; Figure 8). This  
587 pattern is typical of post-entrapment deformation of fluid inclusions (Roedder, 1984), and is  
588 common in most hydrothermal systems (Delaney et al., 1987; Kelley et al., 1993; Petersen et al.,  
589 1998). This result suggests that some inclusion cavities (and therefore fluid density) underwent  
590 later re-equilibration during penetrative deformation phases (i.e., slip zones and planes in both  
591 samples), slightly modifying P-T isochoric relationships (Diamond et al., 2010; Tarantola et al.,  
592 2010; 2012; Vityk & Bodnar, 1995). In contrast, ODM218 shows a very restricted Th range, thus  
593 the isochore fan rather reflects its high variation in salinity (2-10 wt.% NaCl, Figure 8) and thus in  
594 fluid density.

595

### 596 *5.1.3. Comparison with the temperature of chlorite formation*

597 The formation temperature of chlorite, which coevally crystallized with quartz in both matrix  
598 and clasts during silicification (see 2.2 and Bonnemains et al., 2017), is calculated from chlorite  
599 composition (see 4.1.3; Figure 6d; Tables S2 and S4), and is thus an independent estimate of  
600 silicification temperature. The large range of chlorite crystallization temperatures (~150-400 °C,  
601 Figure 6d) reflects continuous crystallization with quartz during breccia infiltration by  
602 hydrothermal fluids and exhumation towards progressively lower P-T conditions in the detachment  
603 plane. The temperature range of chlorite formation is coherent with the estimated trapping  
604 temperatures for fluid inclusions, intersecting in all cases the isochores at realistic pressures (Figure  
605 10). Interestingly, the chlorite temperature range intersects the isochores at higher pressures,  
606 corresponding to lithostatic fluid pressures, for the moderately silicified samples (ODM173 in  
607 particular), than for highly silicified samples (ODM218 in particular) for which the median chlorite  
608 temperatures intersect the isochores at hydrostatic fluid pressures instead. Near hydrostatic fluid  
609 pressures are coherent with the significant fluid amount required to explain pervasive silicification,  
610 thus associated with an open system. In contrast, moderately silicified samples submitted to more

611 restricted fluid circulation may instead correspond to a system only transiently open. Silicification  
612 is both static and linked to deformation episodes, as demonstrated by successive steps of quartz  
613 growth-hydrofracturing-overgrowth (Figures 7 and S3). This complex system witnessed both  
614 spatial and temporal fluid pressure variations, bounded by end-member lithostatic to hydrostatic  
615 pressures, and linked to variations in rock permeability and fault zone connectivity, likely  
616 modulated by both silica sealing and hydrofracturing episodes (Bonnemains et al., 2017).

617 We thus interpret this silicification as a long-lived, complex process along the detachment  
618 plane during exhumation of the hangingwall-derived breccias (Bonnemains et al., 2017), consistent  
619 with the large temperature ranges of both chlorite crystallization and fluid entrapment in quartz.  
620 We also infer that silicification occurred mostly in the temperature range  $\sim 200 - 400$  °C, the highest  
621 temperatures corresponding to the highly silicified sample spanning the largest salinity variations  
622 (2-10 wt.% NaCl, ODM218).

623

## 624 **5.2. Fluid compositions and potential fluid sources**

### 625 ***5.2.1. Insights from fluid inclusion salinity: phase separation***

626 Fluid inclusions contain an aqueous fluid with salinities generally higher than that of seawater.  
627 Fluid inclusions from most samples (ODM155, ODM195, ODM173) present restricted salinity  
628 ranges (4-6 wt.% eq. NaCl) corresponding to  $\sim 115$  to 170% of seawater salinity (3.2 wt.% eq.  
629 NaCl). This range is comparable to ranges of salinity (and Th) measured in fluid inclusions (Figure  
630 8a) in rocks associated with hydrothermal fields both of mafic (TAG: Petersen et al., 1998; MARK:  
631 Delaney et al., 1987; Saccocia & Gillis, 1995) and ultramafic nature (Rainbow, Logatchev,  
632 Ashadze, Semenov, Irinovskoe; Bortnikov et al., 2011, 2014, 2015; Simonov et al., 2015). Fluid  
633 inclusions from the highly silicified sample ODM218 display a large salinity range (2.1 to 10 wt.%  
634 eq. NaCl, Figure 8a). At the grain scale, core-to-rim salinity variations are associated to  
635 luminescence variations (Figures 7b, d, S3b, e and 8b) but do not show any systematic pattern,  
636 rather suggesting that the fault zone witnessed pulses of fluids with variable salinity during  
637 deformation.

638 Salinity in fluid inclusions from subsample ODM218b reaches up to 3 times seawater salinity  
639 (i.e., 10 wt.% equiv. NaCl, Figure 8a). Similar values are also reported for MARK silicified  
640 breccias (Delaney et al., 1987). In contrast, many fluid inclusions of subsample ODM218c cluster

641 at seawater-like salinities, while others in the same sample have salinities below that of seawater  
642 (2.1 wt.% eq. NaCl, Figure 8a), as reported from TAG (Petersen et al., 1998). At least three  
643 mechanisms have been proposed to explain salinities of fluid inclusions differing from that of  
644 seawater: hydration reactions, chloride retention in secondary minerals, and phase separation:

645 (1) Hydration reactions consume water and, consequently, residual fluids may be enriched in  
646 dissolved elements. These reactions increase salinity modestly, with +15% for basalt-seawater  
647 equilibration at 350 °C (Wetzel & Shock, 2000), therefore clearly insufficient to explain the high  
648 salinities recorded in sample ODM218b. This process is only efficient at low water-rock ratio  
649 conditions and closed systems (Delaney et al., 1987). However, important fluid fluxes are required  
650 to attain the observed high levels of silicification (up to ~90 vol.% quartz) in these matrix-supported  
651 breccias (see 5.2.2). This precludes that hydration reactions alone may significantly change  
652 salinities to values consistent with those observed here (Figure 8a).

653 (2) Chloride storage in transient phases (such as amphiboles, up to 4 wt.% chlorine; Vanko,  
654 1988) can also modulate the salinity of the circulating hydrothermal fluids (Kelley & Robinson,  
655 1990; Kelley et al., 1992). At 13°20'N OCC, hydrothermal amphiboles formed under amphibolite  
656 facies conditions (i.e., in clasts, pre-dating silicification) are progressively replaced by chlorite  
657 during silicification at lower temperatures (greenschist facies), and could therefore increase fluid  
658 salinity. However, the low chloride content of these amphiboles (<0.29 wt.%; Bonnemains et al.,  
659 2017) suggests that dissolution of these phases during silicification cannot account by itself for  
660 salinities of fluid inclusions within mafic fault breccias, which are three times higher than those of  
661 seawater.

662 (3) The only efficient mechanism to generate both high and low salinity fluids is the formation  
663 of brine and vapor phases by supercritical phase separation of either seawater or magmatic fluids,  
664 as invoked for high-temperature hydrothermal systems (e.g., Alt et al., 2010; Castelain et al., 2014;  
665 Delaney et al., 1987; Kelley & Delaney 1987; Kelley et al., 1992; Vanko, 1988). At the 13°20'N  
666 detachment fault, the minimum temperature for supercritical phase separation at the seafloor  
667 (~3000 m, 300 bars, see 5.1) is ~400 °C (Figure 11), and would form high salinity brines and a  
668 vapor phase. However, we do not have any direct evidence for in-situ phase separation during  
669 silicification as we lack fluid inclusions with pure brines (up to ~40-50 wt.% eq. NaCl), as observed  
670 in diabbases (Kelley & Delaney, 1987) or trondhjemite (Castelain et al., 2014; Figure 8a), or



671 inclusions with pure vapor phase (vapor to total volume of 0.1-0.5 in our study). This suggests that  
672 phase separation occurred earlier, at deeper levels. Vapor and brine were likely segregated and  
673 migrated upwards separately, similarly to the two-stage model proposed by Delaney et al. (1987)  
674 for the MARK hydrothermal field. The wide range of salinities (i.e., from lower- to three times  
675 higher-than-seawater) reported in 13°20'N silicified fault rocks may be accounted for by either re-  
676 homogenization of variable amounts of brines and vapor phases once released in the detachment  
677 fault (in the one-phase field, Figure 11), or their mixing with fluids of different salinity, prior to  
678 fluid entrapment in quartz.

679 Although we have no direct constraints, we hypothesize that phase separation may have  
680 occurred in the brecciation zone or its immediate vicinity. Indeed, most of the breccia clasts from  
681 13°20'N fault zone are originally diabase, suggesting that they were initially part of the  
682 hangingwall dyke complex adjacent to the detachment fault (see 2.2 and 5.1 and Bonnemains et  
683 al., 2017). With a fully developed amphibolite facies paragenesis (hornblende + labradorite), these  
684 rocks experienced hydrothermal alteration at temperatures higher than 500 °C (see review in Alt,  
685 1995), likely at the base of the upper crust (root of the dyke complex), therefore acting as a reaction  
686 zone. Fluid pressures in this reaction zone may be between hydrostatic and lithostatic, even close  
687 to hydrostatic for high fluid fluxes. Figure 11 shows that cold seawater infiltrating the hangingwall  
688 towards the base of the crust would undergo phase separation between 440 °C and 570 °C,  
689 depending on the fluid pressure gradient. It is thus plausible that phase separation occurred in the  
690 reaction zone where brecciation is inferred to take place (e.g., Bonnemains et al., 2017). Diabase  
691 brecciation along the detachment fault zone may even enhance phase separation, promoting sudden  
692 fluid pressure drops leading to the crossing of the liquid-vapor curve (Figure 11).

693

#### 694 ***5.2.2. Insights from bulk-rock and chlorite compositions: a mafic-rock derived fluid***

695 Textural and mineralogical observations, coupled to bulk-rock analyses, document that diabase  
696 breccias underwent variable silicification during exhumation within the detachment zone (see  
697 4.1.1), reaching up to ~90 vol.% of quartz in matrix-supported breccias (Figure 5; Tables 2 and  
698 S1). Such degrees of silicification require both circulation of a silica-rich fluid and high fluid-rock  
699 ratios along the detachment fault zone. Indeed, experiments suggest that water-rock ratios >50 are  
700 required for basalt replacement by quartz-chlorite assemblages at 300 °C (Mottl, 1983). Elevated

701 fluid fluxes are also supported by the enhanced leaching of alkalis and calcium (Figures 5a and  
702 S1a-b) from diabase clasts with increasing silicification (Bach et al., 2013; Cann, 1969).

703 Chlorite crystallization in both clasts and matrix is associated to silicification, as showed by  
704 chlorite and quartz co-crystallization textures, increasing amount of chlorite with silicification, and  
705 similar chlorite composition in both clasts and matrix (Figure 6a). The decrease of bulk-rock and  
706 chlorite Mg# with increasing silicification (Figures 5b and 6b), correlated to pyrite crystallization  
707 in the highly silicified breccias, suggests interaction with iron-rich fluids. The association iron-rich  
708 chlorites, quartz and pyrite has been observed in silicified oceanic hydrothermal breccias associated  
709 with mafic-rock hosted vents such as TAG (Alt et al., 1985; Honnorez et al., 1998; Humphris et  
710 al., 1998) or at the MARK area (Delaney et al., 1987; Saccocia & Gillis, 1995). For Saccocia and  
711 Gillis (1995), these minerals result from interactions with high salinity, silica- and iron-rich fluids,  
712 depleted in H<sub>2</sub>S. This is in agreement with the high salinity (Figure 8) and low H<sub>2</sub>S content (only  
713 recorded in 4 fluid inclusions from ODM218, Figure 9a) in our fluid inclusions. Hence, almost all  
714 H<sub>2</sub>S was likely stored into pyrite, leading to iron-enriched fluids from which Fe-rich chlorites  
715 crystallized (type I breccias from Saccocia & Gillis, 1995). A low H<sub>2</sub>S content in fluids is also  
716 consistent with the small amount of metallic trace elements recorded in our fluid inclusions (i.e.,  
717 diluted fluids, see 4.2.3). Such fluid composition is characteristic of highly evolved hydrothermal  
718 fluids sampled in upflow zones of hydrothermal cells, and recording mafic rock-hosted reaction  
719 zones (Bach et al., 2013; Saccocia & Gillis, 1995).

720 The significant amounts of silica precipitated in detachment fault breccias also suggest the  
721 leaching of a deep mafic source. Indeed, high-temperature hydrothermal fluids from the reaction  
722 zone at the base of the mafic upper crust may be quartz-saturated (or close to) according to Wetzel  
723 and Shock (2000; ~20 mmolal of aqueous silica at 400°C for seawater-basalt equilibrium). This is  
724 in agreement with fluid composition from basalt-hosted hydrothermal vents at >300 °C (Fouquet  
725 et al., 2010; Schmidt et al., 2011; McDermott et al., 2018). Fluids circulating upwards along the  
726 detachment fault zone may witness both a significant temperature reduction (to 200-300 °C) and  
727 pressure drops, promoting fluid supersaturation and quartz precipitation. On the contrary,  
728 hydrothermal fluids equilibrated with peridotite should be largely undersaturated with respect to  
729 quartz (0.5 mmolal of aqueous silica at 400°, Wetzel & Shock, 2000), and vent fluids from  
730 ultramafic-hosted hydrothermal systems generally record 6-8 mmol/L of aqueous silica (Fouquet,  
731 2010). Under these conditions, a temperature drop of 200 °C will not be sufficient to trigger quartz

732 crystallization. Hence, silica may only be provided by fluids reacting with mafic rocks. Moreover,  
733 the high amount of silica crystallized in the breccia matrix (up to 90 vol% of quartz) requires  
734 circulation of extremely Si-rich fluids: phase separation and brine formation in the reaction zone  
735 may have enhanced aqueous silica concentration, as quartz solubility is about one order of  
736 magnitude higher in NaCl-rich brines than in pure H<sub>2</sub>O ( Scheuermann et al., 2018; Schmidt et al.,  
737 2011; Steele-MacInnis et al., 2011), promoting efficient silica transport towards the upflow zone  
738 along the detachment fault.

739 Therefore, significant amounts of highly evolved hydrothermal fluids from a reaction zone at  
740 the base of the hangingwall dyke complex flowed up along the detachment fault zone, transporting  
741 leached aqueous silica. This syntectonic circulation resulted in intense and pervasive silicification  
742 of mafic detachment fault breccias (with crystallization of Fe-rich chlorite and pyrite).

743

### 744 ***5.2.3. Insights from fluid inclusion gas content: mix with an ultramafic-derived fluid***

745 While most fluid inclusions are purely aqueous (H<sub>2</sub>O-NaCl), some contain small amounts of H<sub>2</sub>,  
746 CO<sub>2</sub>, CH<sub>4</sub>, and minor amounts of H<sub>2</sub>S (i.e., ODM218b and ODM218c; Figure 9; Table 3) in  
747 addition to dominant H<sub>2</sub>O (H<sub>2</sub>O-NaCl-H<sub>2</sub>±CO<sub>2</sub>±CH<sub>4</sub>±H<sub>2</sub>S). Seawater phase separation cannot  
748 produce all these gases, and other fluid sources are required. Among these minor gases, H<sub>2</sub> is by  
749 far the most abundant in the inclusions (Figure 9; Table 3). H<sub>2</sub> is likely produced during  
750 serpentinization reactions by oxidation of the iron contained in olivine, reactions that preferentially  
751 occur between 200 and 350 °C (Martin & Fyfe, 1970; McCollom & Bach, 2009; Seyfried et al.,  
752 2007). At high temperatures (>400 °C), H<sub>2</sub> may also be produced in mafic rocks by pyroxene  
753 alteration (Allen & Seyfried, 2003; Foustoukos & Seyfried, 2005). CO<sub>2</sub> can be either linked to  
754 seawater, or to a magmatic source enriching nearby fluids. CH<sub>4</sub> likely results from CO<sub>2</sub>-rich fluids  
755 reacting with H<sub>2</sub>. This reaction may occur either during serpentinization, from hydrothermal  
756 circulation in ultramafic rocks enriching fluids in both hydrogen and methane (Berndt et al., 1996;  
757 Boulart et al., 2013; Charlou et al., 1998, 2002; Holm & Charlou, 2001; Monnin et al., 2014; Wetzell  
758 & Shock, 2000), in H<sub>2</sub>-rich fluid inclusions hosted in footwall magmatic rocks (e.g., Klein et al.,  
759 2019; McDermott et al., 2015), or at a later time (e.g., during transport), but in any case, prior to  
760 fluid entrapment during silicification.

761 To discriminate the origin of fluids that circulated along the detachment fault zone, we compare  
762 the ratios of H<sub>2</sub>, CO<sub>2</sub>, CH<sub>4</sub>, H<sub>2</sub>S in our fluid inclusions to those analyzed in vent fluids (from MAR  
763 mainly). While few inclusions present a CO<sub>2</sub>-dominant gas content comparable to basalt-hosted  
764 vent fluids, most of these inclusions show high H<sub>2</sub>/CO<sub>2</sub> and H<sub>2</sub>/CH<sub>4</sub> ratios (Figure 9a) and very low  
765 H<sub>2</sub>S/H<sub>2</sub> ratios (Figure 9b), signatures typical of ultramafic-hosted vent fluids (e.g., Rainbow,  
766 Logatchev, Semenov, Irinovskoe; Destringeville et al., 2015; Fouquet et al., 2010; Schmidt et al.,  
767 2011), and of hydrothermal alteration of ultramafic rocks (i.e., serpentinization < 400 °C, Wetzell  
768 & Shock, 2000). However, fluids from the Piccard vents at the ultraslow spreading Cayman ridge  
769 show anomalously high H<sub>2</sub> contents and H<sub>2</sub>/H<sub>2</sub>S ratios, for mafic-rock-derived vents (McDermott  
770 et al., 2018). These fluids are interpreted as resulting from basalt alteration in a reaction zone at  
771 very high temperature (>500°C) and high fluid/rock ratios (McDermott et al., 2018; Scheuermann  
772 et al., 2018). This suggests that the high H<sub>2</sub>/H<sub>2</sub>S ratios analyzed in our fluid inclusions could derive  
773 from the hangingwall reaction zone. Lacking experimental data on basalt alteration at >500°C,  
774 reactions able to release such high H<sub>2</sub> amounts remain unknown. The reaction invoked by  
775 Scheuermann et al. (2020), of amphibole destabilization to magnetite and quartz, is clearly  
776 incompatible with our rocks, as hornblende is fresh in the least altered clasts (Bonnemains et al.,  
777 2017), and no magnetite (neither quartz) was observed. Moreover, H<sub>2</sub>/H<sub>2</sub>S ratios in Piccard vent  
778 fluids remain lower than those measured in most of our fluid inclusions (Figure 9b), although there  
779 is no reason for different partitioning of H<sub>2</sub> and H<sub>2</sub>S between brines and vapor phases after phase  
780 separation (McDermott et al., 2018; Scheuermann et al., 2020). Therefore, H<sub>2</sub> production in the  
781 reaction zone seems to be possible, but may not account for the elevated H<sub>2</sub>/H<sub>2</sub>S ratios analyzed in  
782 our fluid inclusions, which are best explained by H<sub>2</sub> derived from ultramafic-rock serpentinization.  
783 Contribution of ultramafic-derived fluids is further supported by slight Cr and Ni enrichments of  
784 both sample ODM218b (Figure 5c) and some chlorites from highly silicified mafic breccias (Tables  
785 S2 and S3; Angiboust et al., 2014; Boutoux et al., 2014; Locatelli et al., 2019 ; Spandler et al.,  
786 2011).

787 While the hangingwall sampled by the fault zone likely extends only to the base of the dyke  
788 complex, the footwall below the fault zone and deep sections of the hangingwall likely contain  
789 mantle peridotites that witnessed fluid circulation. This is demonstrated by the occurrence of mixed  
790 breccias containing altered ultramafic clasts (Bonnemains et al., 2017), and the outcropping of  
791 ultramafic rocks throughout the area (Escartin et al., 2017; MacLeod et al., 2011). During

792 exhumation, peridotites likely interacted with seawater-derived fluids, and progressively  
793 serpentinized. Fluids may have been subsequently channelized into and along the detachment fault  
794 zone. Mixing of such seawater-salinity fluids with silica-rich brines and vapor phases (prior to  
795 entrapment) could account for the wide salinity range observed in trapped fluids from the silicified  
796 breccias (Figure 8). This contribution of serpentinization fluids must remain limited nonetheless,  
797 as the absolute gas amounts trapped in fluid inclusions are extremely low. We also note that two  
798 thirds of the analyzed fluid inclusions from ODM218 have a gas signature very close to that  
799 analyzed for Irinovskoe vent fluids (Figure 9a), and that present-day fluid circulation within the  
800 footwall may record similar fluid-peridotite reactions at depth, even though these fluids do not  
801 exploit the detachment fault as a flow channel.

802

### 803 **5.3. Detachment faulting, potential heat sources at the ridge axis and scenario for fluid** 804 **pathways**

805 Our results suggest that silicification was linked to flow along the detachment fault zone of  
806 silica-rich brines and minor vapor phases likely mainly formed in the hangingwall reaction zone  
807 (Figure 12a). Such a reaction zone at the base of the upper crust requires a heat source, such as a  
808 magma chamber at deeper levels and nearby the fault, or an along-axis dyke propagation  
809 (Bonnemains et al., 2017; MacLeod et al., 2009). The conceptual model in Figure 12a builds on  
810 the detachment fault zone structure suggested by Bonnemains et al. (2017) and Parnell-Turner et  
811 al. (2018). This model includes a) the incorporation of mafic clasts from the hangingwall upper  
812 crust into the detachment fault zone, from its base to the near-surface (brown stars in Figure 12),  
813 b) a thickening of the fault zone during exhumation, and c) an anastomosed fault zone mixing  
814 footwall-derived ultramafic material with dominant mafic material from the hangingwall. This  
815 model is also consistent with recent 3D seismic experiments revealing elevated seismic velocities  
816 at the footwall, both along the exposed detachment fault, and below its continuation eastwards  
817 below the rift valley floor (Simão et al., 2020). Elevated footwall seismic velocities are consistent  
818 with a lithosphere composed of lower crust and upper mantle rocks, juxtaposed to mafic rocks  
819 across the detachment (Simão et al., 2020).

820 As illustrated in Figure 12b, we propose that seawater percolates downwards through the  
821 hangingwall crust, reaching a reaction zone at temperatures  $>500$  °C, at or near the axial zone.

822 High-temperature fluids circulating into the reaction zone may hydrothermally alter surrounding  
823 mafic rocks, while releasing aqueous silica and potentially small amounts of H<sub>2</sub>S in the fluid phase  
824 (e.g., Bach et al., 2013; Wetzel & Shock, 2000). At these P-T conditions, phase separation occurs  
825 and forms high-salinity brines and low-salinity vapor phases. The small number of inclusions  
826 recording lower-than-seawater salinity (Figure 8a) suggests that only limited amounts of vapor  
827 reached and circulated within the detachment zone, while most of these low-density vapor phases  
828 may have migrated upwards through the hangingwall crust (Figures 11 and 12). Denser, less  
829 buoyant brines may be stored at depth in crustal porosity, within diabase units (Fontaine &  
830 Wilcock, 2006; Fontaine et al., 2007). Brines may be released into the detachment fault zone upon  
831 diabase brecciation, together with minor amounts of vapor phases, locally produced H<sub>2</sub>S, and  
832 potentially CO<sub>2</sub> either transported by seawater or exsolved from the magma lens. Diabase  
833 brecciation may enhance phase separation by causing sudden and local fluid pressure drops (Figure  
834 11). In turn, fluid phase separation may also promote local overpressures that may favor brecciation  
835 along the fault (André-Mayer et al., 2002; Bertelli & Baker, 2010), with possible links to seismicity  
836 along the detachment.

837 Varying gas content and wide salinity ranges of trapped fluids point to a complex and dynamic  
838 system. During silicification of the fault zone, upwelling silica-rich brines and minor vapors mixed  
839 in variable amounts with H<sub>2</sub>(± CH<sub>4</sub>)-rich fluids derived from serpentinization of ultramafic material  
840 from the footwall (Figures 11 and 12; Andreani et al., 2014; McCaig et al., 2010; McCaig & Harris,  
841 2012). These fluids homogenized as a single fluid phase before trapping (one-phase fluid field,  
842 Figure 11). Fluid fluxes from these different sources were likely variable both in time and within  
843 the fault zone, resulting in strong variability of both gas content and salinity of fluid inclusions  
844 (Figures 8 and 9). Significant variations of inclusion fluid composition at quartz grain scale  
845 (Figures 7b, d, S3b, e and 8b) clearly indicate that the fluids circulating along the detachment were  
846 inherently heterogeneous at small spatial scales and short temporal scales. Yet there is no evidence  
847 for any systematic long-term evolution in fluid sources or fluid mixing processes during  
848 silicification (i.e., similarity in primary and secondary fluid inclusion salinity ranges). Moreover,  
849 the wide distribution of samples along axis and the pervasively silicified fault zone also indicate  
850 that this heterogeneous flow was maintained over long-periods of time, and was sampled by the  
851 detachment fault along most of its along-axis length.

852 All these fluids were preferentially channelized within the permeable fault zone, and silica  
853 precipitation was likely triggered by a combination of temperature decrease, pressure drops, and  
854 mixing of silica-rich brines with less-salted fluids. Both chlorite and fluid inclusion temperatures  
855 (Figures 10 and 11) are lower than those measured at the base of the dyke complex elsewhere (Hole  
856 1256; Alt et al., 2010), documenting a significant temperature drop and silicification occurring  
857 under greenschist facies conditions. Upflow silica-rich brines were likely cooled either  
858 continuously or episodically, during transient circulation in a complex, anastomosing fault zone,  
859 and coeval with deformation leading to quartz fracturing-sealing episodes (i.e., fluid pressure  
860 varying between hydrostatic and lithostatic; Figures 7 and 10), but also by fluid mixing with cooler  
861 fluids from the footwall serpentinization and potentially seawater percolating from the seafloor.

#### 862 **5.4. Fluids trapped in detachment fault rocks vs. seafloor hydrothermal venting**

863 Models of fluid flow and detachment faulting often assume a permeable fault zone efficiently  
864 channeling fluids to the seafloor or the shallow crust (e.g., Andersen et al., 2014; McCaig & Harris,  
865 2012; Tao et al., 2020). In these models, fluid flow through the detachment fault feeds hydrothermal  
866 systems found both at the footwall (e.g., Logatchev; Andersen et al., 2014; Longqi: Tao et al.,  
867 2020) and hangingwall (TAG; McCaig & Harris, 2012). The heat source animating this circulation  
868 is often located in the upper mantle, at the base of the detachment microseismicity.

869 Our data and results from the 13°20'N detachment are not consistent with these deep-rooted  
870 hydrothermal systems along detachment fault zones. First, the present-day Irinovskoe  
871 hydrothermal site is located on the striated surface. As the detachment fault emerges at <20° at the  
872 hangingwall cutoff and the detachment is capped by a highly fractured and deformed fault zone  
873 (e.g., Escartín et al., 2017; Parnell-Turner et al., 2018), no plausible mechanism can channel fluids  
874 from the active detachment fault zone below the rift valley floor (below the hangingwall cutoff) to  
875 the Irinovskoe site, over a horizontal distance of ~2 km. The footwall also displays both a high-  
876 velocity seismic anomaly underlying Irinovskoe, restricted to the shallower 2 km, and a broad low  
877 velocity zone at 7-10 km depth (Simão et al., 2020). Owing to seismic resolution limitations, the  
878 presence of magma chambers or heat sources of sizes below the seismic resolution (1 to 3 km in  
879 size, depending on the depth) cannot be excluded. We propose that the fluid circulation system  
880 underlying Irinovskoe is unrelated to the active detachment, and instead is fully hosted within the  
881 footwall, probably reaching depths >2 km. While we lack direct seismic evidence here, this model

882 is similar to that of Rainbow, a hydrothermal field at the top of a detachment massif that is underlain  
883 by seismic reflectors identified as active and fossil magma chambers at depths >3 km (Canales et  
884 al., 2017; Dunn et al., 2017).

885 Silicified fault rocks are distributed throughout the detachment, displaying similar fluid  
886 compositions in quartz inclusions. This observation points to a flow organization along the  
887 detachment that has not been recognized before. Geological observations demonstrate that  
888 syntectonic silicification and associated fluid circulation occurred along the whole length (along-  
889 axis, Figure 1) of the active detachment, and that it operated continuously over time (across-axis;  
890 Bonnemains et al., 2017). Fluid inclusions further indicate that similar fluid sources (similar  
891 primary and secondary inclusions) mixed within the detachment plane (see 5.2.1 and Figure 8a).  
892 This type of distributed and pervasive hydrothermal circulation, extending laterally over several  
893 km and sustained over long periods of time, contrasts with the extremely localized outflow  
894 observed at the seafloor over relatively small surfaces (spatial scales of a few hundreds of m at  
895 most). Assuming that similar fluid circulation linked to deformation operates along the present-  
896 day, active detachment fault and at depth, this would require an extreme fluid flow localization on  
897 a short vertical distance (~2 km), in addition to implausible fluid transport within the footwall.

898 In our preferred interpretation, the fault zone and the fluids within cool down efficiently during  
899 exhumation at the shallower levels of the fault. This cooling can effectively suppress convection  
900 and any active circulation in shallow parts of the system, precluding discharge of high-temperature  
901 fluids at the seafloor. We suggest that the observed present-day hydrothermal activity observed on  
902 the surface of footwall of detachments (e.g., Rainbow, Semenov, Irinovskoe, Mount Den, Mount  
903 Fuji) is most likely due to heat sources underlying these sites and located within the detachment  
904 footwall, rather than fluids steered along the detachment fault and with significant lateral flow. The  
905 hydrothermal system that we document here may be indeed active at depth at 13°20'N, and be  
906 widespread at other systems. Indeed, many active detachments rooting near-axis (e.g., TAG,  
907 Dragon Horn) may be active in close proximity to nearby heat sources (melt lenses or dykes  
908 propagating along-axis), sampling fluids from the associated reaction zone at depth. As these  
909 systems may be restricted to deep lithospheric levels (>1 km) and lack a seafloor expression, they  
910 may only be identifiable studying in situ detachment fault rocks.

911



## 912 **6. Conclusions**

913 The 13°20'N detachment fault zone displays pervasive, syntectonic silicification of fault breccia  
914 that is originally mostly of mafic origin (diabase). Quartz crystals in breccia matrix and clasts  
915 preserve fluid inclusions. Their analyses, coupled to both bulk-rock and chlorite geochemical  
916 compositions, allow us to constrain hydrothermal fluid flow during deformation, and propose a  
917 conceptual model of detachment deformation and fluid flow.

918 First, we document the mixing of two fluid sources based on fluid inclusion salinity and gas  
919 content: 1) primarily brines and minor amounts of vapor phases resulting from phase separation at  
920 high temperature ( $T > 410$  °C), and likely occurring in the hangingwall reaction zone at the base of  
921 the dyke complex; and 2) minor amounts of fluids that interacted with ultramafic rocks, likely  
922 recording serpentinization reactions at temperatures of 200-350 °C, associated with H<sub>2</sub> (and CH<sub>4</sub>)  
923 production. The lack of correlation between salinity and gas content, as well as quartz grain-scale  
924 variations of fluid composition, suggests syntectonic mixing in variable proportions of  
925 compositionally heterogeneous flows at small spatial and short temporal scales.

926 The hydrothermal circulation we document along the detachment fault zone reaches the base of  
927 the hangingwall dyke complex, i.e., 2 km depth, as constrained by seismic refraction data. Fault  
928 zone rocks are brecciated and incorporated into the detachment, together with the silica-rich brines  
929 emanating from a nearby reaction zone. A significant temperature drop is recorded by chlorite  
930 thermometry, from amphibolite facies (~500 °C) to quartz/chlorite equilibrium temperatures as low  
931 as ~200 °C. This temperature drop likely occurs both over small spatial distances and over short  
932 periods of time, with transients, promoting syntectonic silica precipitation in the fault zone. The  
933 hydrothermal circulation documented here is decoupled from present day hydrothermal activity at  
934 the seafloor. We suggest that detachment-related hydrothermal flow, which is widespread, is likely  
935 hosted within the footwall of detachments, passively cross-cuts inactive detachment faults, and is  
936 unrelated to the active detachment fault operating at depth.

937  
938 **Acknowledgements** – The authors warmly acknowledge M-C. Caumon for her help with Raman  
939 Spectroscopy on fluid inclusions at GeoRessources Nancy, O. Boudouma and M. Fialin for their  
940 assistance with SEM-cathodoluminescence and EPMA respectively, M. Quintin and E. Delairis for  
941 thin and thick sections preparation respectively. We thank B. Dubacq and J. Touret for fruitful

942 discussions on chlorite analysis and fluid inclusions, respectively. Two anonymous reviewers are  
943 acknowledged for their critical remarks, and W. Berh and Associate Editor for editorial handling.  
944 This work was funded by INSU Tellus-SYSTER program (ODEFLUIN). Data were acquired  
945 during the ODEMAR cruise (<https://doi.org/10.17600/13030070>) and we thank the extraordinary  
946 work of the crew, engineers, and officers that led to an extremely successful cruise. Bathymetry  
947 (shipboard and AUV) data are publicly available through [www.seanoe.org](http://www.seanoe.org)  
948 (<https://doi.org/10.17882/48324>, <https://doi.org/10.17882/48335>), and samples presented here are  
949 available for further studies through the Marine Rock Repository at IPGP (see [lithotheque.ipgp.fr](http://lithotheque.ipgp.fr))  
950 or contacting JE.

951 **References**

- 952 Allen, D.E. & Seyfried, W.E. (2003) Compositional controls on vent fluids from ultramatic-  
953 hosted hydrothermal systems at mid-ocean ridges: An experimental study at 400 degrees C,  
954 500 bars. *Geochimica Et Cosmochimica Acta*, 67, 1531-1542.  
955 [https://doi.org/10.1016/S0016-7037\(02\)01173-0](https://doi.org/10.1016/S0016-7037(02)01173-0)
- 956 Alt, C. J. (1995). Subseafloor processes in mid-ocean ridge hydrothermal systems. In S. E.  
957 Humphris et al. (Eds.), *Seafloor Hydrothermal Systems: Physical, Chemical, Bio- logical,*  
958 *and Geological Interactions, Geophys. Monogr. Ser.* (Vol. 91, pp. 85–114). Washington, DC:  
959 AGU, <https://doi.org/10.1029/GM091p0085>.
- 960 Alt, J.C., Laverne, C., Coggon, R.M., Teagle, D.A.H., Banerjee, N.R., Morgan, S., et al. (2010).  
961 Subsurface structure of a submarine hydrothermal system in ocean crust formed at the East  
962 Pacific Rise, ODP/IODP Site 1256. *Geochemistry, Geophysics, Geosystems*, 11(10), p. 1-28.  
963 <https://doi.org/10.1029/2010GC003144>
- 964 Alt, J.C., Laverne, C., & Muehlenbachs, K. (1985). Alteration of the upper oceanic crust:  
965 mineralogy and processes in Deep Sea Drilling Project Hole 504B, Leg 83. In R.N. Anderson,  
966 J. Honnorez, K. Becker, et al., *Init. Repts. DSDP*, 83: Washington (US Govt. Printing Office),  
967 217-247
- 968 Andersen, C., Rupke, L., Hasenclever, J., Grevemeyer, I., & Petersen, S. (2014). Fault geometry  
969 and permeability contrast control vent temperatures at the Logatchev 1 hydrothermal field,  
970 Mid-Atlantic Ridge. *Geology*, 43(1), 51–54. <https://doi.org/10.1130/G36113.1>
- 971 André-Mayer, A-S., Leroy, J.L., Bailly, L., Chauvet, A., Marcoux, E., Grancea, L., et al. (2002).  
972 Boiling and vertical mineralization zoning: a case study from the Apacheta low-sulfidation  
973 epithermal gold-silver deposit, southern Peru. *Mineralium Deposita*, 37, 452-464.  
974 <https://doi.org/10.1007/s00126-001-0247-2>
- 975 Andreani, M., Escartin, J., Delacour, A., Ildefonse, B., Godard, M., Dymont, J., Fallick, A.E., &  
976 Fouquet, Y. (2014). Tectonic structure, lithology, and hydrothermal signature of the Rainbow  
977 massif (Mid-Atlantic Ridge 36°14'N). *Geochemistry, Geophysics, Geosystems*, 15, 3543-  
978 3571. <https://doi.org/10.1002/2014GC005269>
- 979 Angiboust, S., Pettke, T., De Hoog, J.C.M., Caron, B., & Oncken, O. (2014). Channelized Fluid  
980 Flow and Eclogite-facies Metasomatism along the Subduction Shear Zone. *J. Petrol.* 55,  
981 883–916. <https://doi.org/10.1093/petrology/egu010>

- 982 Bach, W., Jons, N., & Klein, F. (2013). Metasomatism within the oceanic crust. In D. E. Harlov &  
983 H. Austrheim (Eds.). *Metasomatism and the chemical transformation of rock*. Lecture notes  
984 in Earth System Sciences. Springer, Berlin, Heidelberg. [https://doi.org/10.1007/978-3-642-](https://doi.org/10.1007/978-3-642-28394-9_8)  
985 [28394-9\\_8](https://doi.org/10.1007/978-3-642-28394-9_8)
- 986 Berndt, M.E., Allen, D.E. & Seyfried, W.E. (1996) Reduction of CO<sub>2</sub> during serpentinization of  
987 olivine at 300 degrees C and 500 bar (vol 24, pg 351, 1996). *Geology*, **24**, 671-671.  
988 [https://doi.org/10.1130/0091-7613\(1996\)024<0351:ROCDSO>2.3.CO;2](https://doi.org/10.1130/0091-7613(1996)024<0351:ROCDSO>2.3.CO;2)
- 989 Bertelli, M. & Baker, T. (2010). A fluid inclusion study of the Suicide Ridge Breccia Pipe,  
990 Cloncurry district, Australia: implication for breccia genesis and IOCG mineralization.  
991 *Precambrian Research*, *179* (1-4), 69-87. <https://doi.org/10.1016/j.precamres2010.02.016>
- 992 Bodnar, R. J. (1993). Revised equation and table for determining the freezing point depression of  
993 H<sub>2</sub>O-NaCl solutions. *Geochim. Cosmochim. Acta* *57*, 683–684.
- 994 Boiron, M.C., Essarraj, S., Sellier, E., Cathelineau, M., Lespinasse, M., Poty, B. (1992).  
995 Identification of fluid inclusions in relation to their host microstructural domains in quartz  
996 by cathodoluminescence. *Geochim. Cosmochim Acta* *56*, 175–185.
- 997 Bonnemains, D., Escartín, J., Mével, C., Andreani, M., & Verlaquet, A. (2017). Pervasive  
998 silicification and hanging wall overplating along the 13°20'N oceanic detachment fault (Mid-  
999 Atlantic Ridge): *Geochemistry, Geophysics, Geosystems*, *18*(6), 2028–2053.  
1000 <https://doi.org/10.1002/2017GC006846>
- 1001 Bortnikov, N.S., Simonov, V.A., Amplieva, E.E., & Borovikov, A.A. (2014). Anomalously high  
1002 concentrations of metals in fluid of the Semenov Modern Hydrothermal System (Mid-  
1003 Atlantic Ridge, 13°31'N): LA-ICP-MS study of fluid inclusions in minerals. *Doklady Earth*  
1004 *Sciences*, *456*(2), 714-719. <https://doi.org/10.1134/S1028334X14060221>
- 1005 Bortnikov, N.S., Simonov, V.A., Amplieva, E.E., Stavrova, O.O., & Fouquet, Y. (2011). The  
1006 physicochemical conditions of hydrothermal ore-forming systems of “black smokers”  
1007 associated with mantle ultrabasites in the Central Atlantic region. *Russian Geology and*  
1008 *Geophysics*, *52*(11), 1412–1420. <https://doi.org/10.1016/j.rgg.2011.10.010>
- 1009 Bortnikov, N.S., Simonov, V.A., Borovikov, A.A., Bel, V.E., Amplieva, E.E., Kotlyarov, A. V,  
1010 and Bryanskiy, N. V (2015). The metalliferous fluid of the hydrothermal sulfide system  
1011 associated with the oceanic core complex 13°20'N, The Mid-Atlantic Ridge (LA-ICP-MS  
1012 and fluid inclusions), in *Oceanic Core Complexes and Hydrothermalism*, p. 80–83

- 1013 Boschi, C., Früh-Green, G., Delacour, A., Karson, J., & Kelley, D.S. (2006). Mass transfer and  
1014 fluid flow during detachment faulting and development of an oceanic core complex, Atlantic  
1015 Massif (MAR 30°N). *Geochemistry, Geophysics, Geosystems*, 7(1), Q01004,  
1016 <https://doi.org/10.1029/2005GC001074>
- 1017 Boulart, C., Chavagnac, V., Monnin, C., Delacour, A., Ceuleneer, G., & Hoareau, G. (2013).  
1018 Differences in gas venting from ultramafic-hosted warm springs: the example of Oman and  
1019 Ligurian Ophiolites. *Ophioliti*, 38(2), 142-156. <https://doi.org/10.4454/phioliti.v38i2.423>.
- 1020 Bourdelle, F., Parra, T., Chopin, C., & Beyssac, O. (2013). A new chlorite geothermometer for  
1021 diagenetic to low-grade metamorphic conditions. *Contributions to Mineralogy and  
1022 Petrology*, 165(4), 723–735. <https://doi.org/10.1007/s00410-012-0832-7>
- 1023 Bourdelle, F. & M. Cathelineau (2015). Low-temperature chlorite geothermometry: a graphical  
1024 representation based on a T–R<sup>2+</sup>–Si diagram. *European Journal of Mineralogy*, 27(5), 617-  
1025 626. <https://doi.org/10.1127/ejm/2015/0027-2467>
- 1026 Boutoux, A., Verlaquet, A., Bellahsen, N., Lacombe, O., Villemant, B., Caron, B., Martin, E.,  
1027 Assayag, N., & Cartigny, P. (2014) Fluid systems above basement shear zones during  
1028 inversion of pre-orogenic sedimentary basins (External Crystalline Massifs, Western Alps).  
1029 *Lithos*, 206–207, 435–453. <https://doi.org/10.1016/j.lithos.2014.07.005>
- 1030 Buck, W.R., Lavier, L.L., and Poliakov, A.N.B., 2005, Modes of faulting at mid-ocean ridges:  
1031 *Nature*, v. 434, p. 719–723
- 1032 Canales, J.P., Dunn, R.A., Arai, R., & Sohn, R.A. (2017). Seismic imaging of magma sills beneath  
1033 an ultramafic-hosted hydrothermal system. *Geology*, 45(5), 451–454.  
1034 <https://doi.org/10.1130/G38795.1>
- 1035 Cann, J.R. (1969). Spilites from the Carlsberg Ridge, Indian Ocean. *Journal of Petrology*, 10, 1–  
1036 19
- 1037 Cannat, M., Sauter, D., Mendel, V., Ruellan, E., Okino, K., Escartin, J., Combier, V., & Baala, M.  
1038 (2006). Modes of seafloor generation at a melt-poor ultraslow-spreading ridge. *Geology*,  
1039 34(7), 605–608. <https://doi.org/10.1130/G22486.1>
- 1040 Carignan, J., Hild, P., Mevelle, G., Morel, J., & Yeghicheyan, D. (2001). Routine analyses of trace  
1041 elements in geological samples using flow injection and low pressure on-line liquid  
1042 chromatography coupled to ICP-MS: a study of geochemical reference materials BR, DR-N,

1043 UB-N, AN-G and GH. *Geostandards and Geoanalytical Research*, 25(2–3), 187–198.  
1044 <https://doi.org/10.1111/j.1751-908X.2001.tb00595.x>

1045 Castelain, T., McCaig, A.M., & Cliff, R.A. (2014). Fluid evolution in an Oceanic Core Complex:  
1046 A fluid inclusion study from IODP hole U1309 D-Atlantis Massif, 30°N, Mid-Atlantic  
1047 Ridge. *Geochemistry, Geophysics, Geosystems*, 15(4), 1193–1214.  
1048 <https://doi.org/10.1002/2013GC004975>

1049 Charlou, J.L., Fouquet, Y., Bougault, H., Donval, J.P., Etoubleau, J., Jean-Baptiste, P., Dapoigny,  
1050 A., Appriou, P., & Rona, P.A. (1998). Intense CH<sub>4</sub> plumes generated by serpentinization of  
1051 ultramafic rocks at the intersection of the 15°20'N fracture zone and the Mid-Atlantic Ridge.  
1052 *Geochim. Cosmochim. Acta* 62, 2323 – 2333. [https://doi.org/10.1016/S0016-7037\(98\)00138-](https://doi.org/10.1016/S0016-7037(98)00138-0)  
1053 0

1054 Charlou, J.J., Donval, J.P., Fouquet, Y., Jean Baptiste, P., & Holm, N. (2002). Geochemistry of  
1055 high H<sub>2</sub> and CH<sub>4</sub> vent fluids issuing from ultramafic rocks at the Rainbow hydrothermal field  
1056 (36°14'N, MAR). *Chemical Geology*, 191, 345–359. [https://doi.org/10.1016/S0009-](https://doi.org/10.1016/S0009-2541(02)00134-1)  
1057 2541(02)00134-1

1058 Cherkashev, G.A., Ivanov, V.N., Lazareva, L.I., Rozhdestvenskaya, I.I., Samovarov, M.L.,  
1059 Poroshina, I.M., Sergeev, M.B., Stepanova, T. V, &c Dobretsova, I.G. (2013). Massive  
1060 sulfide ores of the northern equatorial Mid Atlantic Ridge. *Oceanology*, 53(5), 607–619.  
1061 <https://doi.org/10.1134/S0001437013050032>

1062 Coumou, D., Driesner, T., Geiger, S., Paluszny, A., & Heinrich, C. A. (2009). High-resolution  
1063 three-dimensional simulations of mid-ocean ridge hydrothermal systems. *J. Geophys. Res.*,  
1064 114, B07104, <https://doi.org/10.1029/2008JB006121>

1065 Delaney, J.R., Mogk, D.W., & Mottl, M. (1987). Quartz-cemented breccias from the Mid-Atlantic  
1066 Ridge: Samples of a high-salinity hydrothermal upflow zone. *Journal of Geophysical*  
1067 *Research*, 92(B9), 9175. <https://doi.org/10.1029/JB092iB09p09175>

1068 deMartin, B.J., Sohn, R.A., Canales, J.P., & Humphris, S.E. (2007). Kinematics and geometry of  
1069 active detachment faulting beneath the Trans-Atlantic Geotraverse (TAG) hydrothermal field  
1070 on the Mid-Atlantic Ridge. *Geology*, 35(8), 711–714. <https://doi.org/10.1130/G23718A.1>

1071 Destrigneville, C., Chavagnac, V., Olive, J-A., Leleu, T., Rommevaux, C., Escartín, J., Jamieson,  
1072 J., & Petersen S. (2015). Thermo-chemical fluxes, reactions and mixing in hydrothermal

1073 plumes at oceanic core complexes (Mid-Atlantic Ridge, 13°30'N and 13°20'N). Presented at  
1074 AGU Meeting, San Francisco, USA, 14-18 Dec. 2015

1075 Diamond, L.W., Tarantola, A., & Stünitz, H. (2010). Modification of fluid inclusions in quartz by  
1076 deviatoric stress II: experimentally induced changes in inclusion volume and composition.  
1077 *Contrib. Mineral. Petrol.* 160, 845–864. <https://doi.org/10.1007/s00410-010-0510-6>

1078 Dubessy, J., Poty, B., & Ramboz, C. (1989). Advances in C-O-H-N-S fluid geochemistry based on  
1079 micro-Raman spectrometric analysis of fluid inclusions. *European Journal of Mineralogy*,  
1080 1(4), 517–534. <https://doi.org/10.1127/ejm/1/4/0517>

1081 Dunn, R.A., Arai, R., Eason, D.E., Canales, J.P., & Sohn, R.A. (2017). Three-Dimensional Seismic  
1082 Structure of the Mid-Atlantic Ridge: An Investigation of Tectonic, Magmatic, and  
1083 Hydrothermal Processes in the Rainbow Area. *Journal of Geophysical Research: Solid  
1084 Earth*, 122(12), 9580–9602. <https://doi.org/10.1002/2017JB015051>

1085 Escartín, J., Mével, C., Petersen, S., Bonnemains, D., Cannat, M., Andreani, M., Augustin, N.,  
1086 Bezos, A., Chavagnac, V., Choi, Y., Godard, M., Haaga, K., Hamelin, C., Ildefonse, B., et  
1087 al. (2017). Tectonic structure, evolution, and the nature of oceanic core complexes and their  
1088 detachment fault zones (13°20'N and 13°30'N, Mid Atlantic Ridge): *Geochemistry*,  
1089 *Geophysics, Geosystems*, 18, (4), 1451–1482. <https://doi.org/10.1002/2016GC006775>

1090 Escartín, J., Mével, C., MacLeod, C.J., & McCaig, A.M. (2003). Constraints on deformation  
1091 conditions and the origin of oceanic detachments: The Mid-Atlantic Ridge core complex at  
1092 15°45'N. *Geochemistry, Geophysics, Geosystems*, 4(8), 1067.  
1093 <https://doi.org/10.1029/2001GC000278>

1094 Escartín, J., Smith, D.K., Cann, J., Schouten, H., Langmuir, C.H., & Escrig, S. (2008). Central role  
1095 of detachment faults in accretion of slow-spreading oceanic lithosphere. *Nature*, 455(7214),  
1096 790–794. <https://doi.org/10.1038/nature07333>

1097 Fontaine, F.J., & Wilcock, W.S.D. (2006). Dynamics and storage of brine in mid-ocean ridge  
1098 hydrothermal systems. *Journal of Geophysical Research*, 111, B06102.  
1099 <https://doi.org/10.1029/2005JB003866>

1100 Fontaine, F.J., Wilcock, W.S.D., & Butterfield, D.A. (2007). Physical controls on the salinity of  
1101 mid-ocean ridge hydrothermal vent fluids. *Earth and Planetary Science Letters*, 257, 132-  
1102 145. <https://doi:10.1016/j.epsl.2007.02.027>

1103 Fouquet, Y., Cambon, P., Etoubleau, J., Charlou, J.L., Ondréas, H., Barriga, F.J.A.S., Cherkashov,  
1104 G., Semkova, T., Poroshina, I., Bohn, M., Donval, J.P., Henry, K., Murphy, P., & Rouxel, O.  
1105 (2010). Geodiversity of Hydrothermal Processes Along the Mid-Atlantic Ridge and  
1106 Ultramafic-Hosted Mineralization: a New Type Of Oceanic Cu-Zn-Co-Au Volcanogenic  
1107 Massive Sulfide Deposit, *in* Diversity Of Hydrothermal Systems On Slow Spreading Ocean  
1108 Ridges, American Geophysical Union, p. 321–367

1109 Foustoukos, D.I. & Seyfried, W.E. (2005) Redox and pH constraints in the subseafloor root zone  
1110 of the TAG hydrothermal system, 26°N Mid-Atlantic Ridge. *Earth and Planetary Science*  
1111 *Letters*, 235, 497-510. <https://doi.org/10.1016/j.epsl.2005.04.042>

1112 Frezzotti, M.L., Ferrando, S., Tecce, F., & Castelli, D. (2012). Water content and nature of solutes  
1113 in shallow-mantle fluids from fluid inclusions. *Earth and Planetary Science Letters*, 351–  
1114 352, 70–83. <https://doi.org/10.1016/j.epsl.2012.07.023>

1115 Früh-Green, G.L., Kelley, D.S., Bernasconi, S.M., Karson, J.A., Ludwig, K.A., Butterfield, D.A.,  
1116 Boschi, C., & Proskurowski, G. (2003) 30,000 Years of Hydrothermal Activity at the Lost  
1117 City Vent Field. *Science*, 301, 495–498

1118 Gillis, K., & Thompson, G. (1993). Metabasalts from the Mid-Atlantic Ridge: new insights into  
1119 hydrothermal systems in slow-spreading crust. *Contrib. Mineral. Petrol.*, 113, 502-523

1120 Godard, M., Lagabrielle, Y., Alard, O., & Harvey, J. (2008). Geochemistry of the highly depleted  
1121 peridotites drilled at ODP Sites 1272 and 1274 (Fifteen-Twenty Fracture Zone, Mid-Atlantic  
1122 Ridge): Implications for mantle dynamics beneath a slow spreading ridge. *Earth and*  
1123 *Planetary Science Letters*, 267(3–4), 410–425. <https://doi.org/10.1016/j.epsl.2007.11.058>

1124 Hodgkinson, M.R.S., Webber, A.P., Roberts, S., Mills, R.A., Connelly, D.P., & Murton, B.J.  
1125 (2015). Talc-dominated seafloor deposits reveal a new class of hydrothermal system: *Nature*  
1126 *Communications*, 6, 10150. <https://doi.org/10.1038/ncomms10150>

1127 Holm, N.G., & Charlou, J.L. (2001). Initial indications of abiotic formation of hydrocarbons in the  
1128 Rainbow ultramafic hydrothermal system, Mid-Atlantic Ridge. *Earth Planet. Sci. Lett.*, 191,  
1129 1–8.

1130 Honnorez, J., Alt, J.C. & Humphris, S.E. (1998). Vivesection and autopsy of active and fossil  
1131 hydrothermal alteration of basalts beneath and within the TAG hydrothermal mound: Herzig,  
1132 P.M., Humphris, S.E., Miller, D.J., and Zierenberg, R.A. (Eds.), *Proceedings of the Ocean*  
1133 *Drilling Program, Scientific Results*, Vol. 158, p. 231-254



- 1134 Humphris, S.E., & Thompson, G. (1978). Hydrothermal alteration of oceanic basalts by seawater.  
1135 *Geochim. Cosmochim. Acta* 42, 107–125.
- 1136 Humphris, S.E., Alt, J.C., Teagle, D.A.H., & Honnorez, J.J. (1998). Geochemical changes during  
1137 hydrothermal alteration of basement in the stockwork beneath the active TAG hydrothermal  
1138 mound, *in* Proceedings of the Ocean Drilling Program, 158 Scientific Results, Ocean Drilling  
1139 Program, p. 255–276.
- 1140 Karson, J.A., Früh-Green, G.L., Kelley, D.S., Williams, E.A., Yoerger, D.R., & Jakuba, M. (2006).  
1141 Detachment shear zone of the Atlantis Massif core complex, Mid-Atlantic Ridge, 30°N.  
1142 *Geochemistry, Geophysics, Geosystems*, 7(6), Q06016.  
1143 <https://doi.org/10.1029/2005GC001109>
- 1144 Kelley, D.S., & Delaney, J.R. (1987). Two-phase separation and fracturing in mid-ocean ridge  
1145 gabbros at temperatures greater than 700 °C. *Earth. Planet. Sci. Lett.*, 83, 53-66
- 1146 Kelley, D.S., Gillis, K.M., & Thompson, G. (1993). Fluid evolution in submarine magma-  
1147 hydrothermal systems at the Mid-Atlantic Ridge. *Journal of Geophysical Research*, 98(B11),  
1148 19579–19596
- 1149 Kelley, D.S., & Robinson, P.T. (1990). Development of a brine-dominated hydrothermal system  
1150 at temperatures of 400–500 °C in the upper level plutonic sequence, Troodos ophiolite,  
1151 Cyprus. *Geochim. Cosmochim. Acta*, 54, 653–661
- 1152 Kelley, D. S., Robinson P. T., & Malpas, J. G. (1992). Processes of brine generation and circulation  
1153 in the oceanic crust: Fluid inclusion evidence from the Troodos Ophiolite, Cyprus. *J.*  
1154 *Geophys. Res*, 97, B6, 9307-9322.
- 1155 Klein, F., Grozeva, N.G., & Seewald, J.S. (2019). Abiotic methane synthesis and serpentinization  
1156 in olivine-hosted fluid inclusions. *Proceedings of the National Academy of Sciences*, 116(36),  
1157 17666–17672. <https://doi.org/10.1073/pnas.1907871116>
- 1158 Leisen, M., Boiron, M.C., Richard, A., & Dubessy, J. (2012). Determination of Cl and Br  
1159 concentrations in individual fluid inclusions by combining microthermometry and LA-  
1160 ICPMS analysis: Implications for the origin of salinity in crustal fluids. *Chemical Geology*,  
1161 330–331, 197–206. <https://doi.org/10.1016/j.chemgeo.2012.09.003>
- 1162 Locatelli, M., Verlaquet, A., Agard, P., Pettke, T., & Federico, L. (2019). Fluid pulses during  
1163 stepwise brecciation at intermediate subduction depths (Monviso eclogites, W. Alps): first

1164 internally then externally sourced, *Geochemistry, Geophysics, Geosystems*, 20(3).  
1165 <https://doi.org/10.1029/2019GC008549>

1166 Longerich, H. P., Jackson, S. E., & Gunther, D. (1996). Laser ablation inductively coupled plasma  
1167 mass spectrometric transient signal data acquisition and analyte concentration calculation. *J.*  
1168 *Anal. Atom. Spectrom.* 11, 899–904

1169 MacLeod, C.J., Escartín, J., Banerji, D., Banks, G.J., Gleeson, M., Irving, D.H.B., Lilly, R.M.,  
1170 McCaig, A., Niu, Y.-L., Allerton, S., & Smith, D.K. (2002). Direct geological evidence for  
1171 oceanic detachment faulting: The Mid-Atlantic Ridge, 15°45'N. *Geology*, 30(10), 279–282.

1172 MacLeod, C.J., Searle, R.C., Casey, J.F., Mallows, C., Unsworth, M., Achenbach, K., & Harris,  
1173 M. (2009). Life cycle of oceanic core complexes. *Earth and Planetary Science Letters*, 287,  
1174 333–344

1175 Mallows, C., & Searle, R.C. (2012). A geophysical study of oceanic core complexes and  
1176 surrounding terrain, Mid-Atlantic Ridge 13°N–14°N. *Geochemistry Geophysics Geosystems*,  
1177 13(1), Q0AG08. <https://doi.org/10.1029/2012GC004075>

1178 Martin, B., & Fyfe, W. S. (1970). Some experimental and theoretical observations on the kinetics  
1179 of hydration reactions with particular reference to serpentinization, *Chem. Geol.*, 6, 185–202.  
1180 [https://doi.org/10.1016/0009-2541\(70\)90018-5](https://doi.org/10.1016/0009-2541(70)90018-5).

1181 McCaig, A., Cliff, R.A., Escartín, J., Fallick, A.E., & MacLeod, C.J. (2007). Oceanic detachment  
1182 faults focus very large volumes of black smoker fluids. *Geology*, 35, 935–938.  
1183 <https://doi.org/10.1130/G23657A.1>

1184 McCaig, A.M., Delacour, A., Fallick, A.E., Castelain, T., & Früh-Green, G.L. (2010). Detachment  
1185 fault control on hydrothermal circulation systems: Interpreting the subsurface beneath the  
1186 TAG hydrothermal field using the isotopic and geological evolution of oceanic core  
1187 complexes in the Atlantic. *Geophysical Monograph Series*, 188, 207–239.  
1188 <https://doi.org/10.1029/2008GM000729>

1189 McCaig, A.M., & Harris, M. (2012). Hydrothermal circulation and the dike-gabbro transition in  
1190 the detachment mode of slow seafloor spreading. *Geology*, 40, 367-370

1191 McCollom, T.M. & Bach, W. (2009) Thermodynamic constraints on hydrogen generation during  
1192 serpentinization of ultramafic rocks. *Geochimica et Cosmochimica Acta*, 73, 856-875.  
1193 <https://doi.org/10.1016/j.gca.2008.10.032>

1194 McDermott, J.M., Seewald, J.S., German, C.R. & Sylva, S.P. (2015) Pathways for abiotic organic  
1195 synthesis at submarine hydrothermal fields. *PNAS*, *112*(25), 7668-7672. [https://doi.org](https://doi.org/10.1073/pnas.1506295112)  
1196 [/10.1073/pnas.1506295112](https://doi.org/10.1073/pnas.1506295112)

1197 McDermott, J.M., Sylva, S.P., Ono, S., German, C.R. & Seewald, J.S. (2018) Geochemistry of  
1198 fluids from Earth's deepest ridge-crest hot-springs: Piccard hydrothermal field, Mid-Cayman  
1199 Rise. *Geochimica and Cosmochimica Acta*, *228*, 95-118. [https://doi.org](https://doi.org/10.1016/j.gca.2018.01.021)  
1200 [/10.1016/j.gca.2018.01.021](https://doi.org/10.1016/j.gca.2018.01.021)

1201 Monnin, C., Chavagnac, V., Boulart, C., Ménez, B., Gérard, M., Gérard, E., Quéméneur M., Erauso  
1202 G., Postec A., Guentas-Dombrowski L., Payri C., & Pelletier B. (2014). The low temperature  
1203 hyperalkaline hydrothermal system of the Prony Bay (New Caledonia). *Biogeosciences*  
1204 *Discussion*, *11*, 5687-5706. <https://doi:10.5194/bg-11-5687-2014>

1205 Mottl, M.J. (1983). Metabasalts, axial hot springs, and the structure of hydrothermal systems at  
1206 mid- ocean ridges. *Geol. Soc. Am. Bull.* *94*, 161–180

1207 Olive, J.A., Parnell-Turner, R., Escartin, J., Smith, D.K., & Petersen, S. (2019). Controls on the  
1208 seafloor exposure of detachment fault surfaces. *Earth and Planetary Science Letters*, *506*,  
1209 381-387. <https://doi.org/10.1016/j.epsl.2018.11.001>

1210 Ondréas, H., Cannat, M., Fouquet, Y., & Normand, A. (2012). Geological context and vents  
1211 morphology of the ultramafic-hosted Ashadze hydrothermal areas (Mid-Atlantic Ridge  
1212 13°N). *Geochemistry Geophysics Geosystems*, *13*(1), Q0AG14.  
1213 <https://doi.org/10.1029/2012GC004433>

1214 Parnell-Turner, R., White, N., Henstock, T.J., Jones, S.M., MacLennan, J., & Murton, B.J. (2017).  
1215 Causes and Consequences of Diachronous V-Shaped Ridges in the North Atlantic Ocean.  
1216 *Journal of Geophysical Research: Solid Earth*, *122*(11), 8675–8708.  
1217 <https://doi.org/10.1002/2017JB014225>

1218 Parnell-Turner, R., Escartín, J., Olive, J.-A., Smith, D.K., & Petersen, S. (2018). Genesis of  
1219 corrugated fault surfaces by strain localization recorded at oceanic detachments. *Earth and*  
1220 *Planetary Science Letters*, *498*, 116–128. <https://doi.org/10.1016/j.epsl.2018.06.034>

1221 Pasteris, J.D., Wopenka, B., & Seitz, J.C. (1988). Practical aspects of quantitative laser Raman  
1222 microprobe spectroscopy for the study of fluid inclusions. *Geochimica et Cosmochimica*  
1223 *Acta*, *52*, 979–988

1224 Paulick, H., Bach, W., Godard, M., de Hoog, J.C.M., Suhr, G., & Harvey, J. (2006). Geochemistry  
1225 of abyssal peridotites (Mid-Atlantic Ridge, 15°20'N, ODP Leg 209): implications for fluid-  
1226 rock interaction in slow spreading environments. *Chemical Geology*, 234(3-4), 179-210

1227 Pearce, N. J. G., Perkins, W. T., Westgate, J. A., Gorton, M. P., Jackson, S. E., Nael, C. R. &  
1228 Chenery, S. P. (1997). Compilation of new and published major trace element data for NIST  
1229 610 NIST SRM 612 glass reference materials. *Geostand. Newslett.* 21, 115–144.

1230 Pertsev, A.N., Bortnikov, N.S., Vlasov, E.A., Beltenev, V.E., Dobretsova, I.G., & Ageeva, O. A.  
1231 (2012). Recent massive sulfide deposits of the Semenov ore district, Mid-Atlantic Ridge,  
1232 13°31' N: Associated rocks of the oceanic core complex and their hydrothermal alteration.  
1233 *Geology of Ore Deposits*, 54(5), 334–346. <https://doi.org/10.1134/S1075701512050030>.

1234 Petersen, S., Hertzog, M., & Hannington, M.D. (1998). Fluid inclusion studies as a guide to the  
1235 temperature regime within the TAG hydrothermal mound, 26°, Mid-Atlantic Ridge. In P.M.  
1236 Hertzog, S.E. Humphris, D.J. Miller, R.A. Zierenberg (Eds.), *Proceedings of the Ocean*  
1237 *Drilling Program, Scientific Results* (vol. 158, pp. 163-178).

1238 Petersen, S., Kuhn, K., Kuhn, T., Augustin, N., Hekinian, R., Franz, L., & Borowski, C. (2009).  
1239 The geological setting of the ultramafic-hosted Logatchev hydrothermal field (14°45'N,  
1240 Mid-Atlantic Ridge) and its influence on massive sulfide formation. *Lithos*, 112(1-2), 40-56.  
1241 <https://doi.org/10.1016/j.lithos.2009.02.008>

1242 Raimbourg, H., Thiéry, R., Vacelet, M., Ramboz, C., Cluzel, N., Le Trong, E., Yamaguchi, A., &  
1243 Kimura, G. (2014). A new method of reconstituting the P-T conditions of fluid circulation in  
1244 an accretionary prism (Shimanto, Japan) from microthermometry of methane-bearing  
1245 aqueous inclusions. *Geochim. Cosmochim. Acta* 125, 96–109.  
1246 <http://dx.doi.org/10.1016/j.gca.2013.09.025>.

1247 Roedder, E. (1984). Fluid Inclusions. Reviews in Mineralogy, Vol. 12, Mineralogical Society of  
1248 America, 644 p.

1249 Saccocia, P.J., & Gillis, K.M. (1995). Hydrothermal upflow zones in the oceanic crust. *Earth and*  
1250 *Planetary Science Letters*, 136, 1–16

1251 Scheuermann, P.P., Tan, C. & Seyfried, W.E. (2018) Quartz solubility in the two-phase region of  
1252 the NaCl-H<sub>2</sub>O system: an experimental study with application to the Piccard hydrothermal  
1253 field, Mid-Cayman Rise. *Geochemistry, Geophysics, Geosystems*, 19, 3570-3582.  
1254 <https://doi.org/10.1029/2018GC007610>.

- 1255 Scheuermann, P.P., Xing, Y., Ding, K. & Seyfried, W.E. (2020) Experimental measurement of  
1256 H<sub>2</sub>(aq) solubility in hydrothermal fluids: application to the Piccard hydrothermal field, Mid-  
1257 Cayman Rise. *Geochemica and Cosmochimica Acta*, (283), 22-39.  
1258 <https://doi.org/10.1016/j.gca.2020.05.020>.
- 1259 Schmidt, K., Garbe-Schönberg, D., Koschinsky, A., Strauss, H., Jost, C. L., Klevenz, V., &  
1260 Königer P. (2011). Fluid elemental and stable isotope composition of the Nibelungen  
1261 hydrothermal field (8°18'S, Mid-Atlantic Ridge): constraints on fluid–rock interaction in  
1262 heterogeneous lithosphere. *Chem. Geol.*, 280, 1–18.
- 1263 Schroeder, T., & John, B.E. (2004). Strain localization on an oceanic detachment fault system,  
1264 Atlantis Massif, 30°N, Mid-Atlantic Ridge. *Geochemistry, Geophysics, Geosystems*, 5(11),  
1265 Q11007. <https://doi.org/10.1029/2004GC00728>.
- 1266 Seyfried, W.E., Foustoukos, D.I. & Fu, Q. (2007) Redox evolution and mass transfer during  
1267 serpentinization: An experimental and theoretical study at 200 degrees C, 500 bar with  
1268 implications for ultramafic-hosted hydrothermal systems at Mid-Ocean Ridges. *Geochimica*  
1269 *Et Cosmochimica Acta*, 71, 3872-3886. <https://doi.org/10.1016/j.gca.2007.05.015>
- 1270 Simão, N.M., Peirce, C., Funnell, M.J., Robinson, A.H., Searle, R.C., MacLeod, C.J., & Reston,  
1271 T.J. (2020). 3-D P-wave velocity structure of oceanic core complexes at 13°N on the Mid-  
1272 Atlantic Ridge. *Geophysical Journal International*, 221(3), 1555–1579.  
1273 <https://doi.org/10.1093/gji/ggaa093>
- 1274 Simonov, V.A., Borovikov, A.A., Kotlyarov, A.V., Amplieva, E.E., & Bortnikov, N.S. (2015). *LA-*  
1275 *ICP-MS evidence for high concentrations of metals in fluid from modern sea-floor*  
1276 *hydrothermal systems: a case study of fluid inclusions in minerals from Semenov, Ashadze,*  
1277 *and Logatchev sulfide edifices (Mid-Atlantic Ridge)*. Paper presented at the proceedings of  
1278 the 13<sup>th</sup> biennial SGA meeting, 24-27 August 2015, Nancy, France
- 1279 Smith, D.K., Cann, J.R., & Escartín, J. (2006). Widespread active detachment faulting and core  
1280 complex formation near 13° N on the Mid-Atlantic Ridge. *Nature*, 442(7101), 440–443.  
1281 <https://doi.org/10.1038/nature04950>
- 1282 Smith, D.K., Escartín, J., Schouten, H., & Cann, J.R. (2008). Fault rotation and core complex  
1283 formation: Significant processes in seafloor formation at slow-spreading mid-ocean ridges  
1284 (Mid-Atlantic Ridge, 13 –15° N). *Geochemistry, Geophysics, Geosystems*, 9(3), Q03003.  
1285 <https://doi.org/10.1029/2007GC001699>

1286 Son, J., Pak, S.-J., Kim, J., Baker, E.T., You, O.-R., Son, S., & Moon, J. (2014). Tectonic and  
1287 magmatic control of hydrothermal activity along the slow-spreading Central Indian Ridge,  
1288 8°S-17°S. *Geochemistry, Geophysics, Geosystems*, 15(5), 2011–2020.  
1289 <https://doi.org/10.1002/2013GC005206>

1290 Sourirajan, S. & Kennedy, G.C. (1962). The system H<sub>2</sub>O–NaCl at elevated temperatures and  
1291 pressures, *Am. J. Sci.*, 260, 115–141.

1292 Spandler, C., Pettke, T., & Rubatto, D. (2011). Internal and external fluid sources for eclogite-  
1293 facies veins in the Monviso meta-ophiolite, Western Alps: Implications for fluid flow in  
1294 subduction zones. *Journal of Petrology*, 52(6), 1207–1236.  
1295 <https://doi.org/10.1093/petrology/egr025>

1296 Steele-MacInnis, M., Bodnar, R.J., & Naden, J. (2011). Numerical model to determine the  
1297 composition of H<sub>2</sub>O–NaCl–CaCl<sub>2</sub> fluid inclusions based on microthermometric and  
1298 microanalytical data. *Geochimica et Cosmochimica Acta*, 75(1), 21–40.  
1299 <https://doi.org/10.1016/j.gca.2010.10.002>

1300 Tao, C., Seyfried, W.E., Lowell, R.P., Liu, Y., Liang, J., Guo, Z., Ding, K., Zhang, H., Liu, J., Qiu,  
1301 L., Egorov, I., Liao, S., Zhao, M., Zhou, J., et al. (2020). Deep high-temperature  
1302 hydrothermal circulation in a detachment faulting system on the ultra-slow spreading ridge.  
1303 *Nature Communications*, 11(1), 1300. <https://doi.org/10.1038/s41467-020-15062-w>

1304 Tarantola, A., Diamond, L.W., & Stünitz, H. (2010). Modification of fluid inclusions in quartz by  
1305 deviatoric stress. I: experimentally induced changes in inclusion shapes and microstructures.  
1306 *Contrib. Mineral. Petrol.*, 160, 825–843.

1307 Tarantola, A., Diamond, L.W., Stünitz, H., Thust, A., & Pec, M. (2010). Modification of fluid  
1308 inclusions in quartz by deviatoric stress. III: influence of principal stresses on inclusion  
1309 density and orientation. *Contrib. Mineral. Petrol.*, 164, 537-550.

1310 Tivey, M.K., Mills, R.A., & Teagle, D.A.H. (1998). Temperature and salinity of fluid inclusions  
1311 in anhydrite as indicators of seawater entrainment and heating in the TAG active mound. In:  
1312 Herzig PM, Humphris SE, Miller DJ, Zierenberg RA (eds) *Proceedings of the ocean drilling  
1313 program, scientific results, vol 158*. Ocean drilling program, College Station, 179–190

1314 Touret, J.L.R. (2001). Fluids in metamorphic rocks. *Lithos* 55(1-4), 1-25.  
1315 [https://doi.org/10.1016/S0024-4937\(00\)00036-0](https://doi.org/10.1016/S0024-4937(00)00036-0)

- 1316 Tucholke, B.E., Behn, M.D., Buck, W.R., & Lin, J. (2008). Role of melt supply in oceanic  
1317 detachment faulting and formation of megamullions. *Geology*, 36(6), 455–458.  
1318 <https://doi.org/10.1130/G24639A>
- 1319 Van den Kerkhof, A.M., & Hein, U.F. (2001). Fluid inclusion petrography. *Lithos*, 55(1–4), 27–  
1320 47. [https://doi.org/10.1016/S0024-4937\(00\)00037-2](https://doi.org/10.1016/S0024-4937(00)00037-2)
- 1321 Vanko, D.A. (1988). Temperature, pressure, and composition of hydrothermal fluids with their  
1322 bearing on the magnitude of tectonic uplift at mid-ocean ridges, inferred from fluid inclusions  
1323 in oceanic layer 3 rocks. *J. Geophys. Res.*, 93, 4595-4611
- 1324 Vanko, D. A., Wolfgang, B., Roberts, S., Yeats, C.J., & Scott, S.D. (2004). Fluid inclusion  
1325 evidence for subsurface phase separation and variable fluid mixing regimes beneath the deep-  
1326 sea PACMANUS hydrothermal field, Manus Basin back arc rift, Papua New Guinea. *Journal*  
1327 *of Geophysical Research*, 109(B3), B03201. <https://doi.org/10.1029/2003JB002579>
- 1328 Vidal, O., De Andrade, V., Lewin, E., Munoz, M., Parra, T., & Pascarelli, S. (2006). P-T-  
1329 deformation-Fe<sup>3+</sup>/Fe<sup>2+</sup> mapping at the thin section scale and comparison with XANES  
1330 mapping: application to a garnet-bearing metapelite from the Sambagawa metamorphic belt  
1331 (Japan). *J. Metamorph. Geol.*, 24(7), 669–683
- 1332 Vidal, O., & Parra, T. (2000). Exhumation paths of high-pressure metapelites obtained from local  
1333 equilibria for chlorite-phengite assemblages. *Geol. J.* 35(3–4), 139–161
- 1334 Vidal, O., Parra, T., & Trotet, F. (2001). A thermodynamic model for Fe-Mg aluminous chlorite  
1335 using data from phase equilibrium experiments and natural pelitic assemblages in the 100–  
1336 600 °C, 1–25 kb range. *Am. J. Sci.*, 301(6), 557–592
- 1337 Vidal, O., Parra, T., & Vieillard, P. (2005). Thermodynamic properties of the Tschermak solid  
1338 solution in Fe-chlorite: application to natural examples and possible role of oxidation. *Am.*  
1339 *Mineral.*, 90(2–3), 347–358
- 1340 Vityk, M.O., & Bodnar, R.J. (1995). Textural evolution of synthetic fluid inclusions in quartz  
1341 during reequilibration, with applications to tectonic reconstruction. *Contrib. Mineral. Petrol.*  
1342 121, 309–323.
- 1343 Walshe, J-L. (1986). A six-component chlorite solid solution model and the conditions of chlorite  
1344 formation in hydrothermal and geothermal systems. *Econ. Geol.*, 81, 681-703

- 1345 Wetzel, L.R., & Shock, E.L. (2000). Distinguishing ultramafic- from basalt-hosted submarine  
1346 hydrothermal vent fluid compositions. *Journal of Geophysical Research*, 105(B4), 8319–  
1347 8340
- 1348 Wilson, S.C., Murton, B.J., & Taylor, R.N. (2013). Mantle composition controls the development  
1349 of an Oceanic Core Complex. *Geochemistry, Geophysics, Geosystems*, 14, 1–18.  
1350 <https://doi.org/10.1002/ggge.20046>.
- 1351 Zhang, Y.G., & Frantz, J.D. (1987). Determination of the homogenization temperatures and  
1352 densities of supercritical fluids in the system NaCl-KCl-CaCl<sub>2</sub>-H<sub>2</sub>O using synthetic fluid  
1353 inclusions. *Chemical Geology*, 64, 335-350.
- 1354



1355 **Tables**

1356

1357 **Table 1.** Characteristics of the six fault rocks considered for this study. The outcrop numbers refer to Figure 1b and to Bonnemains et  
 1358 al. (2017).

1359

Outcrop	Sample # ODM_ROC_ Referred to as	IGSN	Latitude	Longitude	Depth (m)	Rock type	Texture	Mineralogical composition*	Quartz content	Analyses		
										Whole rock	Chlorite	Fluid Inclusions
1	V547_115 ODM115	CNRS0000000115	13°18.96' N	-44°53.43' W	3159	mafic	clast of breccia with vacuoles	Chl, Pl, Px, Pmp	absent	x	x	
2	V552_217 ODM217	CNRS0000000221	13°19.22' N	-44°53.31' W	3113	mafic / ultramaf ic	matrix-supported breccia with a striated surface and 4 slip zones	<i>clast:</i> Tlc / Chl ± Ttn <i>matrix:</i> Tlc, Amp, Srp	absent	x	x	
	V552_218 ODM218	CNRS0000000222	13°19.22' N	-44°53.28' W	3133	mafic	matrix-supported breccia with a striated surface and 6 slip zones	<i>clast:</i> Chl ± Ttn / Chl + Qz ± Sulf (Py, Po, Ccp) <i>matrix:</i> Qz + Chl + Sulf (Py, Po, Ccp)	high	x	x	x
3	V551_173 ODM173	CNRS0000000176	13°20.40' N	-44°54.03' W	3218	mafic / ultramaf ic	matrix-supported breccia with one side mostly matrix and the other containing clasts	<i>clast:</i> Tlc, Amp / Chl ± Ttn <i>matrix:</i> Tlc, Chl ± Qz ± Sulf (Py, Po)	high on matrix- supported side, mo- derate on the other	x	x	x
4	V551_195 ODM195	CNRS0000000199	13°19.51' N	-44°53.75' W	2922	mafic	clast-supported breccia	<i>clast:</i> Pl + Amp + Chl <i>matrix:</i> fine-grained with sub- mm clasts and rare Chl and Qz grains	moderate	x	x	x
6	V550_155 ODM155	CNRS0000000157	13°19.40' N	-44°54.04' W	3104	mafic	matrix-supported breccia with a striated surface and 5 slip zones	<i>clast:</i> Chl ± Ttn / Chl + Qz ± Sulf (Py) <i>matrix:</i> Qz + Chl + Sulf (Py)	high	x	x	x

1360 \* Mineral abbreviations: Amp, amphibole; Ccp, chalcopyrite; Chl, chlorite; Pl, plagioclase; Pmp, pumpellyite; Px, pyroxene; Py, pyrite; Po, pyrrhotite; Qz, quartz; Srp, serpentine; Ttn, titanite; Sulf, sulfide;  
 1361 Tlc, talc

1362

1363

1364

1365

1366

1367

1368

1369

1370 **Table 2.** Major and selected trace element whole-rock analyses of mafic and mixed mafic-ultramafic breccias from the detachment fault  
 1371 surface (see Table S1 for full analyses).  
 1372

Nature Degree of silicification		Basaltic clast Qz free	Mafic Moderately Si	Mafic Highly Si	Mafic Highly Si	Mafic Highly Si	Mafic Highly Si	Mixed Qz free	Mixed Qz free	Mixed Qz free	Mixed Moderately Si	Mixed Moderately Si	Mixed Moderately Si
Sample		ODM115	ODM195	ODM218a	ODM218b	ODM218 wr	ODM155	ODM217a	ODM217b	ODM217 wr	ODM173a	ODM173b	ODM173 wr
SiO <sub>2</sub>	wt.%	51.81	49.16	84.35	62.40	65.72	79.27	49.41	55.08	48.90	55.64	57.37	68.25
Al <sub>2</sub> O <sub>3</sub>	wt.%	13.76	13.05	2.69	4.12	3.78	2.43	5.46	2.26	5.25	9.05	1.50	5.18
Fe <sub>2</sub> O <sub>3</sub>	wt.%	8.16	10.76	6.30	19.97	17.09	9.47	11.25	8.07	12.50	13.79	10.04	11.07
MnO	wt.%	0.16	0.22	0.06	0.08	0.08	0.06	0.33	0.39	0.45	0.11	0.07	0.07
MgO	wt.%	6.08	11.88	2.43	4.33	4.08	2.10	22.70	22.93	21.30	11.24	20.49	8.18
CaO	wt.%	11.27	4.57	0.28	0.48	0.30	0.28	4.32	6.72	5.33	0.24	0.09	0.17
Na <sub>2</sub> O	wt.%	3.78	1.23	< D.L.	0.11	0.07	0.05	0.22	0.20	0.24	0.29	0.28	0.17
K <sub>2</sub> O	wt.%	0.09	0.04	< D.L.	< D.L.	< D.L.	0.02	0.03	0.03	0.04	0.04	0.03	0.03
TiO <sub>2</sub>	wt.%	1.37	0.65	0.17	0.27	0.26	0.15	0.42	0.12	0.40	0.49	< D.L.	0.26
P <sub>2</sub> O <sub>5</sub>	wt.%	0.16	< D.L.	< D.L.	< D.L.	< D.L.	< D.L.	0.06	< D.L.	0.05	0.05	< D.L.	0.04
PF	wt.%	3.03	7.22	3.44	7.72	7.77	6.67	6.39	4.86	6.52	9.18	10.28	6.24
<b>Total</b>	wt.%	99.65	98.79	99.71	99.48	99.14	100.49	100.60	100.67	100.97	100.11	100.15	99.66
<b>Mg #</b>		59.61	68.62	43.26	30.05	32.11	30.51	80.00	84.91	77.15	61.74	80.18	59.41
FeO	wt.%	4.74	5.54	5.50	14.46	12.49	3.51	8.01	5.61	8.85	7.45	5.75	6.14
S	wt.%	0.04	0.04	1.04	7.68	6.21	4.75	0.02	0.03	0.02	0.66	0.69	1.98
Cr	ppm	308.50	349.30	293.70	590.40	525.60	303.30	1826.00	1895.00	2070.00	934.30	3319.00	1214.00
Cu	ppm	66.84	11.68	87.36	564.10	697.30	19.05	874.20	450.80	1540.00	504.20	1609.00	605.20
Ni	ppm	112.80	126.40	140.40	492.70	385.90	190.70	1080.00	1180.00	1064.00	429.50	1609.00	710.70
Zn	ppm	60.02	105.60	45.73	56.51	64.18	33.78	139.50	115.00	161.80	237.90	2947.00	379.70

<D.L.: lower than detection limit. Qz: quartz; Highly Si: highly silicified

1373  
 1374  
 1375 **Table 3.** Microthermometric measurements in fluid inclusions and Raman spectroscopy results.  
 1376

Sample	Quartz location	Nb	Th (°C)			Salinity (wt.% NaCl eq.)			Gases other than H <sub>2</sub> O in fluid inclusions, analyzed by Raman spectroscopy
			Range	Average	SD	Range	Average	SD	
ODM195	Matrix	19	149-218	182	16	4.3-5.9	5.2	0.5	12 FI studied – no gas detected
ODM155	All	24	183-322	263	25	3.5-5.9	4.8	0.3	
	- Matrix	14	197-286	258	24	4.3-5.9	4.9	0.4	17 FI studied – 2 with CO <sub>2</sub> only
	- Clasts	10	183-322	271	23	3.5-5.3	4.7	0.3	
ODM218b	All	30	260-336	318	9	4.8-10.2	7.6	0.9	28 FI studied – 7 with H <sub>2</sub> only. 6 with H <sub>2</sub> +CO <sub>2</sub> . 2 with H <sub>2</sub> +CH <sub>4</sub>
	- Matrix	6	260-329	305	25	6.2-6.9	6.4	0.3	
	- Clasts	24	310-336	321	5	4.8-10.2	7.9	0.8	
ODM218c	Matrix	36	258-348	317	12	2.4-6.2	4.3	0.8	21 FI studied – 11 with H <sub>2</sub> only. 1 with H <sub>2</sub> +CO <sub>2</sub> . 3 with H <sub>2</sub> +CH <sub>4</sub> . 2 with H <sub>2</sub> +CO <sub>2</sub> +CH <sub>4</sub> . 4 with H <sub>2</sub> +CO <sub>2</sub> +CH <sub>4</sub> +H <sub>2</sub> S
ODM173	Matrix	10	153-177	176	13	3.9-6.4	4.6	0.8	

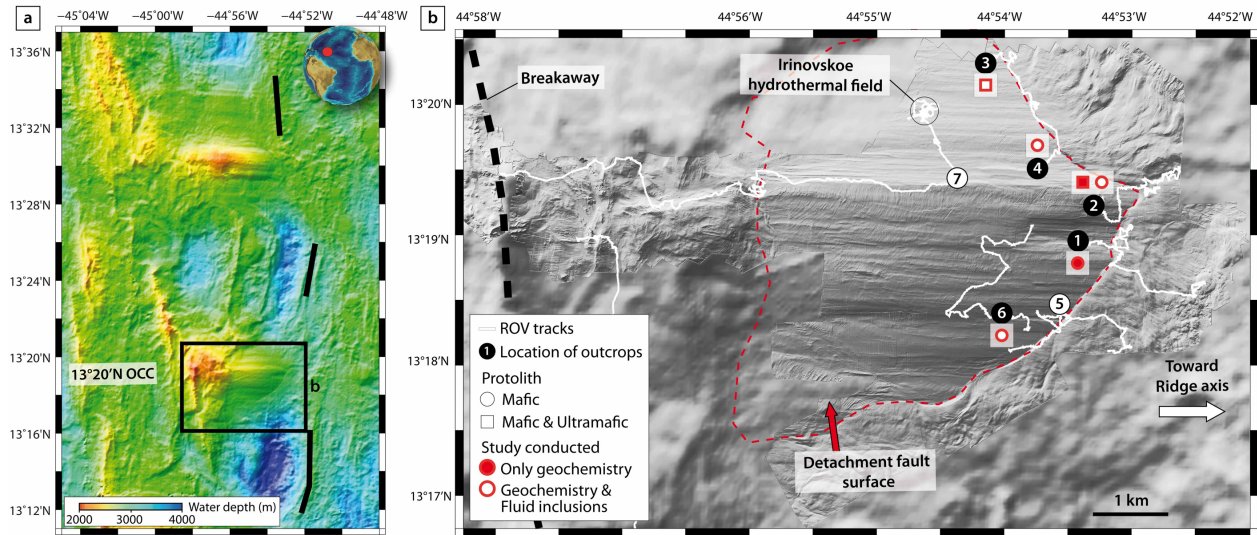
Nb: number of fluid inclusions; SD: standard deviation

1377  
 1378

1379 **Figures**

1380

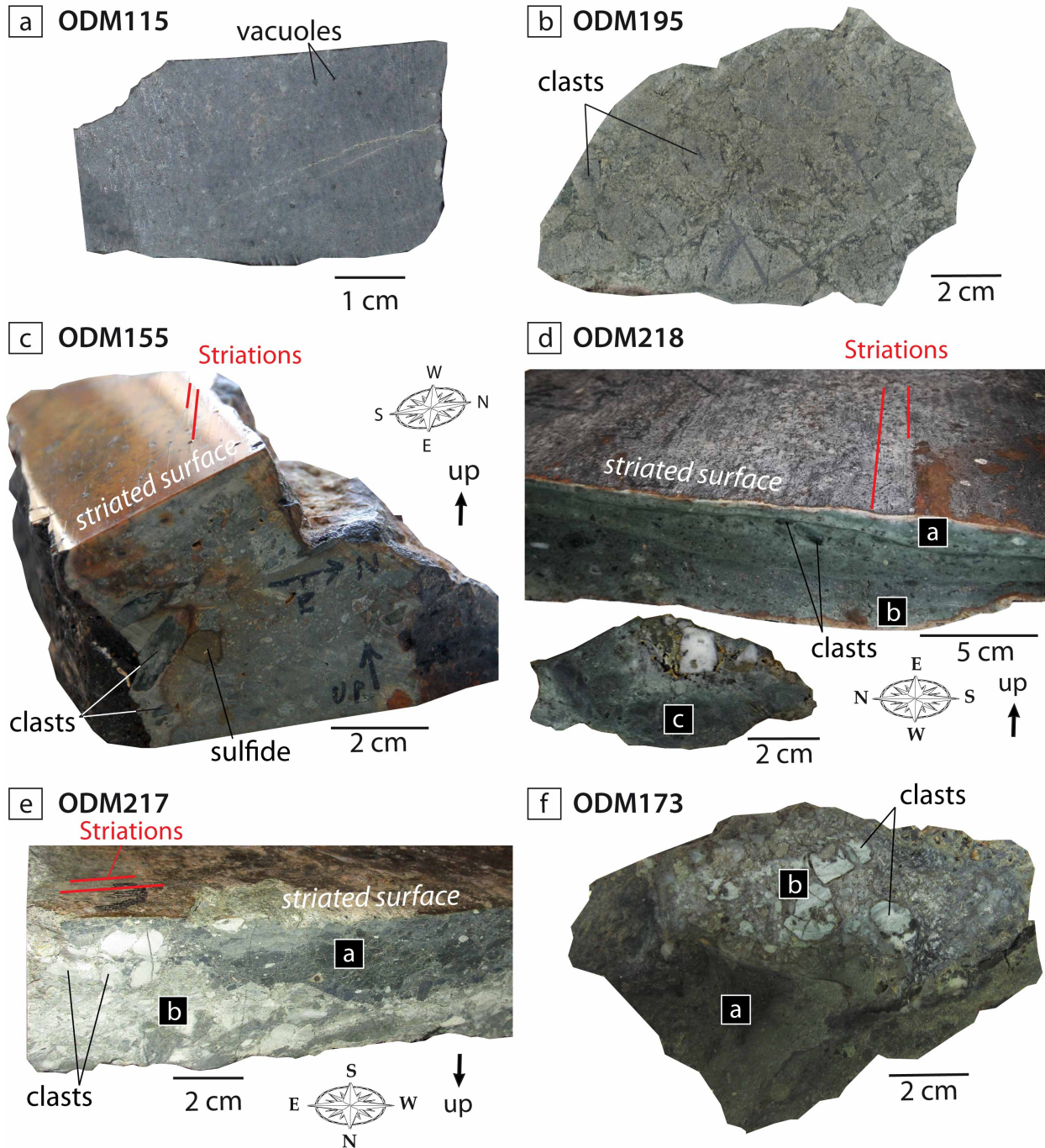
1381



1382

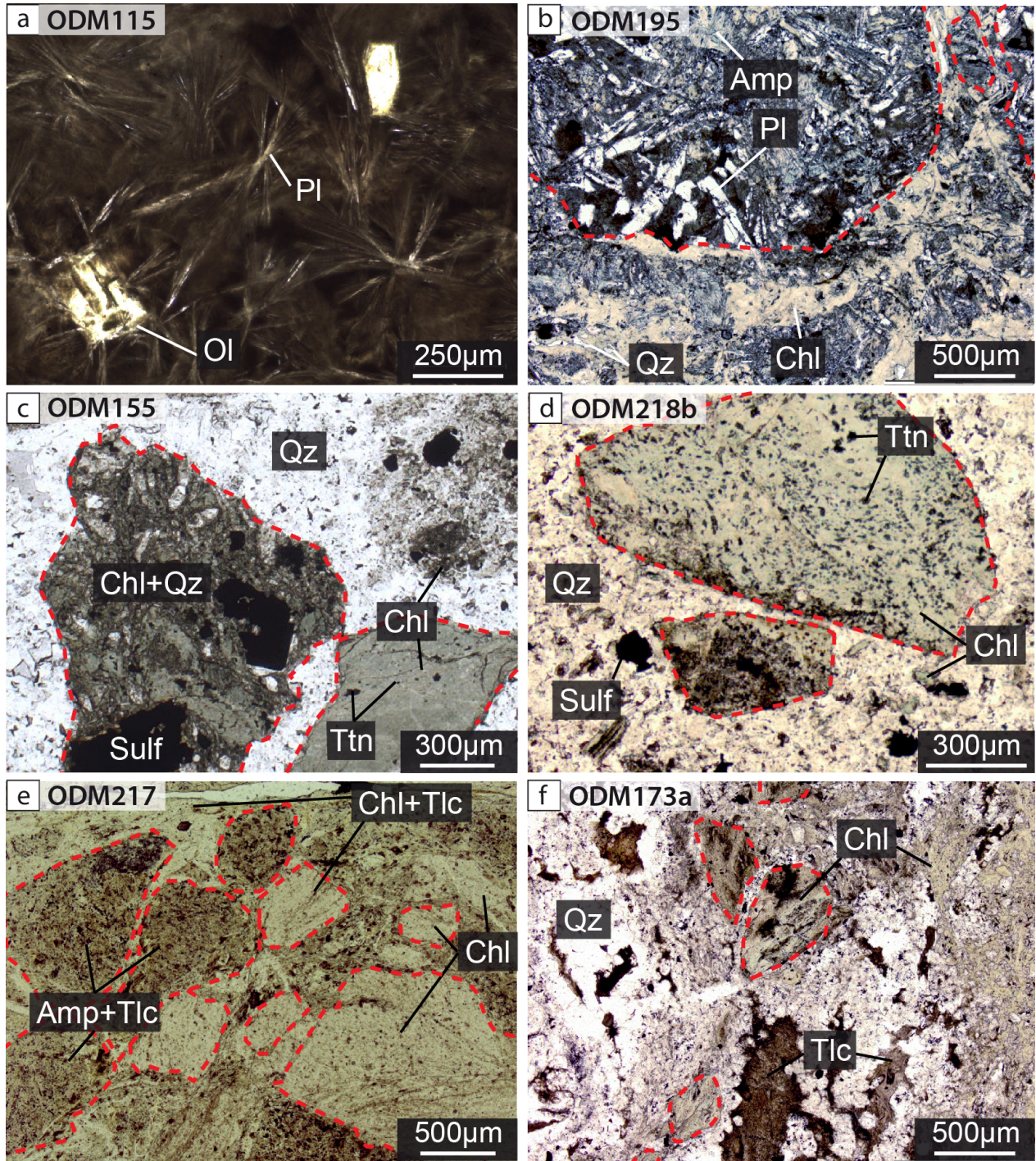
1383 **Figure 1:** (a) Multibeam bathymetry data of the 13°20'N detachment region, showing the core  
1384 complex (black box) and the ridge axis (thick black lines). (b) Shaded relief microbathymetry  
1385 acquired with the AUV Abyss (GEOMAR), collected during the ODEMAR cruise  
1386 (<https://doi.org/10.17600/13030070>) over the 13°20'N OCC, complemented with shipboard  
1387 bathymetry. White lines are tracks of ten ROV dives. Fault surface outcrops identified and sampled  
1388 with the ROV are shown by a circle (see Bonnemains et al., 2017). Samples used for this study  
1389 come from five of them (black numbered circles and associated red symbols, see **Table 1** for  
1390 details).

1391



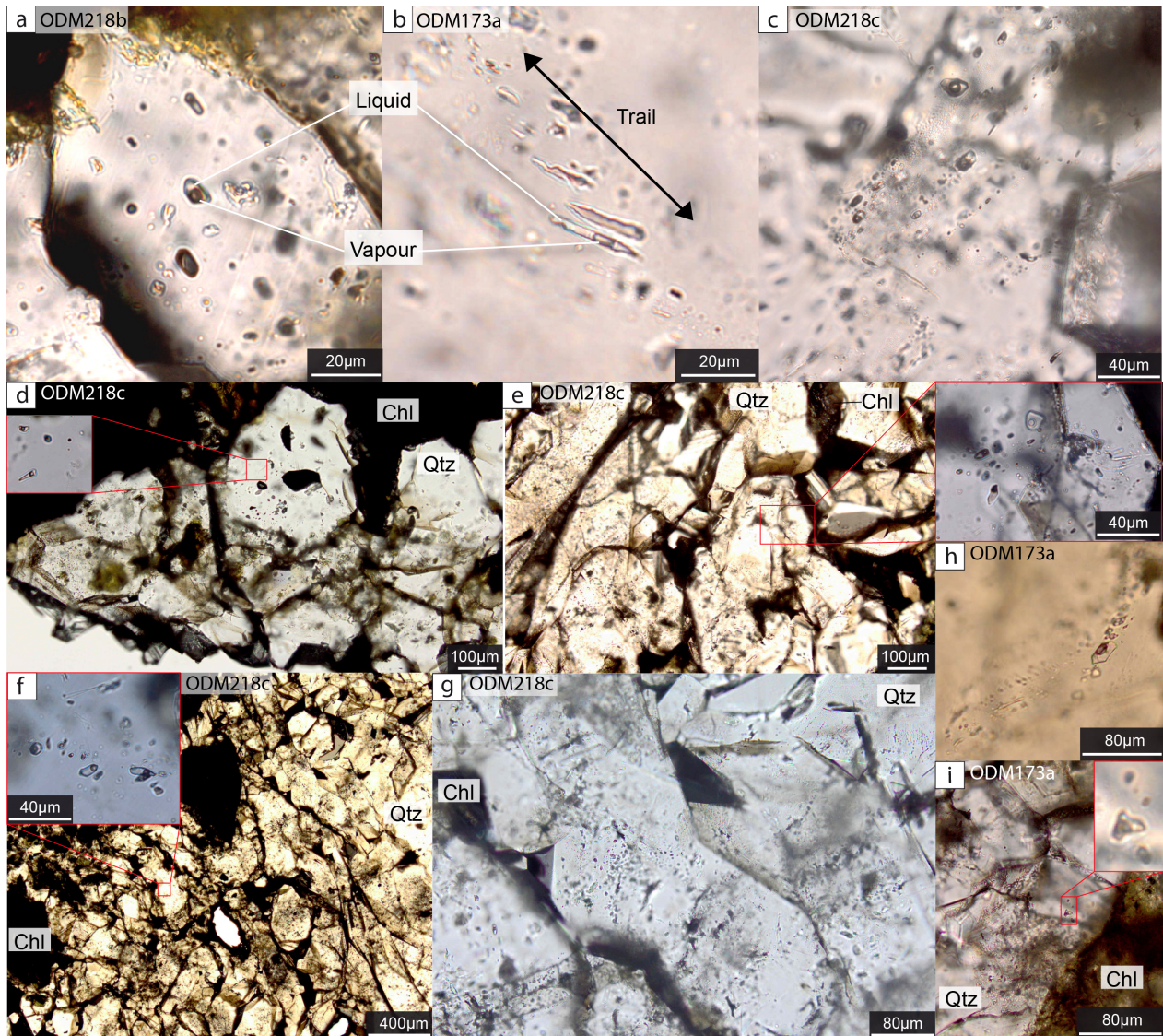
1392  
 1393 **Figure 2:** Macro-photographs of the studied fault rocks. (a) Clast of metabasalt with no quartz  
 1394 ODM115. (b) Moderately silicified mafic breccia ODM195. (c) Highly silicified mafic breccia  
 1395 ODM155. (d) Highly silicified mafic breccia ODM218 that is distinguished in two parts  
 1396 (subsamples a and b) at different distance from the striated surface (or slip plane) and a fragment  
 1397 dislodged from the lower part of sample (subsample ODM218c). (e) Unsilicified mafic-ultramafic  
 1398 breccia ODM217. We identify two parts based on the difference in color and mineralogical

1399 composition between these slip layers. (f) Silicified mafic-ultramafic breccia ODM173 with  
1400 ODM173a richer in quartz than ODM173b. All samples were recovered in situ at the detachment  
1401 fault zone.  
1402



1403  
 1404 **Figure 3:** Microphotographs of studied samples in plane polarized light. (a) Unsilicified mafic  
 1405 clast showing basaltic texture with radiating plagioclase (Pl) laths and dendritic olivine (Ol)  
 1406 crystals. (b) Moderately silicified mafic breccia contains clasts displaying a doleritic texture, made  
 1407 of amphibole (Amp) + plagioclase ± chlorite (Chl), surrounded by a matrix consisting of crushed  
 1408 clasts mixed with chlorite and quartz (Qz). (c, d) Highly silicified mafic breccias containing clasts

1409 of chlorite ± titanite (Ttn) and chlorite ± quartz ± sulfide (Sulf), in a matrix mainly composed of  
 1410 quartz and minor chlorite and sulfide. In one of the clasts (c), the doleritic texture is still visible.  
 1411 (e) Unsilicified and (f) silicified mafic-ultramafic breccias containing both mafic (made of chlorite  
 1412 ± titanite) and ultramafic (made of talc, Tlc, and amphibole) clasts embedded in a matrix composed  
 1413 of chlorite and talc, in addition to quartz for sample (f). (e) corresponds to zone a in Figure 2f.  
 1414 Clasts are delimited by red dotted lines.  
 1415



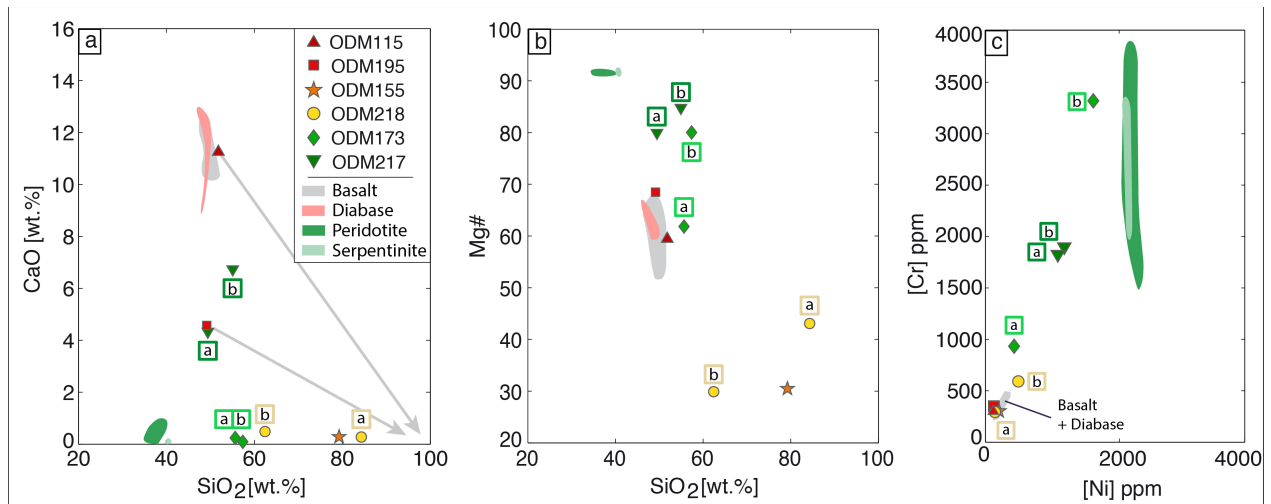
1416  
 1417 **Figure 4:** Microphotographs of representative two-phase (liquid and vapor) fluid inclusions in  
 1418 quartz grains. Clustered fluid inclusions with similar vapor/liquid ratios are considered as primary  
 1419 (a, d; e; i); fluid inclusions organized in trails are considered as secondary inclusions (b, c, f, g, h).

1420 Note that most trails are intragrain trails, restricted to one quartz grain, while only few trails  
 1421 crosscut several quartz grain boundaries (g). Qtz: quartz; Chl: chlorite.

1422

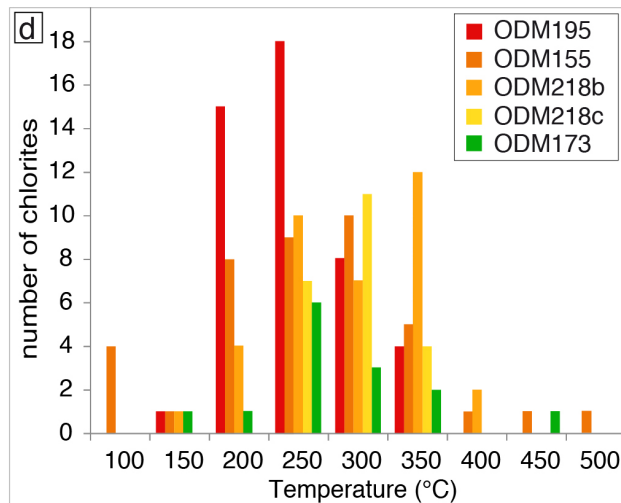
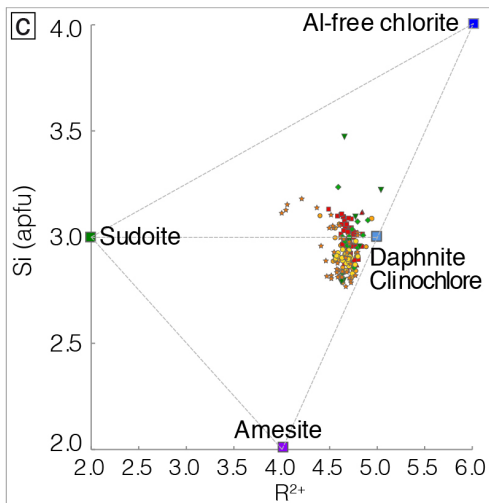
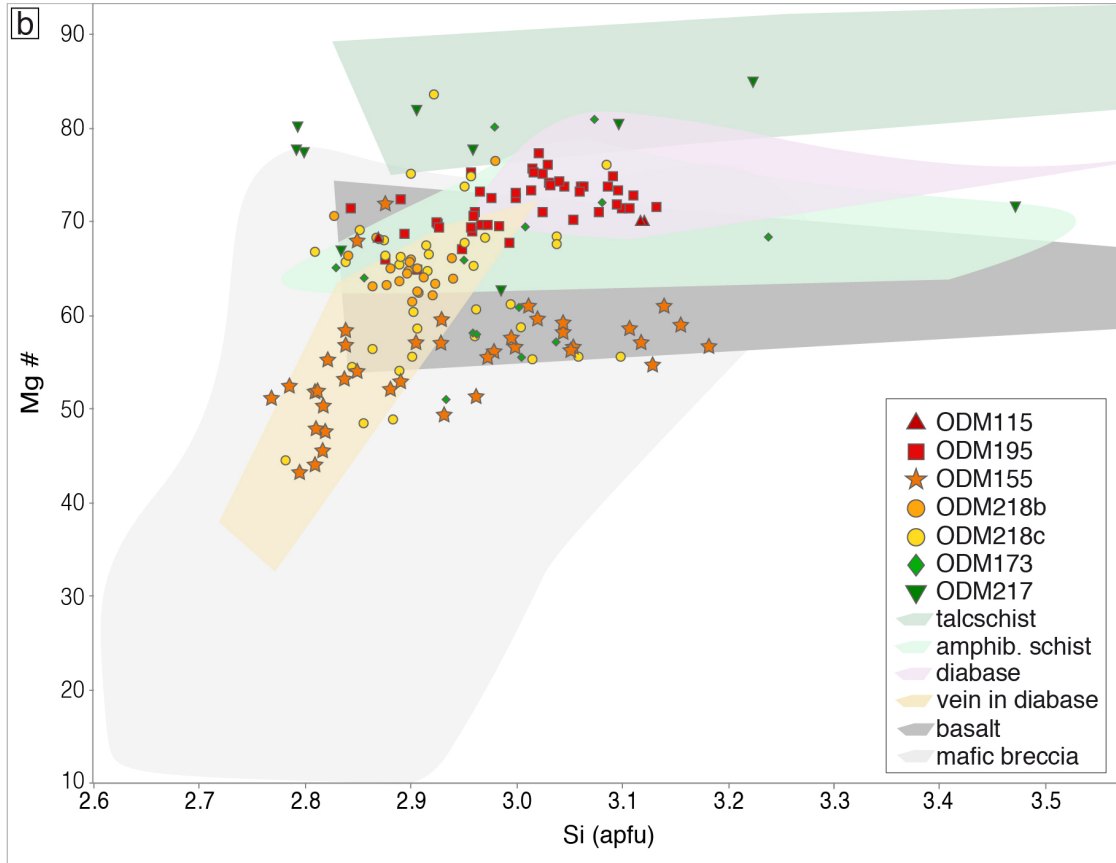
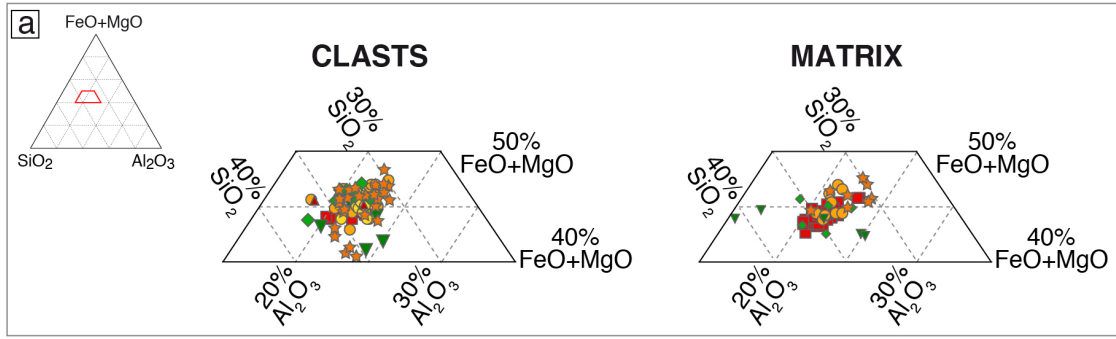
1423

1424



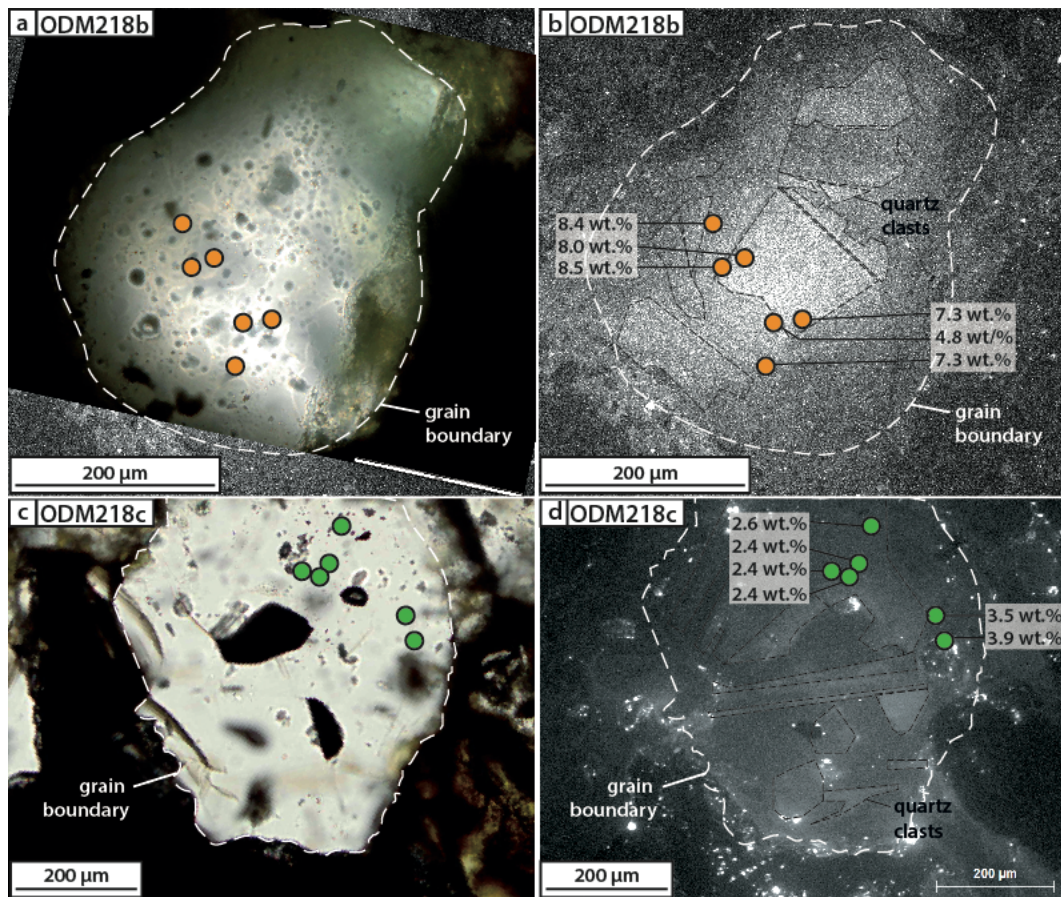
1425  
 1426 **Figure 5:** Bulk rock geochemistry. SiO<sub>2</sub> versus (a) CaO and (b) Mg# ( $=Mg/(Mg+Fe)*100$ );  
 1427 brecciated rocks show a relative decrease in both CaO and Mg# with increasing degree of  
 1428 silicification; mixed mafic-ultramafic breccias (green symbols) tend to be higher in magnesium at  
 1429 a given silica content; grey arrows: trend of passive depletion of CaO in breccias due to silica  
 1430 addition; Mg# will not be affected by silica addition. (c) Cr vs Ni; mixed breccias tend to be  
 1431 enriched in nickel and chromium compared with purely mafic breccias. Data for basalts and  
 1432 diabases from the 13°20'N OCC (Wilson et al., 2013) and for peridotites from the 15°20'N Fracture  
 1433 Zone (Godard et al., 2008; Paulick et al., 2006) are shown for comparison. Data are available in  
 1434 Table 2.





1436 **Figure 6:** Chlorite composition in clasts and matrices (a) in a FeO+MgO, Al<sub>2</sub>O<sub>3</sub>, SiO<sub>2</sub> ternary  
 1437 diagram; (b) Mg# versus Si (atoms per formula unit); chlorite compositions are compared to  
 1438 other oceanic chlorites from ultramafic rocks (talcschists from 15°45'N: Escartín et al., 2003, and  
 1439 south of Atlantis Massif: Boschi et al., 2006); mixed mafic-ultramafic amphibolite schists  
 1440 (Escartín et al., 2003); mafic rocks (diabases: Escartín et al., 2003; basalts from MAR: Humphris  
 1441 & Thompson, 1978, and from MARK: Gillis and Thompson, 1993); altered mafic rocks  
 1442 (silicified breccias from MARK: Delaney et al., 1987; Saccocia and Gillis, 1995; chlorite-quartz  
 1443 vein in diabase, Atlantis Massif: Castelain et al., 2014); (c) Si versus R<sup>2+</sup> diagram with chlorite  
 1444 endmembers; (d) Histogram of chlorite crystallization temperatures estimated using the semi-  
 1445 empirical geothermometer of Bourdelle et al. (2013). Chlorite analyses and calculated  
 1446 temperatures are available in Tables S2 and S4.

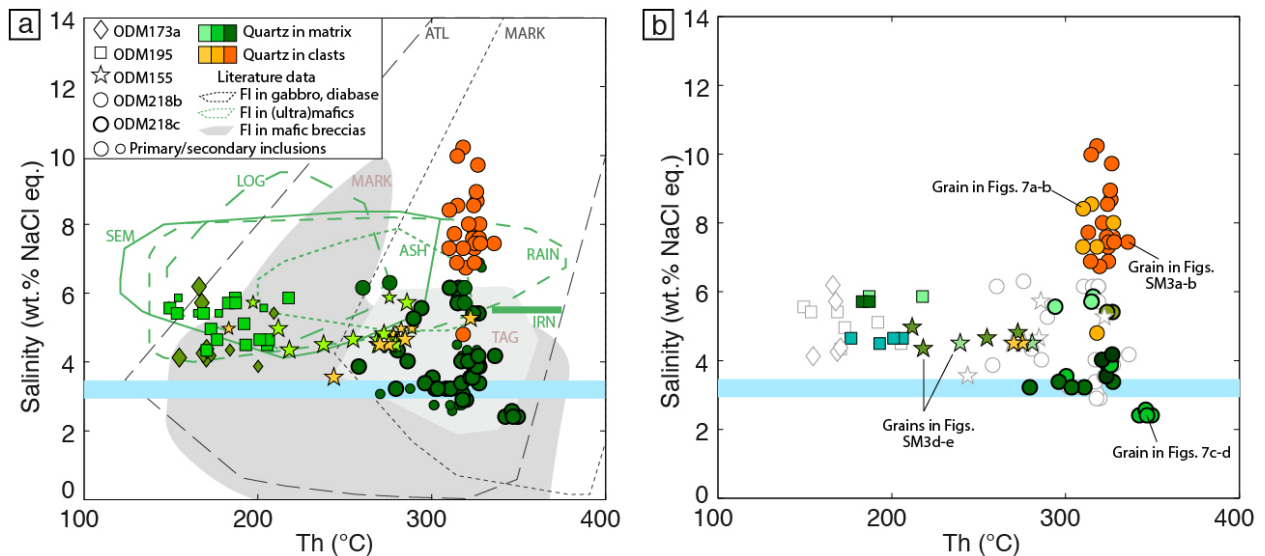
1447



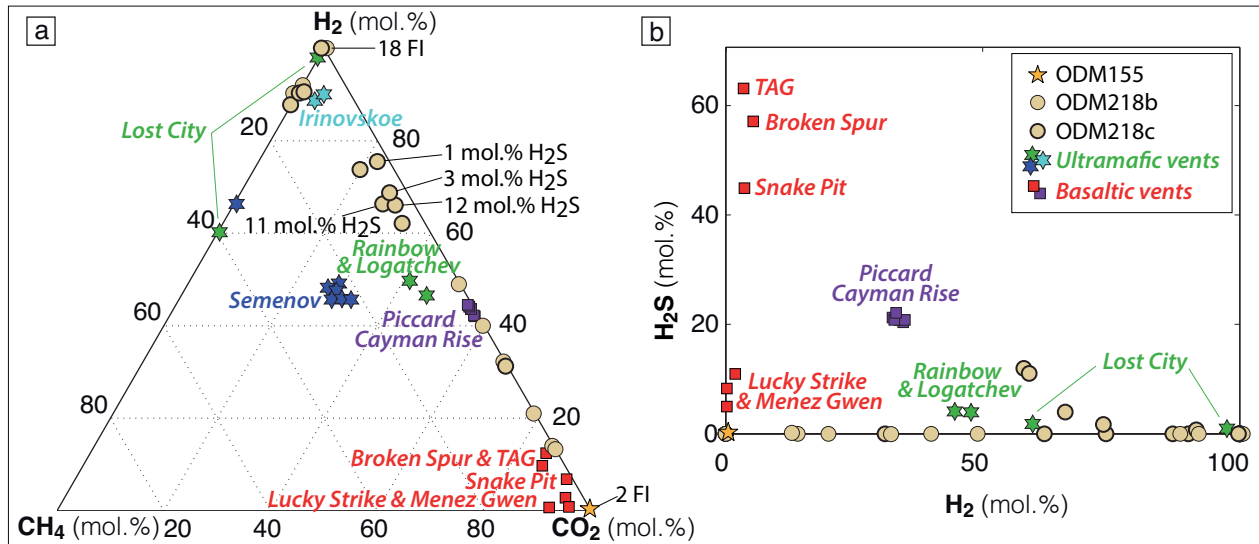
1448 **Figure 7:** Distribution of measured fluid inclusions in quartz grains from ODM218b (a and b,  
 1449 orange dots) and ODM218c (c and d, green dots). Microphotographs under parallel nicols showing  
 1450

1451 individual quartz crystals in ODM218b (a) and in ODM218c (c). SEM-cathodoluminescence image  
 1452 of the same quartz grains in ODM218b (b) and in ODM218c (d); grain boundary shown by the  
 1453 white dashed line; luminescence variations illustrate that quartz grains are composed of multiple  
 1454 former quartz angular clasts (black dotted lines) around which quartz recrystallized in successive  
 1455 generations. Quartz crystallization was obviously syntectonic, with successive steps of quartz  
 1456 growth-hydrofracturing-overgrowth. The large salinity (indicated in wt.% NaCl equivalent)  
 1457 variation for fluid inclusions at the quartz grain scale suggests that fluids with different salinities  
 1458 were circulating (and thus trapped) during the successive episodes of quartz growth. Note that the  
 1459 position of fluid inclusions was projected on the grain surface, while inclusions are in fact  
 1460 distributed at various depths in the quartz grain.

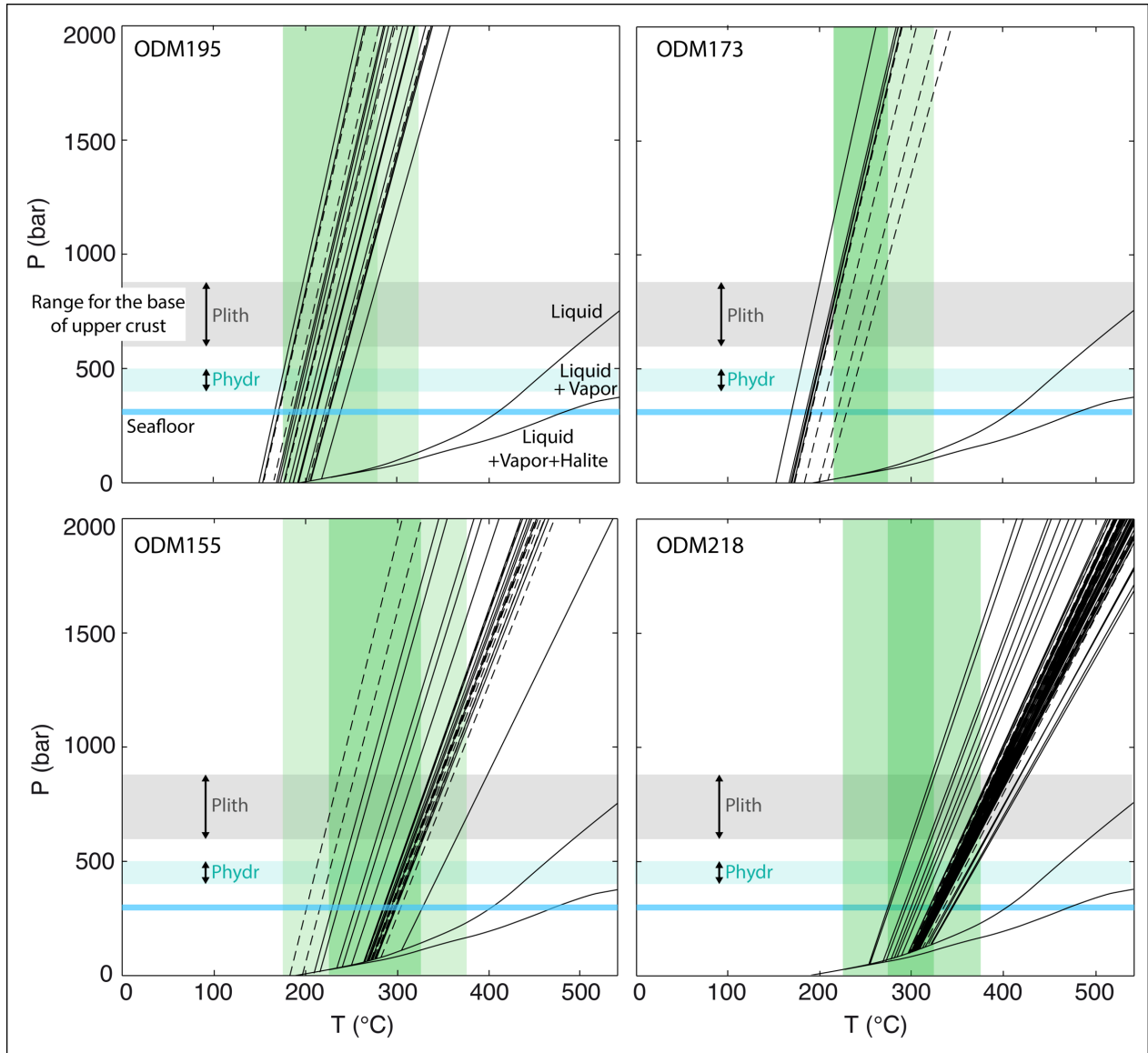
1461



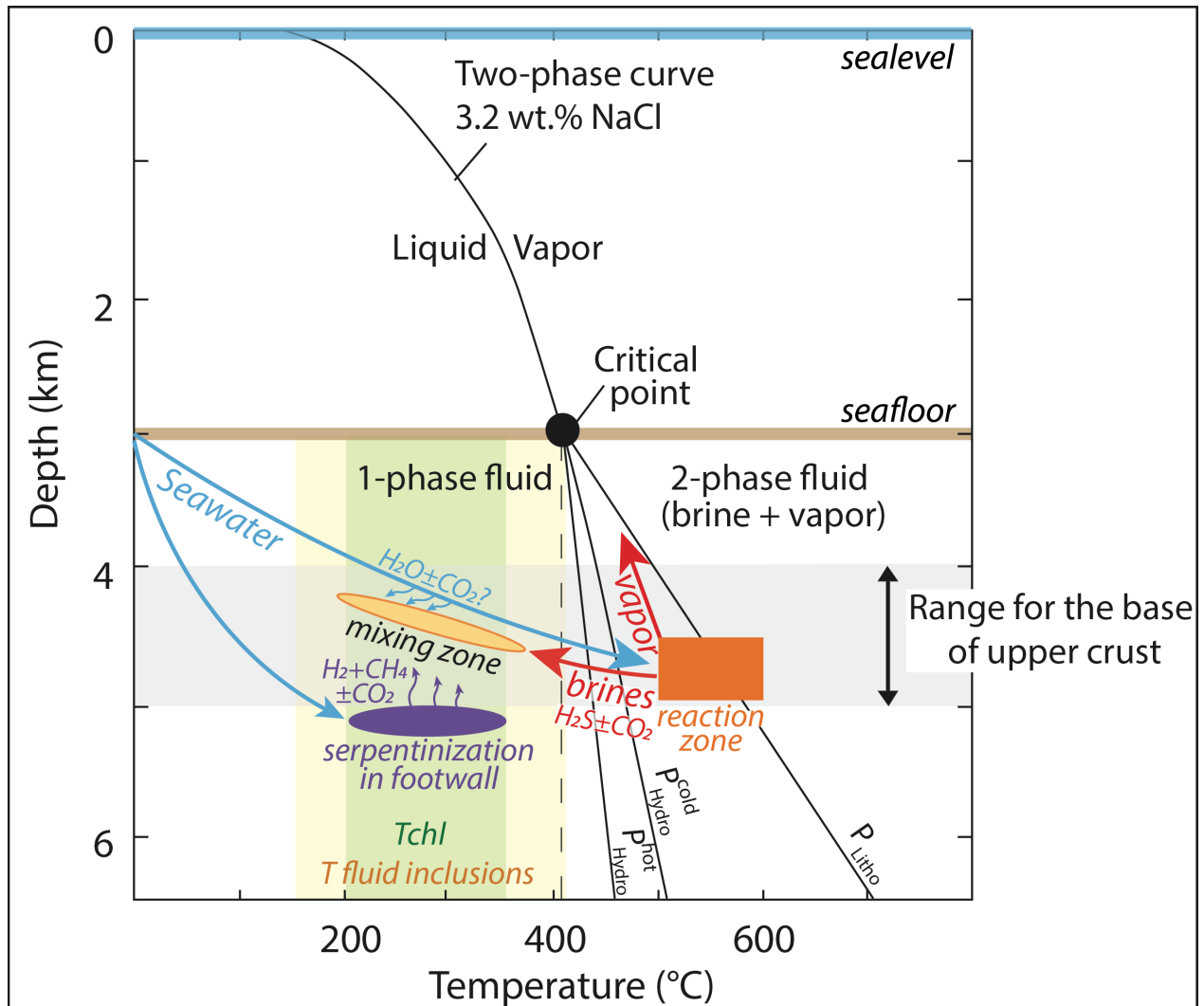
1462  
 1463 **Figure 8:** Homogenization temperatures (Th) against salinity for (a) all primary and secondary  
 1464 fluid inclusions; data are compared to Th and salinity ranges measured in fluid inclusions from  
 1465 oceanic gabbros (MARK: Kelley and Delaney, 1987), diabases (Atlantis Massif: Castelain et al.,  
 1466 2014), mafic silicified breccias from MARK (Delaney et al., 1987; Saccocia and Gillis, 1995) and  
 1467 TAG (Petersen et al., 1998), detachment plane (ultra)mafic rocks hosting hydrothermal vents  
 1468 (Rainbow, Logatchev, Ashadze, Semenov, Irinovskoe; Bortnikov et al., 2011, 2014, 2015;  
 1469 Simonov et al., 2015); (b) Heterogeneity of inclusion Th and salinity at the sample scale for the  
 1470 primary inclusions only, for clarity issues, using a similar color and symbol for inclusions in each  
 1471 grain. Seawater salinity is indicated with a blue line.



1472  
 1473 **Figure 9:** Molar proportion of gases (other than H<sub>2</sub>O) analyzed by Raman spectroscopy in the  
 1474 vapor phase of two-phase fluid inclusions for the two highly silicified mafic breccias ODM155 and  
 1475 ODM218. All fluid inclusions are dominantly aqueous, and H<sub>2</sub>O vapor is the dominant gas phase.  
 1476 (a) Relative molar proportions of CH<sub>4</sub>, CO<sub>2</sub> and H<sub>2</sub> in the gas phase. Gases other than H<sub>2</sub>O were  
 1477 analyzed in only 2 inclusions (over 17 analyzed) for ODM155 (and contain only CO<sub>2</sub> other than  
 1478 H<sub>2</sub>O vapor), in 15 inclusions over 28 analyzed for ODM218b, and in the 21 fluid inclusions  
 1479 analyzed in ODM218c. 7 and 11 fluid inclusions contain only H<sub>2</sub> (other than H<sub>2</sub>O vapor) in  
 1480 ODM218b and ODM218c, respectively. (b) H<sub>2</sub> versus H<sub>2</sub>S content in fluid inclusions (expressed  
 1481 as a mol.% of CH<sub>4</sub>-CO<sub>2</sub>-H<sub>2</sub>-H<sub>2</sub>S in the vapor phase). Fluid inclusion gas compositions are  
 1482 compared to data from basaltic- (Menez Gwen, Broken Spur, TAG, Snake Pit, Lucky Strike) and  
 1483 ultramafic- (Rainbow, Logatchev, Lost City) derived hydrothermal vents (Fouquet et al., 2010).  
 1484 Data from Semenov and Irinovskoe ultramafic-derived vents (Destrigneville et al., 2015) and from  
 1485 Piccard mafic-derived vents on Cayman Rise (McDermott et al., 2018) are also plotted for  
 1486 comparison.  
 1487



1488  
 1489 **Figure 10:** Range of P-T conditions for silicification of brecciated rocks within the detachment  
 1490 plane. P-T isochoric relationships for fluid inclusions, calculated from microthermometric data  
 1491 (equation of Zhang & Frantz, 1987), are plotted in black plain and dashed lines for primary and  
 1492 secondary fluid inclusions respectively. The liquid-vapor and liquid-vapor-halite curves are from  
 1493 Sourirajan and Kennedy (1962). Pressure at the seafloor is indicated with a blue line, and the range  
 1494 of lithostatic and hydrostatic fluid pressures at the base of the hangingwall upper crust (1–2 km  
 1495 thick) is in grey and blue respectively (assuming seawater and rock densities of 1025 and 3000  
 1496 kg/m<sup>3</sup> respectively). The temperature range of chlorite crystallization during silicification,  
 1497 calculated from chlorite composition (geothermometer of Bourdelle et al., 2013), is in green (darker  
 1498 green for higher number of chlorites; see Figure 6d).

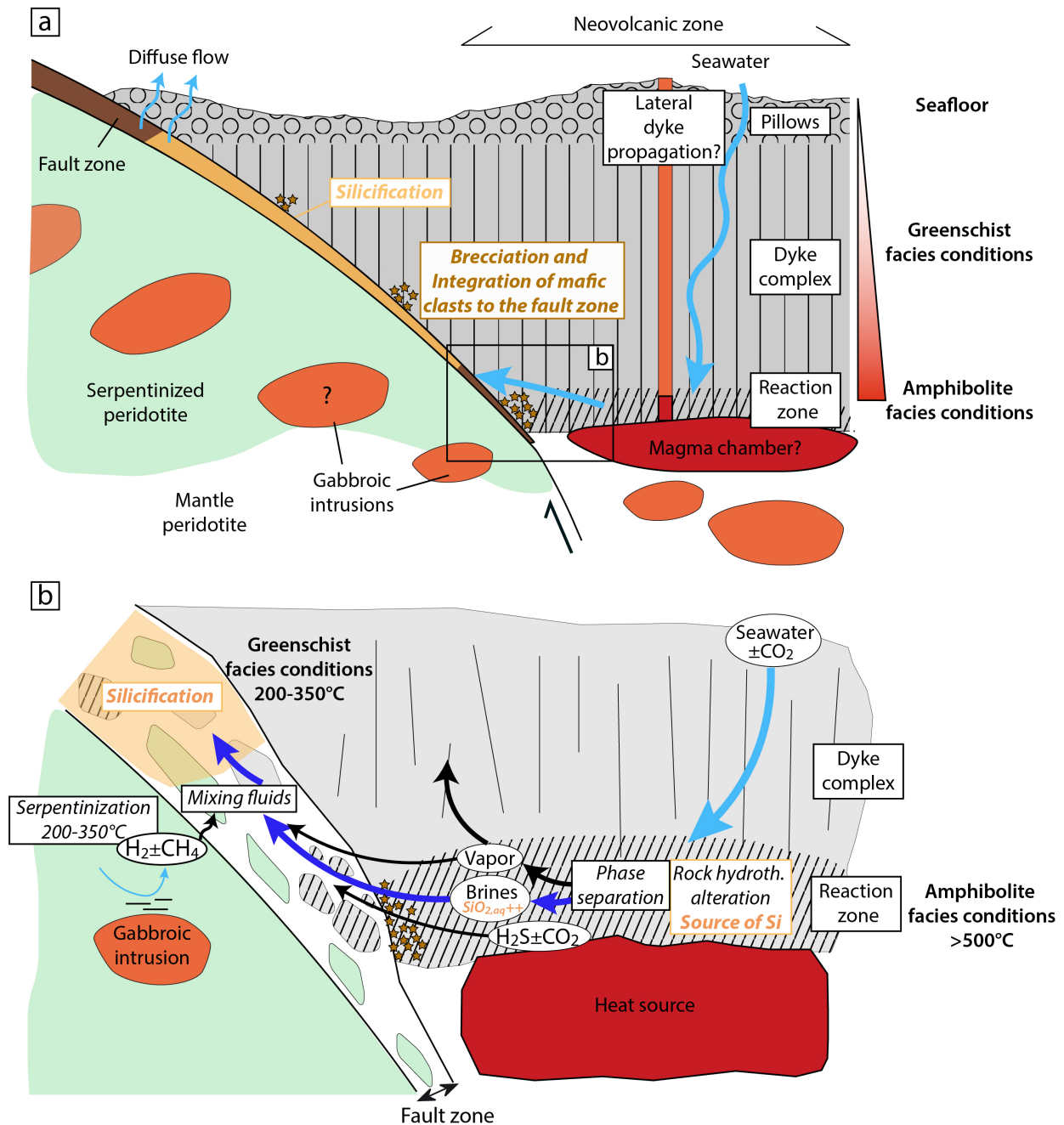


1499  
 1500 **Figure 11:** P-T-depth relationships in the NaCl-H<sub>2</sub>O system for a hydrothermal seawater-like  
 1501 solution (3.2 wt.% NaCl). The two-phase curve separates the one-phase liquid field from the two-  
 1502 phase liquid+vapor field (Sourirajan & Kennedy, 1962). Temperature-depth relationship for the  
 1503 two-phase curve beyond the critical point (407°C, 298 bars, black dot) is calculated for both  
 1504 lithostatic and hydrostatic fluid pressures. Cold and hot hydrostatic pressure gradients (100 and 50  
 1505 bar/km respectively) were taken from Coumou et al. (2009) and Castelain et al. (2014). Seawater  
 1506 (blue arrow) infiltrating the hangingwall crust (1-2 km thick) may undergo phase separation, at  
 1507 least when reaching the reaction zone (orange rectangle) at the base of the crust (diabase clasts  
 1508 suggest temperature >500 °C). While part of vapor phases can migrate upwards into the crust,  
 1509 higher density brines are likely released in the detachment plane upon diabase brecciation (red  
 1510 arrows). They are mixed in variable amounts with fluids derived from footwall serpentinization

1511 (purple arrows) and potentially small amounts of seawater circulating in hangingwall basalts (blue  
 1512 arrows). Temperature ranges of chlorite formation (light green zone) and homogenization of fluid  
 1513 inclusions (light yellow zone) are reported (see Figures 6d, 8, 10 and text for details).

1514

1515



1516

1517 **Figure 12:** Schematic interpretation of fluid circulation along the 13°20'N OCC. (a) The  
 1518 hangingwall corresponds to a section of upper crust while the footwall progressively exhumed

1519 material from deeper levels of the lithosphere (mantle-derived peridotites with gabbroic intrusions).  
1520 A reaction zone at the base of the upper crust is generated by a heat source located beneath the  
1521 neovolcanic zone. The fault zone thickens during exhumation, due to the integration of hangingwall  
1522 material. (b) Close up of the reaction zone close to the heat source. Seawater percolates down to  
1523 the reaction zone where increased pressure and temperature generate phase separation into brine  
1524 and vapor phases. Brines are enriched in silica released by hydrothermal alteration of the mafic  
1525 rocks. While most of the vapor phases escape towards the surface, brines (and a small portion of  
1526 vapor phases) are integrated into the fault zone during the overplating and mix with (small amounts  
1527 of) hydrogen-bearing fluids generated by serpentinization of the footwall. Reaction of hydrogen  
1528 with CO<sub>2</sub> either dissolved in seawater or released by magmatic activity results in the formation of  
1529 methane. As the fluid ascends and cools down, the solubility of silica strongly decreases resulting  
1530 in precipitation of quartz that entraps the fluid inclusions.

1531



1532

1533

*Geochemistry, Geophysics, Geosystems*

1534

Supporting Information for

1535

**Fluid circulation along an oceanic detachment fault: insights from fluid**

1536

**inclusions in silicified brecciated fault rocks (Mid-Atlantic Ridge at 13°20'N)**

1537

A. Verlaquet<sup>1\*</sup>, D. Bonnemains<sup>2</sup>, C. Mével<sup>2</sup>, J. Escartín<sup>2,3</sup>, M. Andreani<sup>4</sup>, F.

1538

Bourdelle<sup>5</sup>, M-C. Boiron<sup>6</sup>, V. Chavagnac<sup>7</sup>

1539

<sup>1</sup> Sorbonne Université, CNRS-INSU, Institut des Sciences de la Terre, IStEP UMR 7193, F 75005 Paris,

1540

France

1541

<sup>2</sup> Université de Paris, Institut de Physique du Globe, CNRS, F-75005 Paris, France

1542

<sup>3</sup> Laboratoire de Géologie (CNRS UMR 8538), Département de Géosciences, Ecole Normale Supérieure,

1543

PSL University, F-75005 Paris, France

1544

<sup>4</sup> Laboratoire de Géologie LGL-TPE, Université de Lyon, UCBL, ENSL, CNRS, Villeurbanne, 69622, France

1545

<sup>5</sup> Univ. Lille, IMT Lille Douai, Univ. Artois, Yncrea Hauts-de-France, ULR 4515 - LGCgE,

1546

Laboratoire de Génie Civil et géo-Environnement, F-59000 Lille, France

1547

<sup>6</sup> Université de Lorraine, CNRS, GeoRessources, F-54000 Nancy, France

1548

<sup>7</sup> Géosciences Environnement Toulouse (GET), Université Paul Sabatier Toulouse 3, CNRS UMR 5563, IRD,

1549

Toulouse, France

1550

\* Corresponding author: [anne.verlaquet@sorbonne-universite.fr](mailto:anne.verlaquet@sorbonne-universite.fr)

1551

1552

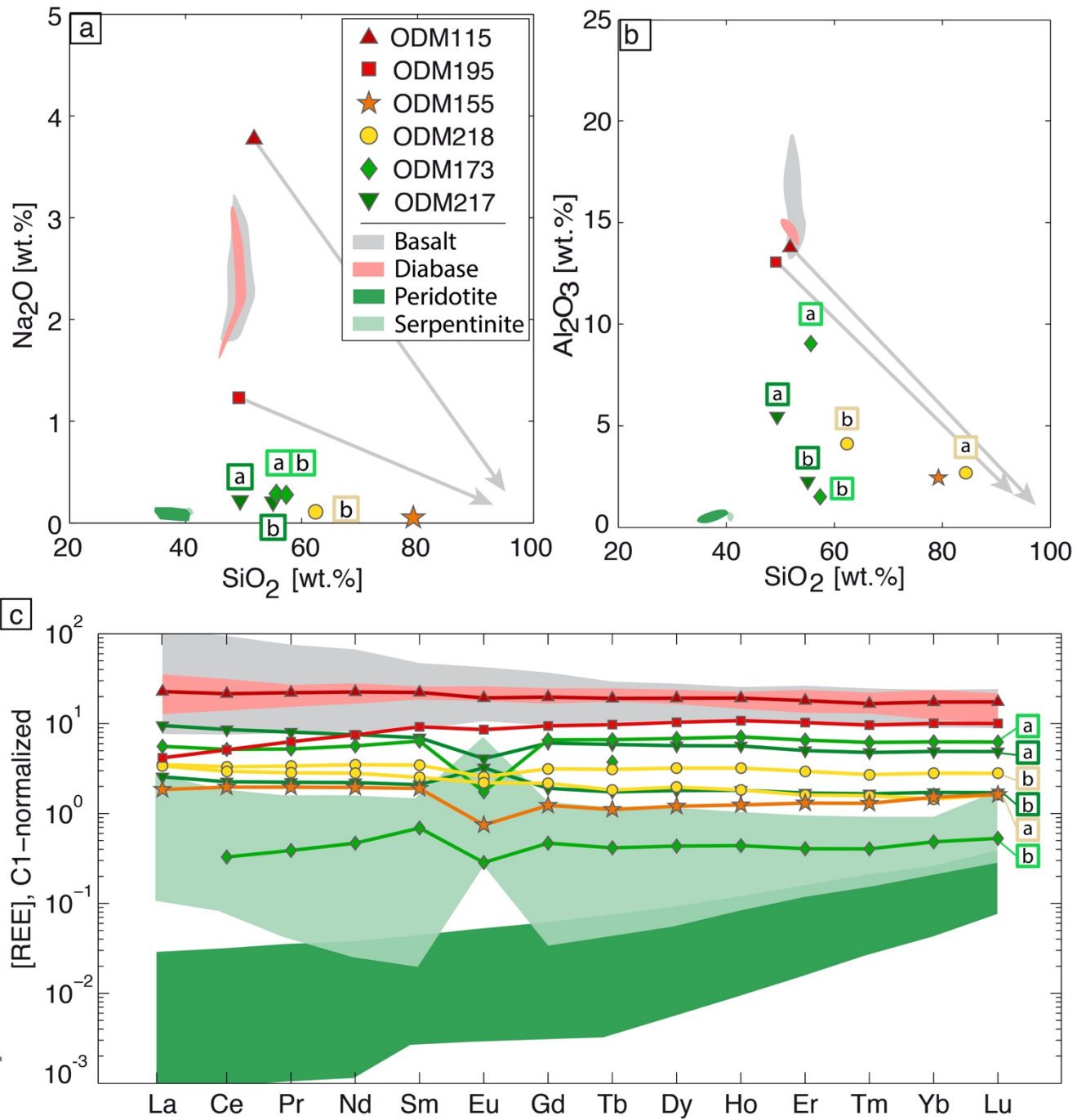
1553 **Contents of this file**

1554

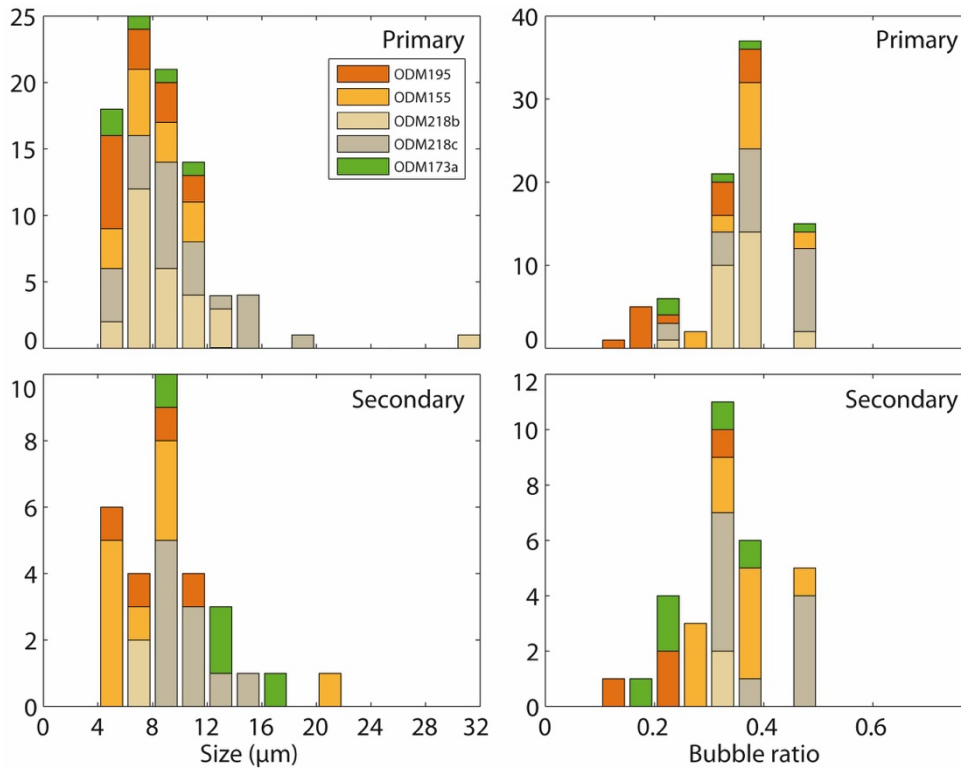
Figures S1 to S5

1555

Tables S1 to S4



1556  
 1557  
 1558 **Figure S1:** Bulk rock geochemistry. SiO<sub>2</sub> versus (a) Na<sub>2</sub>O and (b) Al<sub>2</sub>O<sub>3</sub>; brecciated rocks show a  
 1559 relative decrease in both Na<sub>2</sub>O and Al<sub>2</sub>O<sub>3</sub> with increasing degree of silicification; grey arrows:  
 1560 trend of passive depletion of Na<sub>2</sub>O and Al<sub>2</sub>O<sub>3</sub> in breccias due to silica addition. (c) Rare earth  
 1561 element (REE) content of brecciated rocks normalized to chondrite. Compositions are compared  
 1562 to data for basalts and diabases from the 13°20'N OCC (Wilson et al., 2013) and for peridotites  
 1563 from the 15°20'N Fracture Zone (Godard et al., 2008; Paulick et al., 2006).



1564

1565

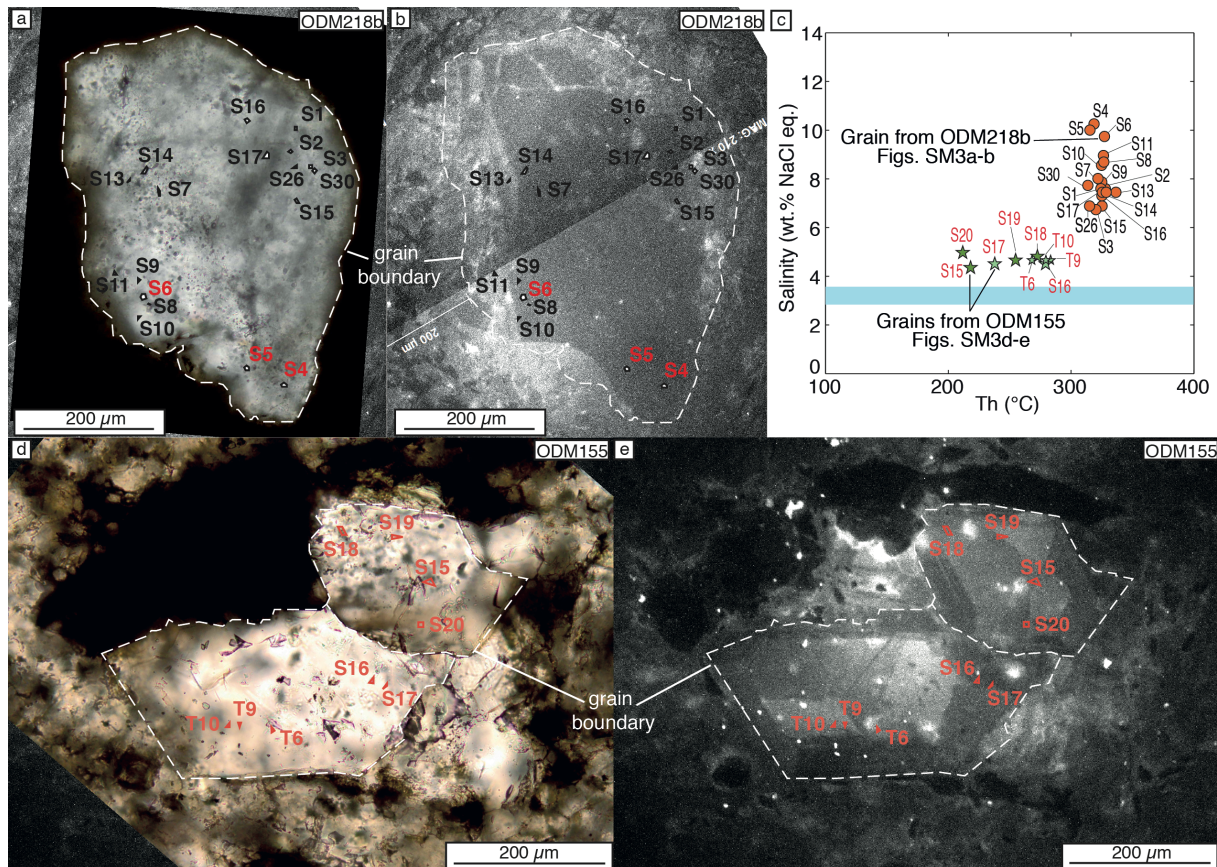
1566 **Figure S2:** Size distribution (left) and bubble/inclusion volumetric ratio (right) histograms for primary (top)  
 1567 and secondary (bottom) fluid inclusions. Vertical axis is frequency.

1568

1569

1570

1571



1572

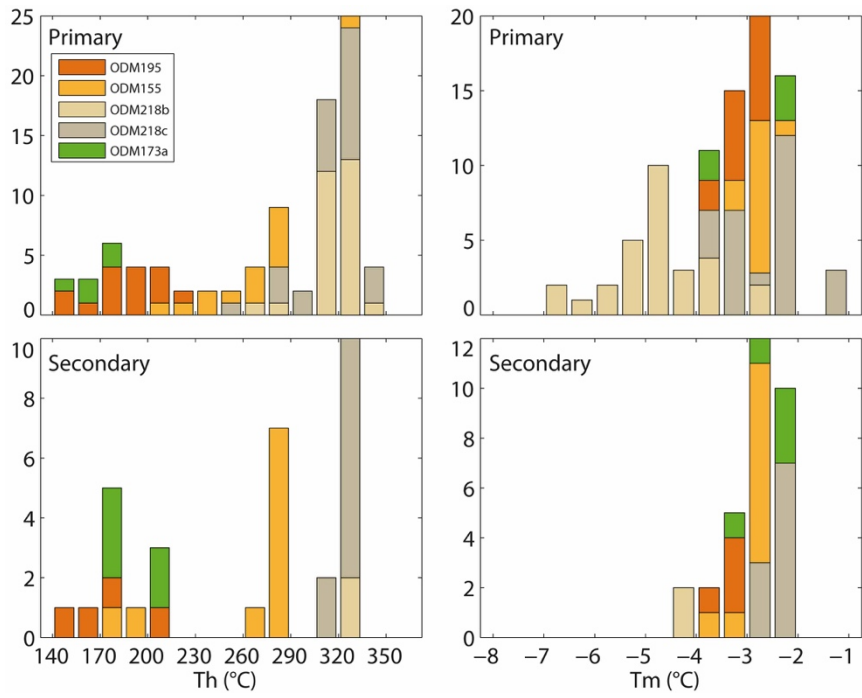
1573

1574 **Figure S3:** Location of analyzed fluid inclusions in quartz grains from ODM218b (a and b, orange dots in c)  
 1575 and ODM155 (d and e, green stars in c). Microphotographs under parallel nicols showing individual quartz  
 1576 crystals in ODM218b (a) and in ODM155 (d). SEM-cathodoluminescence images of the same quartz grains  
 1577 in ODM218b (b) and in ODM155 (e); grain boundaries are shown by the white dashed line; luminescence  
 1578 variations illustrate that quartz grains are composed of multiple former quartz angular clasts around which  
 1579 quartz recrystallized in successive generations. Quartz crystallization was unequivocally syntectonic, with  
 1580 successive steps of quartz growth-hydrofracturing-overgrowth. (c) Homogenization temperatures (Th)  
 1581 against salinity (indicated in wt.% NaCl equivalent) for primary (big symbols) and secondary (small symbols)  
 1582 fluid inclusions from quartz grains in ODM218b (a, b) and ODM155 (d, e). Seawater salinity is indicated  
 1583 with a blue line. The large salinity variation measured from fluid inclusions within individual grains  
 1584 indicates entrapment of fluids with varying salinities during successive quartz growth episodes. Note that  
 1585 the position of fluid inclusions was projected on the grain surface, while inclusions are in fact distributed  
 1586 at various depths within the quartz grain. In ODM218b (a, b) inclusions in red are those very close to the  
 1587 thick section surface.

1588

1589

1590



1591

1592

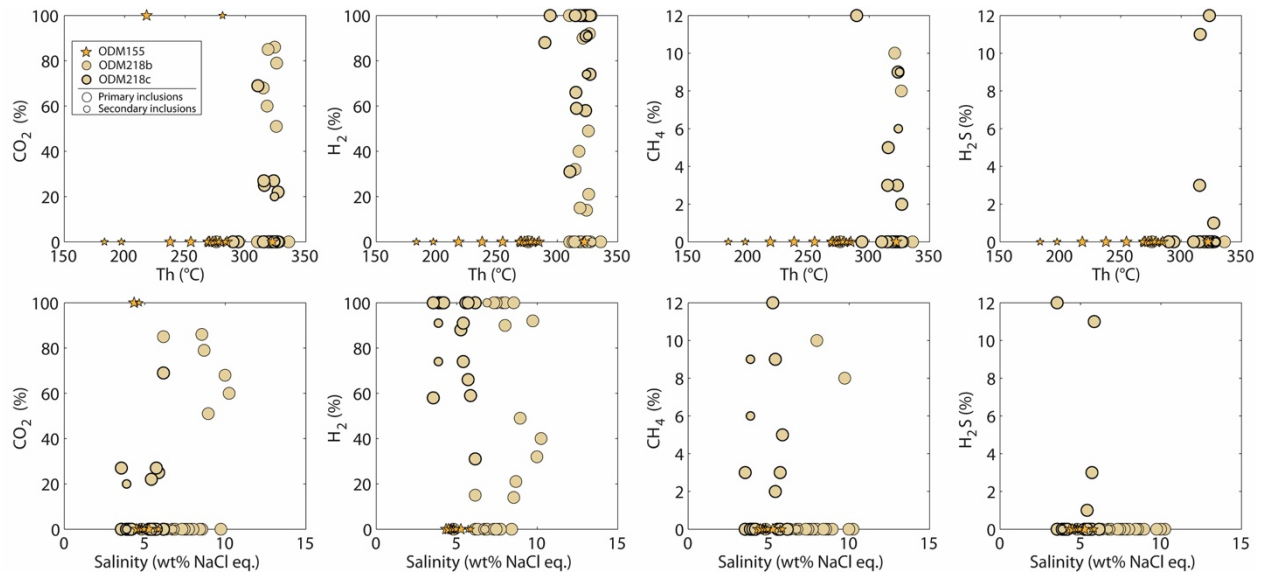
1593 **Figure S4:** Histogram showing the distribution of homogenization temperatures (Th, left) and ice melting  
1594 temperatures ( $T_{m_{ice}}$ , right) for primary (top) and secondary (bottom) fluid inclusions. Vertical axis is  
1595 frequency.

1596

1597

1598

1599



1600

1601 **Figure S5:** Gas content (mol.% of gas other than H<sub>2</sub>O in the gas bubble) versus homogenization  
 1602 temperature (Th) and salinity.

1603 **Table S1. Full chemical analyses of the selected samples.**

1604

Nature Degree of silicification Sample	Basaltic clast Qz free ODM115	Mafic Moderately Si ODM195	Mafic Highly Si ODM218a	Mafic Highly Si ODM218b	Mafic Highly Si ODM218 wr	Mafic Highly Si ODM155	Mixed Qz free ODM217a	Mixed Qz free ODM217b	Mixed Qz free ODM217 wr	Mixed Moderately Si ODM173a	Mixed Moderately Si ODM173b	Mixed Moderately Si ODM173 wr
<b>SiO<sub>2</sub></b> wt.%	51.81	49.16	84.35	62.40	65.72	79.27	49.41	55.08	48.90	55.64	57.37	68.25
<b>Al<sub>2</sub>O<sub>3</sub></b> wt.%	13.76	13.05	2.69	4.12	3.78	2.43	5.46	2.26	5.25	9.05	1.50	5.18
<b>Fe<sub>2</sub>O<sub>3</sub></b> wt.%	8.16	10.76	6.30	19.97	17.09	9.47	11.25	8.07	12.50	13.79	10.04	11.07
<b>MnO</b> wt.%	0.16	0.22	0.06	0.08	0.08	0.06	0.33	0.39	0.45	0.11	0.07	0.07
<b>MgO</b> wt.%	6.08	11.88	2.43	4.33	4.08	2.10	22.70	22.93	21.30	11.24	20.49	8.18
<b>CaO</b> wt.%	11.27	4.57	0.28	0.48	0.30	0.28	4.32	6.72	5.33	0.24	0.09	0.17
<b>Na<sub>2</sub>O</b> wt.%	3.78	1.23	< D.L.	0.11	0.07	0.05	0.22	0.20	0.24	0.29	0.28	0.17
<b>K<sub>2</sub>O</b> wt.%	0.09	0.04	< D.L.	< D.L.	< D.L.	0.02	0.03	0.03	0.04	0.04	0.03	0.03
<b>TiO<sub>2</sub></b> wt.%	1.37	0.65	0.17	0.27	0.26	0.15	0.42	0.12	0.40	0.49	< D.L.	0.26
<b>P<sub>2</sub>O<sub>5</sub></b> wt.%	0.16	< D.L.	< D.L.	< D.L.	< D.L.	< D.L.	0.06	< D.L.	0.05	0.05	< D.L.	0.04
<b>PF</b> wt.%	3.03	7.22	3.44	7.72	7.77	6.67	6.39	4.86	6.52	9.18	10.28	6.24
<b>Total</b> wt.%	99.65	98.79	99.71	99.48	99.14	100.49	100.60	100.67	100.97	100.11	100.15	99.66
<b>Mg #</b>	59.61	68.62	43.26	30.05	32.11	30.51	80.00	84.91	77.15	61.74	80.18	59.41
<b>FeO</b> wt.%	4.74	5.54	5.50	14.46	12.49	3.51	8.01	5.61	8.85	7.45	5.75	6.14
<b>H<sub>2</sub>O total</b> wt.%	3.22	8.13	2.49	4.20	4.32	2.62	7.05	5.55	6.95	8.93	< D.L.	5.32
<b>S total</b> wt.%	0.04	0.04	1.04	7.68	6.21	4.75	0.02	0.03	0.02	0.66	0.69	1.98
<b>B</b> ppm	5	2	2	<2	<2	4	11	8	14	8	10	7
<b>Cl</b> ppm	230	800	240	355	295	235	435	380	580	1520	2540	1030
<b>Li</b> ppm	3.7	7.6	5.4	3.0	3.3	8.3	7.4	7.6	7.4	4.3	4.2	3.1
<b>As</b> ppm	2.29	< D.L.	< D.L.	< D.L.	< D.L.	1.80	1.88	1.75	3.25	1.68	< D.L.	< D.L.
<b>Ba</b> ppm	35.37	4.17	3.00	1.67	< D.L.	2.66	< D.L.	1.69	< D.L.	1.90	< D.L.	6.75
<b>Be</b> ppm	0.64	< D.L.	< D.L.	< D.L.	< D.L.	< D.L.	0.46	0.60	0.50	< D.L.	< D.L.	< D.L.
<b>Bi</b> ppm	0.19	< D.L.	0.21	0.69	1.30	0.32	< D.L.	< D.L.	0.10	0.12	0.52	0.20
<b>Cd</b> ppm	0.14	< D.L.	< D.L.	< D.L.	0.12	< D.L.	< D.L.	< D.L.	< D.L.	0.68	203.80	12.18
<b>Ce</b> ppm	13.19	3.13	1.81	2.03	1.98	1.20	5.26	1.38	3.77	3.17	0.20	1.35
<b>Co</b> ppm	30.87	31.10	36.76	206.20	151.30	82.21	71.51	61.76	71.78	49.51	280.50	60.67
<b>Cr</b> ppm	308.50	349.30	293.70	590.40	525.60	303.30	1826.00	1895.00	2070.00	934.30	3319.00	1214.00
<b>Cs</b> ppm	< D.L.	< D.L.	< D.L.	< D.L.	< D.L.	< D.L.	< D.L.	< D.L.	< D.L.	< D.L.	< D.L.	< D.L.
<b>Cu</b> ppm	66.84	11.68	87.36	564.10	697.30	19.05	874.20	450.80	1540.00	504.20	1609.00	605.20
<b>Dy</b> ppm	4.72	2.55	0.48	0.79	0.75	0.30	1.40	0.44	1.38	1.68	0.11	0.92
<b>Er</b> ppm	2.89	1.65	0.26	0.47	0.45	0.21	0.80	0.27	0.81	1.05	0.07	0.59
<b>Eu</b> ppm	1.09	0.48	0.12	0.14	0.13	0.04	0.23	0.18	0.19	0.10	0.02	0.05
<b>Ga</b> ppm	13.96	11.95	3.46	5.99	5.77	3.93	8.09	4.23	8.36	11.42	5.84	7.08
<b>Gd</b> ppm	3.93	1.88	0.43	0.63	0.60	0.25	1.21	0.38	1.12	1.32	0.09	0.75
<b>Ge</b> ppm	1.85	0.75	0.50	0.43	0.40	0.28	1.57	1.64	1.95	0.61	5.09	0.74
<b>Hf</b> ppm	2.45	0.97	0.27	0.48	0.45	0.28	0.75	0.22	0.68	0.75	< D.L.	0.39
<b>Ho</b> ppm	1.05	0.59	0.10	0.18	0.16	0.07	0.31	0.10	0.30	0.39	0.02	0.22
<b>In</b> ppm	< D.L.	< D.L.	< D.L.	< D.L.	< D.L.	< D.L.	0.11	< D.L.	0.18	< D.L.	< D.L.	< D.L.
<b>La</b> ppm	5.40	0.99	0.80	0.83	0.83	0.44	2.26	0.61	1.55	1.33	< D.L.	0.55
<b>Lu</b> ppm	0.43	0.25	0.04	0.07	0.07	0.04	0.12	0.04	0.12	0.15	0.01	0.09
<b>Mo</b> ppm	< D.L.	< D.L.	5.58	12.11	8.58	1.43	< D.L.	< D.L.	< D.L.	1.39	184.30	14.06

<b>Nb</b>	ppm	6.84	0.57	1.08	1.46	1.47	0.89	3.90	0.88	2.96	2.07	< D.L.	1.16
<b>Nd</b>	ppm	10.30	3.43	1.28	1.60	1.52	0.89	3.45	1.01	2.69	2.59	0.21	1.20
<b>Ni</b>	ppm	112.80	126.40	140.40	492.70	385.90	190.70	1080.00	1180.00	1064.00	429.50	1609.00	710.70
<b>Pb</b>	ppm	0.90	< D.L.	< D.L.	1.23	1.17	1.08	< D.L.	< D.L.	< D.L.	< D.L.	2.24	1.22
<b>Pr</b>	ppm	2.05	0.58	0.26	0.31	0.29	0.18	0.75	0.21	0.56	0.49	0.04	0.20
<b>Rb</b>	ppm	0.79	< D.L.	< D.L.	< D.L.	< D.L.	< D.L.	< D.L.	< D.L.	< D.L.	< D.L.	< D.L.	< D.L.
<b>Sc</b>	ppm	38.58	32.40	5.40	8.67	8.67	5.12	15.97	9.30	16.01	22.31	9.47	12.85
<b>Sb</b>	ppm	< D.L.	< D.L.	< D.L.	< D.L.	< D.L.	< D.L.	< D.L.	< D.L.	< D.L.	< D.L.	0.25	< D.L.
<b>Sm</b>	ppm	3.30	1.36	0.37	0.51	0.50	0.28	1.03	0.31	0.90	0.95	0.10	0.50
<b>Sn</b>	ppm	1.55	0.64	3.80	0.48	0.52	9.66	< D.L.	< D.L.	0.54	0.79	0.83	1.09
<b>Sr</b>	ppm	145.50	32.01	< D.L.	4.17	< D.L.	3.86	5.94	4.84	6.93	9.61	4.48	6.18
<b>Ta</b>	ppm	0.52	0.05	0.09	0.11	0.11	0.07	0.28	0.06	0.21	0.16	< D.L.	0.08
<b>Tb</b>	ppm	0.69	0.35	0.07	0.11	0.11	0.04	0.21	0.06	0.20	0.24	0.02	0.14
<b>Th</b>	ppm	0.55	< D.L.	< D.L.	0.12	0.11	0.07	0.29	0.07	0.23	0.16	< D.L.	0.08
<b>Tm</b>	ppm	0.41	0.24	0.04	0.07	0.06	0.03	0.12	0.04	0.12	0.15	0.01	0.08
<b>U</b>	ppm	0.19	< D.L.	0.07	0.07	0.06	0.05	0.13	0.07	0.15	0.14	0.45	0.14
<b>V</b>	ppm	266.50	180.50	35.06	58.83	54.12	34.71	99.12	49.06	99.92	115.90	42.02	68.29
<b>W</b>	ppm	0.32	< D.L.	0.72	< D.L.	< D.L.	0.55	0.32	< D.L.	0.41	1.28	< D.L.	1.21
<b>Y</b>	ppm	26.89	14.83	2.43	4.39	4.12	1.91	7.95	2.65	7.71	10.34	0.61	5.87
<b>Yb</b>	ppm	2.80	1.63	0.23	0.45	0.43	0.24	0.79	0.28	0.80	1.01	0.08	0.57
<b>Zn</b>	ppm	60.02	105.60	45.73	56.51	64.18	33.78	139.50	115.00	161.80	237.90	2947.00	379.70
<b>Zr</b>	ppm	84.25	29.36	10.77	17.07	16.19	10.14	27.35	7.70	24.15	24.61	< D.L.	14.00

1605 <D.L.: lower than detection limit. Qz: quartz. Highly/moderately Si: highly/moderately silicified

1606

1607

1608







Sample	155	155	155	155	155	155	155	155	155	155	155	155	155	155	155	155	155	155	155	155	155	155	155
Clast vs matrix	Clast	Clast	Clast	Clast	Clast	Clast	Clast	Clast	Clast	Clast	Clast	Clast	Clast	Clast	Clast	Clast	Clast	Clast	Clast	Clast	Clast	Clast	Clast
Analysis #	14	73 / 1	75 / 1	76 / 1	77 / 1	81 / 1	82 / 1	83 / 1	41 / 1	42 / 1	43 / 1	44 / 1	45 / 1	46 / 1	48 / 1	49 / 1	50 / 1	51 / 1	52 / 1	53 / 1	54 / 1	57 / 1	58 / 1
<b>Chlorite composition <sup>a</sup></b>																							
SiO <sub>2</sub>	28.07	31.03	30.61	30.78	30.68	29.35	27.02	29.24	27.94	28.79	26.59	26.61	25.39	28.07	29.40	29.06	28.72	27.25	29.02	28.86	29.17	27.82	26.49
TiO <sub>2</sub>	0.03	0.04	0.08	0.06	0.03	0.01	0.07	0.02	0.00	0.02	0.05	0.06	0.02	0.01	0.00	0.04	0.09	0.07	0.00	0.01	0.01	0.05	0.05
Al <sub>2</sub> O <sub>3</sub>	19.16	19.99	18.27	20.81	18.41	17.26	19.23	17.37	18.57	18.11	19.93	19.88	18.88	18.00	18.17	18.03	17.80	19.41	17.68	18.03	17.46	20.26	20.36
Cr <sub>2</sub> O <sub>3</sub>	0.03	0.08	0.01	0.00	0.06	0.00	0.10	0.02	0.11	0.21	0.08	0.04	0.00	0.08	0.26	0.40	0.44	0.04	0.31	0.43	0.30	0.12	0.00
FeO	22.98	19.31	19.62	19.95	20.75	22.31	24.31	21.62	22.64	24.05	25.12	25.55	29.02	21.98	21.13	21.07	22.37	24.60	22.35	22.81	22.68	24.06	25.08
MnO	0.27	0.35	0.31	0.53	0.33	0.32	0.39	0.24	0.23	0.41	0.24	0.29	0.17	0.52	0.56	0.52	0.38	0.39	0.33	0.35	0.21	0.21	0.32
MgO	17.21	15.68	17.35	14.91	15.33	18.53	16.82	18.95	17.08	16.84	15.17	15.82	12.40	18.19	17.25	16.60	17.12	15.04	16.17	16.74	16.60	15.22	14.27
NiO	0.09	0.09	0.07	0.15	0.12	0.11	0.00	0.09	0.14	0.08	0.00	0.01	0.03	0.09	0.01	0.17	0.08	0.05	0.07	0.17	0.06	0.00	0.02
CaO	0.09	0.18	0.22	0.23	0.30	0.22	0.06	0.09	0.07	0.10	0.07	0.07	0.07	0.10	0.11	0.11	0.09	0.05	0.27	0.13	0.18	0.08	0.11
Na <sub>2</sub> O	0.01	0.08	0.06	0.08	0.11	0.01	0.06	0.04	0.00	0.03	0.04	0.07	0.06	0.04	0.07	0.10	0.05	0.06	0.12	0.07	0.04	0.05	0.03
K <sub>2</sub> O	0.01	0.02	0.04	0.05	0.02	0.00	0.02	0.00	0.01	0.00	0.01	0.02	0.01	0.02	0.05	0.05	0.01	0.02	0.04	0.01	0.01	0.02	0.02
total	87.94	86.85	86.63	87.56	86.15	88.12	88.07	87.68	86.79	88.65	87.30	88.41	86.06	87.09	87.00	86.15	87.16	86.99	86.35	87.60	86.72	87.89	86.74
K <sub>2</sub> O+Na <sub>2</sub> O+CaO	0.10	0.28	0.32	0.36	0.43	0.23	0.14	0.12	0.08	0.14	0.12	0.15	0.14	0.17	0.22	0.26	0.15	0.13	0.43	0.21	0.23	0.15	0.16
<b>Structural formula <sup>b</sup></b>																							
Si	2.90	3.15	3.14	3.12	3.18	3.02	2.82	3.01	2.93	2.97	2.81	2.78	2.79	2.93	3.04	3.04	2.99	2.88	3.05	3.00	3.05	2.89	2.82
Ti	0.00	0.00	0.01	0.00	0.00	0.00	0.01	0.00	0.00	0.00	0.00	0.00	0.00	0.00	0.00	0.00	0.01	0.01	0.00	0.00	0.00	0.00	0.00
Al	2.34	2.40	2.21	2.48	2.25	2.09	2.37	2.11	2.29	2.20	2.48	2.45	2.45	2.21	2.22	2.22	2.19	2.42	2.19	2.21	2.15	2.48	2.55
Al <sup>IV</sup>	1.10	0.85	0.86	0.88	0.82	0.98	1.18	0.99	1.07	1.03	1.19	1.22	1.21	1.07	0.96	0.96	1.01	1.12	0.95	1.00	0.95	1.11	1.18
Al <sup>VI</sup>	1.24	1.55	1.35	1.60	1.43	1.11	1.19	1.12	1.22	1.17	1.29	1.23	1.24	1.14	1.26	1.27	1.18	1.30	1.24	1.21	1.21	1.37	1.37
Cr	0.00	0.01	0.00	0.00	0.00	0.00	0.01	0.00	0.01	0.02	0.01	0.00	0.00	0.01	0.02	0.03	0.04	0.00	0.03	0.04	0.02	0.01	0.00
Fe	1.99	1.64	1.68	1.69	1.80	1.92	2.12	1.86	1.98	2.08	2.22	2.24	2.67	1.92	1.83	1.84	1.95	2.17	1.96	1.98	1.99	2.09	2.23
Mn	0.02	0.03	0.03	0.05	0.03	0.03	0.03	0.02	0.02	0.04	0.02	0.03	0.02	0.05	0.05	0.05	0.03	0.04	0.03	0.03	0.02	0.02	0.03
Mg	2.65	2.38	2.65	2.25	2.37	2.84	2.62	2.91	2.67	2.59	2.39	2.47	2.03	2.83	2.66	2.59	2.66	2.37	2.53	2.59	2.59	2.36	2.26
Ni	0.01	0.01	0.01	0.01	0.01	0.01	0.00	0.01	0.01	0.01	0.00	0.00	0.00	0.01	0.00	0.01	0.01	0.00	0.01	0.01	0.00	0.00	0.00
Ca	0.01	0.02	0.02	0.03	0.03	0.02	0.01	0.01	0.01	0.01	0.01	0.01	0.01	0.01	0.01	0.01	0.01	0.01	0.03	0.01	0.02	0.01	0.01
Na	0.00	0.02	0.01	0.01	0.02	0.00	0.01	0.01	0.00	0.01	0.01	0.01	0.01	0.01	0.01	0.02	0.01	0.01	0.02	0.01	0.01	0.01	0.01
K	0.00	0.00	0.00	0.01	0.00	0.00	0.00	0.00	0.00	0.00	0.00	0.00	0.00	0.00	0.01	0.01	0.00	0.00	0.01	0.00	0.00	0.00	0.00
octahedral sum	5.92	5.65	5.75	5.64	5.70	5.93	5.99	5.94	5.92	5.92	5.94	5.99	5.99	5.97	5.85	5.84	5.89	5.91	5.86	5.89	5.86	5.86	5.91
vacancies	0.08	0.35	0.25	0.36	0.30	0.07	0.01	0.06	0.08	0.08	0.06	0.01	0.01	0.03	0.15	0.16	0.11	0.09	0.14	0.11	0.14	0.14	0.09
Mg# <sup>c</sup>	0.57	0.59	0.61	0.57	0.57	0.60	0.55	0.61	0.57	0.56	0.52	0.52	0.43	0.60	0.59	0.58	0.58	0.52	0.56	0.57	0.57	0.53	0.50
R <sup>2+</sup> <sup>d</sup>	4.67	4.06	4.37	4.00	4.21	4.80	4.77	4.80	4.68	4.71	4.63	4.73	4.72	4.80	4.54	4.50	4.65	4.58	4.53	4.62	4.60	4.46	4.52
<b>Calculated T (°C)</b>																							
Bourdelle et al. (2013) <sup>e</sup>	284	113	138	116	120	274	1305	278	276	272	359	863	612	399	192	185	243	262	193	231	200	223	273
T <sub>corrected</sub> (>350°C) <sup>e</sup>							492					317	444	398	334								

1618

1619

Sample	218a	218a	218a	218a	218a	218a	218a	218a	218a	218a	218a	218a	218a	218a	218a	218a	218a	218a	218a	218a	218a	218a	218a	
Clast vs matrix	Clast	Clast	Clast	Clast	Clast	Clast	Clast	Clast	Clast	Clast	Clast	Clast	Clast	Clast	Clast	Clast	Clast	Clast	Clast	Clast	Clast	Clast	Clast	Clast
Analysis #	22	29	30	13 / 1	14 / 1	18 / 1	19 / 1	20 / 1	21 / 1	23 / 1	26 / 1	27 / 1	33 / 1	39 / 1	41 / 1	43 / 1	49 / 1	56 / 1	57 / 1	58 / 1	59 / 1	60 / 1	61 / 1	
Zone analysed	C2	C6	C6	C-3	C-3	C-3	C-3	C-3	C-3	C-3	C-3	C-4	C-4	C-4	C-4	C-4	C-4	C-5	C-6	C-6	C-6	C-7	C-7	
<b>Chlorite composition <sup>a</sup></b>																								
SiO <sub>2</sub>	27.59	30.42	27.21	29.33	28.53	27.11	27.18	28.94	25.64	26.69	29.01	28.37	29.10	28.70	27.66	28.07	28.88	29.91	30.98	29.13	28.05	27.65	28.23	
TiO <sub>2</sub>	0.03	0.02	0.03	0.00	0.08	0.06	0.11	0.06	0.04	0.06	0.00	0.08	0.00	0.34	0.04	0.11	0.03	0.03	0.04	0.01	0.07	0.06	0.09	
Al <sub>2</sub> O <sub>3</sub>	19.06	19.76	19.12	17.56	17.23	19.43	18.92	18.86	19.64	19.08	19.64	19.59	17.66	18.09	18.48	18.21	17.55	17.48	15.91	18.13	19.30	19.37	19.31	
Cr <sub>2</sub> O <sub>3</sub>	0.03	0.04	0.05	0.07	0.07	0.08	0.19	0.00	0.04	0.12	0.04	0.08	0.17	0.05	0.17	0.12	0.16	0.66	0.64	0.35	0.09	0.05	0.01	
FeO	23.76	9.81	24.59	23.27	23.60	25.89	23.53	18.33	28.21	26.53	18.58	17.75	22.42	20.09	21.23	21.92	18.37	17.41	14.20	14.87	18.70	19.11	18.76	
MnO	0.42	0.25	0.47	0.58	0.45	0.51	0.59	0.73	0.37	0.50	0.21	0.18	0.44	0.57	0.35	0.54	0.30	0.01	0.06	0.11	0.23	0.07	0.20	
MgO	17.14	27.78	16.45	16.29	16.29	13.86	15.44	21.24	12.65	13.98	20.59	21.11	17.87	17.73	18.06	16.77	21.61	21.13	25.20	23.31	19.73	20.50	20.66	
NiO	0.01	0.10	0.00	0.00	0.11	0.00	0.02	0.04	0.09	0.00	0.00	0.08	0.05	0.06	0.06	0.11	0.08	0.23	0.26	0.23	0.02	0.05	0.00	
CaO	0.13	0.03	0.09	0.23	0.24	0.15	0.26	0.07	0.05	0.11	0.04	0.11	0.17	0.46	0.15	0.23	0.09	0.07	0.01	0.02	0.19	0.03	0.03	
Na <sub>2</sub> O	0.04	0.02	0.03	0.00	0.02	0.04	0.01	0.00	0.05	0.02	0.01	0.00	0.02	0.01	0.03	0.00	0.03	0.00	0.00	0.00	0.06	0.03	0.01	
K <sub>2</sub> O	0.01	0.02	0.01	0.03	0.02	0.01	0.01	0.02	0.03	0.00	0.00	0.00	0.01	0.01	0.00	0.04	0.01	0.00	0.00	0.04	0.05	0.02	0.01	
total	88.23	88.23	88.06	87.37	86.64	87.14	86.26	88.29	86.82	87.10	88.10	87.34	87.92	86.10	86.24	86.13	87.11	86.94	87.33	86.21	86.48	86.93	87.31	
K <sub>2</sub> O+Na <sub>2</sub> O+CaO	0.18	0.07	0.14	0.26	0.28	0.20	0.28	0.09	0.13	0.13	0.05	0.11	0.20	0.48	0.18	0.27	0.13	0.08	0.02	0.06	0.29	0.08	0.05	
<b>Structural formula <sup>b</sup></b>																								
Si	2.86	2.92	2.84	3.06	3.01	2.88	2.89	2.91	2.78	2.85	2.92	2.87	3.00	2.99	2.90	2.96	2.95	3.04	3.08	2.95	2.89	2.84	2.88	
Ti	0.00	0.00	0.00	0.00	0.01	0.01	0.01	0.00	0.00	0.00	0.00	0.01	0.00	0.03	0.00	0.01	0.00	0.00	0.00	0.00	0.01	0.00	0.01	
Al	2.33	2.24	2.36	2.16	2.15	2.43	2.37	2.24	2.51	2.40	2.33	2.34	2.15	2.22	2.28	2.26	2.11	2.09	1.87	2.16	2.34	2.34	2.32	
Al <sup>IV</sup>	1.14	1.08	1.16	0.94	0.99	1.12	1.11	1.09	1.22	1.15	1.08	1.13	1.00	1.01	1.10	1.04	1.05	0.96	0.92	1.05	1.11	1.16	1.12	
Al <sup>VI</sup>	1.19	1.16	1.20	1.21	1.16	1.32	1.26	1.15	1.29	1.26	1.24	1.21	1.15	1.22	1.19	1.22	1.06	1.13	0.95	1.11	1.23	1.18	1.19	
Cr	0.00	0.00	0.00	0.01	0.01	0.01	0.02	0.00	0.00	0.01	0.00	0.01	0.01	0.00	0.01	0.01	0.01	0.05	0.05	0.03	0.01	0.00	0.00	
Fe	2.06	0.79	2.15	2.03	2.09	2.30	2.09	1.54	2.56	2.37	1.56	1.50	1.94	1.75	1.86	1.93	1.57	1.48	1.18	1.26	1.61	1.64	1.60	
Mn	0.04	0.02	0.04	0.05	0.04	0.05	0.05	0.06	0.03	0.04	0.02	0.02	0.04	0.05	0.03	0.05	0.03	0.00	0.01	0.01	0.02	0.01	0.02	
Mg	2.65	3.98	2.56	2.53	2.57	2.20	2.45	3.19	2.05	2.23	3.09	3.19	2.75	2.76	2.82	2.64	3.29	3.20	3.74	3.52	3.03	3.14	3.14	
Ni	0.00	0.01	0.00	0.00	0.01	0.00	0.00	0.00	0.01	0.00	0.00	0.01	0.00	0.01	0.01	0.01	0.01	0.02	0.02	0.02	0.00	0.00	0.00	
Ca	0.01	0.00	0.01	0.03	0.03	0.02	0.03	0.01	0.01	0.01	0.00	0.01	0.02	0.05	0.02	0.03	0.01	0.01	0.00	0.00	0.02	0.00	0.00	
Na	0.01	0.00	0.01	0.00	0.00	0.01	0.00	0.00	0.01	0.00	0.00	0.00	0.00	0.00	0.01	0.00	0.01	0.00	0.00	0.00	0.01	0.01	0.00	
K	0.00	0.00	0.00	0.00	0.00	0.00	0.00	0.00	0.00	0.00	0.00	0.00	0.00	0.00	0.00	0.01	0.00	0.00	0.00	0.01	0.01	0.00	0.00	
octahedral sum	5.97	5.96	5.98	5.86	5.90	5.89	5.90	5.96	5.96	5.93	5.92	5.94	5.92	5.84	5.95	5.89	5.99	5.89	5.95	5.96	5.94	5.98	5.95	
vacancies	0.03	0.04	0.02	0.14	0.10	0.11	0.10	0.04	0.04	0.07	0.08	0.06	0.08	0.16	0.05	0.11	0.01	0.11	0.05	0.04	0.06	0.02	0.05	
Mg# <sup>c</sup>	0.56	0.83	0.54	0.56	0.55	0.49	0.54	0.67	0.44	0.48	0.66	0.68	0.59	0.61	0.60	0.58	0.68	0.68	0.76	0.74	0.65	0.66	0.66	
R <sup>2+</sup> <sup>d</sup>	4.75	4.79	4.75	4.61	4.70	4.54	4.59	4.80	4.65	4.65	4.67	4.71	4.73	4.57	4.72	4.63	4.89	4.70	4.95	4.81	4.66	4.79	4.75	
<b>Calculated T (°C)</b>																								
Bourdelle et al. (2013) <sup>e</sup>	445	362	500	194	234	247	263	388	407	313	271	336	251	203	330	233	585	211	302	330	304	630	379	
T <sub>corrected</sub> (>350°C) <sup>e</sup>	351	319	369					330	337								391					402	326	

1620

1621

Sample	218a	218a	218a	218a	218a	218a	218a	218a	218a	218a	218a	218a	218a
Clast vs matrix	Clast	Clast	Clast	Clast	Mat	Mat	Mat	Mat	Mat	Mat	Mat	Mat	Mat
Analysis #	62 / 1	63 / 1	64 / 1	65 / 1	9 / 1	10 / 1	11 / 1	44 / 1	45 / 1	46 / 1	47 / 1	50 / 1	69 / 1
<b>Chlorite composition <sup>a</sup></b>													
SiO <sub>2</sub>	28.23	29.35	27.75	28.58	28.20	30.04	28.31	27.60	28.93	28.98	28.65	30.16	29.44
TiO <sub>2</sub>	0.01	0.08	0.04	0.04	0.00	0.03	0.00	0.04	0.00	0.09	0.03	0.00	0.03
Al <sub>2</sub> O <sub>3</sub>	19.86	18.85	20.29	20.27	18.42	17.92	17.90	18.64	18.47	19.06	19.56	18.66	18.49
Cr <sub>2</sub> O <sub>3</sub>	0.00	0.01	0.02	0.11	0.27	0.67	0.08	0.11	0.03	0.04	0.26	0.17	0.03
FeO	17.36	17.43	18.52	18.22	22.93	22.55	21.15	23.60	19.10	14.22	18.97	17.54	14.29
MnO	0.16	0.17	0.15	0.21	0.38	0.40	0.36	0.43	0.25	0.28	0.26	0.26	0.11
MgO	21.71	21.00	20.83	19.95	18.08	15.79	18.24	16.47	20.11	23.98	19.42	20.42	23.76
NiO	0.02	0.07	0.16	0.06	0.10	0.04	0.16	0.04	0.25	0.10	0.11	0.02	0.28
CaO	0.00	0.11	0.03	0.06	0.05	0.28	0.10	0.15	0.00	0.07	0.11	0.06	0.06
Na <sub>2</sub> O	0.00	0.01	0.01	0.00	0.00	0.05	0.08	0.03	0.00	0.02	0.08	0.05	0.00
K <sub>2</sub> O	0.00	0.00	0.02	0.02	0.00	0.08	0.00	0.00	0.00	0.03	0.03	0.03	0.01
total	87.35	87.08	87.82	87.52	88.42	87.85	86.38	87.11	87.13	86.87	87.50	87.37	86.49
K <sub>2</sub> O+Na <sub>2</sub> O+CaO	0.00	0.11	0.05	0.09	0.05	0.40	0.18	0.18	0.00	0.12	0.23	0.13	0.07
<b>Structural formula <sup>b</sup></b>													
Si	2.85	2.97	2.81	2.89	2.91	3.10	2.96	2.90	2.96	2.90	2.92	3.04	2.96
Ti	0.00	0.01	0.00	0.00	0.00	0.00	0.00	0.00	0.00	0.01	0.00	0.00	0.00
Al	2.36	2.25	2.42	2.42	2.24	2.18	2.21	2.31	2.23	2.25	2.35	2.22	2.19
Al <sup>IV</sup>	1.15	1.03	1.19	1.11	1.09	0.90	1.04	1.10	1.04	1.10	1.08	0.96	1.04
Al <sup>VI</sup>	1.21	1.22	1.23	1.31	1.14	1.28	1.17	1.21	1.18	1.15	1.26	1.25	1.14
Cr	0.00	0.00	0.00	0.01	0.02	0.05	0.01	0.01	0.00	0.00	0.02	0.01	0.00
Fe	1.47	1.48	1.57	1.54	1.98	1.94	1.85	2.07	1.63	1.19	1.61	1.48	1.20
Mn	0.01	0.01	0.01	0.02	0.03	0.03	0.03	0.04	0.02	0.02	0.02	0.02	0.01
Mg	3.27	3.17	3.14	3.01	2.78	2.43	2.84	2.58	3.07	3.58	2.95	3.07	3.56
Ni	0.00	0.01	0.01	0.00	0.01	0.00	0.01	0.00	0.02	0.01	0.01	0.00	0.02
Ca	0.00	0.01	0.00	0.01	0.01	0.03	0.01	0.02	0.00	0.01	0.01	0.01	0.01
Na	0.00	0.00	0.00	0.00	0.00	0.01	0.02	0.01	0.00	0.00	0.02	0.01	0.00
K	0.00	0.00	0.00	0.00	0.00	0.01	0.00	0.00	0.00	0.00	0.00	0.00	0.00
octahedral sum	5.97	5.90	5.98	5.89	5.96	5.79	5.94	5.94	5.93	5.97	5.91	5.85	5.94
vacancies	0.03	0.10	0.02	0.11	0.04	0.21	0.06	0.06	0.07	0.03	0.09	0.15	0.06
Mg# <sup>c</sup>	0.69	0.68	0.67	0.66	0.58	0.56	0.61	0.55	0.65	0.75	0.65	0.67	0.75
R <sup>2+</sup> <sup>d</sup>	4.75	4.66	4.74	4.57	4.79	4.41	4.74	4.70	4.74	4.80	4.59	4.57	4.79
<b>Calculated T (°C)</b>													
Bourdelle et al. (2013) <sup>e</sup>	422	236	494	245	393	152	284	309	267	415	246	188	300
Tcorrected (>350°C) <sup>e</sup>	343		367		332					340			

1622

1623

Sample	218c	218c	218c	218c	218c	218c	218c	218c	218c	218c	218c	218c	218c	218c	218c	218c	218c	218c	218c	218c	218c	218c	
Clast vs matrix	Clast	Clast	Clast	Clast	Clast	Clast	Clast	Clast	Clast	Clast	Clast	Clast	Clast	Clast	Clast	Clast	Clast	Clast	Clast	Clast	Clast	Clast	Clast
Analysis #	33 / 1	38 / 1	39 / 1	40 / 1	41 / 1	42 / 1	101 /	102 /	103 /	103 /	103 /	103 /	103 /	103 /	103 /	103 /	103 /	103 /	103 /	103 /	103 /	104 /	
<b>Chlorite composition <sup>a</sup></b>																							
SiO <sub>2</sub>	28.75	28.61	28.38	28.00	28.29	28.44	27.80	28.02	27.66	27.81	28.39	28.56	27.99	28.37	28.54	28.60	28.45	27.75	28.02	28.96	28.54	30.11	
TiO <sub>2</sub>	0.14	0.02	0.03	0.67	0.05	0.08	0.04	0.04	0.03	0.00	0.06	0.03	0.07	0.10	0.06	0.14	0.06	0.09	0.17	0.39	0.08	0.02	
Al <sub>2</sub> O <sub>3</sub>	18.97	18.75	19.48	19.58	19.71	19.08	19.25	18.25	19.14	19.10	19.93	18.93	19.01	19.32	19.88	19.38	19.07	19.85	19.33	19.66	19.59	18.50	
Cr <sub>2</sub> O <sub>3</sub>	0.41	0.01	0.00	0.02	0.03	0.03	0.33	0.19	0.29	0.18	0.11	0.13	0.00	0.08	0.00	0.04	0.04	0.17	0.00	0.10	0.09	0.12	
FeO	19.01	18.52	17.89	16.44	17.60	19.25	20.10	20.73	19.67	18.92	18.31	19.41	19.11	19.49	19.89	19.64	20.55	18.36	19.79	19.49	20.95	13.56	
MnO	0.22	0.26	0.27	0.17	0.26	0.21	0.27	0.31	0.28	0.31	0.28	0.22	0.22	0.30	0.35	0.27	0.18	0.17	0.21	0.26	0.34	0.28	
MgO	20.59	20.17	21.41	22.15	21.14	19.97	19.22	19.21	18.95	19.65	19.58	19.23	19.61	18.82	19.43	19.90	18.89	20.27	18.44	19.42	18.63	24.56	
NiO	0.17	0.07	0.12	0.06	0.08	0.13	0.09	0.04	0.11	0.13	0.05	0.03	0.09	0.00	0.00	0.16	0.09	0.05	0.05	0.08	0.07	0.14	
CaO	0.13	0.05	0.04	0.05	0.06	0.07	0.06	0.05	0.05	0.06	0.09	0.09	0.08	0.06	0.09	0.12	0.10	0.09	0.20	0.25	0.11	0.05	
Na <sub>2</sub> O	0.02	0.04	0.00	0.01	0.04	0.02	0.09	0.02	0.03	0.04	0.00	0.04	0.00	0.05	0.00	0.00	0.00	0.05	0.05	0.03	0.03	0.03	
K <sub>2</sub> O	0.01	0.00	0.02	0.01	0.00	0.02	0.00	0.00	0.02	0.01	0.02	0.00	0.02	0.05	0.01	0.02	0.00	0.00	0.01	0.02	0.00	0.00	
total	88.41	86.49	87.62	87.16	87.26	87.28	87.24	86.87	86.22	86.20	86.82	86.67	86.22	86.65	88.23	88.26	87.43	86.79	86.26	88.67	88.46	87.36	
K <sub>2</sub> O+Na <sub>2</sub> O+CaO	0.16	0.09	0.05	0.07	0.10	0.10	0.15	0.08	0.10	0.11	0.11	0.13	0.11	0.16	0.10	0.14	0.10	0.09	0.25	0.30	0.17	0.07	
<b>Structural formula <sup>b</sup></b>																							
Si	2.90	2.94	2.87	2.83	2.87	2.91	2.86	2.91	2.88	2.88	2.90	2.94	2.90	2.92	2.89	2.90	2.92	2.84	2.91	2.91	2.90	2.98	
Ti	0.01	0.00	0.00	0.05	0.00	0.01	0.00	0.00	0.00	0.00	0.00	0.00	0.01	0.01	0.00	0.01	0.00	0.01	0.01	0.03	0.01	0.00	
Al	2.25	2.27	2.32	2.33	2.35	2.30	2.34	2.23	2.35	2.33	2.40	2.30	2.32	2.35	2.37	2.31	2.31	2.40	2.36	2.33	2.35	2.16	
Al <sup>IV</sup>	1.10	1.06	1.13	1.17	1.13	1.09	1.14	1.09	1.12	1.12	1.10	1.06	1.10	1.08	1.11	1.10	1.08	1.16	1.09	1.09	1.10	1.02	
Al <sup>VI</sup>	1.15	1.21	1.19	1.16	1.22	1.20	1.20	1.14	1.22	1.21	1.30	1.24	1.22	1.27	1.26	1.21	1.23	1.24	1.27	1.24	1.25	1.14	
Cr	0.03	0.00	0.00	0.00	0.00	0.00	0.03	0.02	0.02	0.01	0.01	0.01	0.00	0.01	0.00	0.00	0.00	0.01	0.00	0.01	0.01	0.01	
Fe	1.60	1.59	1.51	1.39	1.49	1.64	1.73	1.80	1.71	1.64	1.56	1.67	1.65	1.68	1.68	1.66	1.76	1.57	1.72	1.64	1.78	1.12	
Mn	0.02	0.02	0.02	0.01	0.02	0.02	0.02	0.03	0.02	0.03	0.02	0.02	0.02	0.03	0.03	0.02	0.02	0.01	0.02	0.02	0.03	0.02	
Mg	3.10	3.09	3.23	3.33	3.19	3.04	2.95	2.97	2.94	3.03	2.98	2.95	3.02	2.89	2.93	3.00	2.89	3.09	2.85	2.91	2.82	3.62	
Ni	0.01	0.01	0.01	0.00	0.01	0.01	0.01	0.00	0.01	0.01	0.01	0.00	0.01	0.00	0.00	0.01	0.01	0.00	0.00	0.01	0.01	0.01	
Ca	0.01	0.01	0.00	0.01	0.01	0.01	0.01	0.01	0.01	0.01	0.01	0.01	0.01	0.01	0.01	0.01	0.01	0.01	0.02	0.03	0.01	0.00	
Na	0.00	0.01	0.00	0.00	0.01	0.00	0.02	0.00	0.01	0.01	0.00	0.01	0.00	0.01	0.00	0.00	0.00	0.01	0.01	0.01	0.01	0.01	
K	0.00	0.00	0.00	0.00	0.00	0.00	0.00	0.00	0.00	0.00	0.00	0.00	0.00	0.01	0.00	0.00	0.00	0.00	0.00	0.00	0.00	0.00	
octahedral sum	5.94	5.93	5.97	5.91	5.95	5.93	5.96	5.97	5.94	5.95	5.89	5.91	5.93	5.89	5.92	5.93	5.92	5.94	5.89	5.87	5.91	5.94	
vacancies	0.06	0.07	0.03	0.09	0.05	0.07	0.04	0.03	0.06	0.05	0.11	0.09	0.07	0.11	0.08	0.07	0.08	0.06	0.11	0.13	0.09	0.06	
Mg# <sup>c</sup>	0.66	0.66	0.68	0.71	0.68	0.65	0.63	0.62	0.63	0.65	0.66	0.64	0.65	0.63	0.64	0.64	0.62	0.66	0.62	0.64	0.61	0.76	
R <sup>2+</sup> <sup>d</sup>	4.73	4.71	4.77	4.74	4.71	4.72	4.71	4.80	4.68	4.71	4.57	4.64	4.71	4.60	4.65	4.70	4.68	4.68	4.59	4.58	4.64	4.78	
<b>Calculated T (°C)</b>																							
Bourdelle et al. (2013) <sup>e</sup>	322	278	418	373	351	303	371	410	313	334	242	250	305	242	280	299	270	349	248	234	269	285	
Tcorrected (>350°C) <sup>e</sup>			341	323	314		323	338															

1624

1625

1626

1627

Sample	155	155	155	155	155	155	155	155	155	155	155	155	155	155	155	155	155	115	115	115
Clast vs matrix	Clast	Clast	Clast	Clast	Clast	Clast	Mat	Mat	Mat	Mat	Mat	Mat	Mat	Mat	Mat	Mat	Mat	clast	clast	clast
Analysis #	83 / 1	87 / 1	89 / 1	92 / 1	93 / 1	94 / 1	78 / 1	80 / 1	89 / 1	56 / 1	59 / 1	60 / 1	61 / 1	73 / 1	74 / 1	78 / 1	79 / 1	25 / 1	28 / 1	33 / 1
<b>Chlorite composition <sup>a</sup></b>																				
SiO <sub>2</sub>	30.66	28.34	28.78	26.99	26.58	27.52	27.14	27.31	28.80	29.88	27.78	26.30	28.12	26.37	26.72	26.72	26.64	28.14	31.06	30.62
TiO <sub>2</sub>	0.05	0.08	0.06	0.00	0.07	0.02	0.00	0.00	0.10	0.07	0.04	0.03	0.10	0.02	0.00	0.19	0.06	0.04	0.00	0.00
Al <sub>2</sub> O <sub>3</sub>	19.94	20.83	19.88	19.73	20.45	19.92	20.08	19.97	18.05	17.19	19.13	19.38	19.46	20.03	20.13	20.48	20.67	19.12	16.18	15.94
Cr <sub>2</sub> O <sub>3</sub>	0.50	0.00	0.00	0.20	0.04	0.06	0.18	0.04	0.02	0.61	0.00	0.00	0.00	0.07	0.02	0.07	0.04	0.05	0.00	0.08
FeO	21.27	17.35	15.81	23.87	26.12	22.39	24.36	22.95	23.72	21.24	25.96	27.42	24.31	28.69	28.29	24.56	26.33	17.71	17.14	16.92
MnO	0.33	0.15	0.12	0.14	0.25	0.21	0.31	0.26	0.20	0.43	0.14	0.20	0.16	0.14	0.21	0.22	0.25	0.23	0.25	0.11
MgO	14.43	20.71	22.77	15.71	15.33	17.69	15.54	16.93	17.11	16.92	14.25	14.09	14.37	12.71	13.27	14.93	13.45	21.41	22.53	22.31
NiO	0.06	0.04	0.03	0.00	0.00	0.12	0.02	0.02	0.00	0.12	0.07	0.00	0.04	0.03	0.05	0.01	0.08	0.09	0.10	0.06
CaO	0.26	0.05	0.08	0.07	0.05	0.03	0.07	0.05	0.11	0.15	0.08	0.04	0.10	0.06	0.08	0.03	0.04	0.12	0.32	0.38
Na <sub>2</sub> O	0.05	0.04	0.02	0.06	0.04	0.06	0.09	0.06	0.08	0.12	0.04	0.06	0.09	0.05	0.08	0.04	0.01	0.03	0.06	0.06
K <sub>2</sub> O	0.04	0.02	0.00	0.01	0.01	0.00	0.05	0.04	0.02	0.03	0.03	0.04	0.09	0.02	0.01	0.01	0.02	0.03	0.06	0.05
total	87.59	87.62	87.55	86.79	88.95	88.01	87.85	87.62	88.22	86.76	87.52	87.54	86.84	88.19	88.86	87.27	87.59	86.97	87.71	86.54
K <sub>2</sub> O+Na <sub>2</sub> O+CaO	0.36	0.12	0.10	0.15	0.10	0.09	0.21	0.14	0.22	0.30	0.14	0.13	0.27	0.13	0.17	0.08	0.07	0.18	0.44	0.49
<b>Structural formula <sup>b</sup></b>																				
Si	3.13	2.85	2.87	2.85	2.77	2.84	2.84	2.84	2.98	3.11	2.93	2.81	2.96	2.81	2.82	2.81	2.82	2.87	3.12	3.12
Ti	0.00	0.01	0.00	0.00	0.01	0.00	0.00	0.00	0.01	0.01	0.00	0.00	0.01	0.00	0.00	0.02	0.01	0.00	0.00	0.00
Al	2.40	2.47	2.34	2.45	2.51	2.42	2.47	2.45	2.20	2.10	2.38	2.44	2.42	2.51	2.50	2.54	2.58	2.30	1.92	1.91
Al <sup>IV</sup>	0.87	1.15	1.13	1.15	1.23	1.16	1.16	1.16	1.02	0.89	1.07	1.19	1.04	1.19	1.18	1.19	1.18	1.13	0.88	0.88
Al <sup>VI</sup>	1.53	1.32	1.21	1.30	1.28	1.26	1.31	1.28	1.18	1.21	1.31	1.25	1.38	1.32	1.31	1.35	1.39	1.16	1.04	1.03
Cr	0.04	0.00	0.00	0.02	0.00	0.01	0.01	0.00	0.00	0.05	0.00	0.00	0.00	0.01	0.00	0.01	0.00	0.00	0.00	0.01
Fe	1.81	1.46	1.32	2.11	2.27	1.93	2.13	1.99	2.05	1.85	2.29	2.45	2.14	2.55	2.49	2.16	2.33	1.51	1.44	1.44
Mn	0.03	0.01	0.01	0.01	0.02	0.02	0.03	0.02	0.02	0.04	0.01	0.02	0.01	0.01	0.02	0.02	0.02	0.02	0.02	0.01
Mg	2.19	3.10	3.39	2.47	2.38	2.72	2.42	2.62	2.64	2.62	2.24	2.24	2.26	2.02	2.08	2.34	2.12	3.25	3.37	3.38
Ni	0.00	0.00	0.00	0.00	0.00	0.01	0.00	0.00	0.00	0.01	0.01	0.00	0.00	0.00	0.00	0.00	0.01	0.01	0.01	0.01
Ca	0.03	0.01	0.01	0.01	0.01	0.00	0.01	0.01	0.01	0.02	0.01	0.01	0.01	0.01	0.01	0.00	0.00	0.01	0.03	0.04
Na	0.01	0.01	0.00	0.01	0.01	0.01	0.02	0.01	0.02	0.02	0.01	0.01	0.02	0.01	0.02	0.01	0.00	0.01	0.01	0.01
K	0.01	0.00	0.00	0.00	0.00	0.00	0.01	0.01	0.00	0.00	0.00	0.01	0.01	0.00	0.00	0.00	0.00	0.00	0.01	0.01
octahedral sum	5.65	5.91	5.95	5.93	5.97	5.95	5.93	5.95	5.92	5.82	5.88	5.98	5.83	5.93	5.94	5.89	5.88	5.98	5.93	5.93
vacancies	0.35	0.09	0.05	0.07	0.03	0.05	0.07	0.05	0.08	0.18	0.12	0.02	0.17	0.07	0.06	0.11	0.12	0.02	0.07	0.07
Mg# <sup>c</sup>	0.55	0.68	0.72	0.54	0.51	0.58	0.53	0.57	0.56	0.59	0.49	0.48	0.51	0.44	0.46	0.52	0.48	0.68	0.70	0.70
R <sup>2+</sup> <sup>d</sup>	4.04	4.58	4.72	4.59	4.67	4.68	4.58	4.64	4.71	4.51	4.55	4.71	4.41	4.59	4.60	4.52	4.48	4.79	4.84	4.84
<b>Calculated T (°C)</b>																				
Bourdelle et al. (2013) <sup>e</sup>	116	307	352	306	509	360	312	335	259	175	223	490	186	321	326	272	251			
T <sub>corrected</sub> (>350°C) <sup>e</sup>			315		371	318						365								





1632 **Table S3.** *In situ LA-ICP-MS trace element analysis (ppm) of 22 chlorite crystals from silicified samples.*

1633

<b>Sample</b>	195	195	195	195	155	155	155	155	155	155	155	218ab	218ab	218ab	218ab	218c	218c	218c	173	173	173
<b>Clast vs matrix</b>	clast	clast	clast	clast	clast	clast	matrix	matrix	clast	clast	matrix	clast	clast	matrix	matrix	clast	clast	matrix	matrix	matrix	matrix
<b>Analysis #</b>	Ch1	Ch2	Ch2-1	Ch3b	Ch1	Ch2	Ch3	Ch3-1	Ch4	Ch5	Ch6	Ch1	Ch2	Ch3	Ch4	Ch1	Ch2	Ch3	Ch1	Ch2	Ch3
<b>Ti (47)<sup>a</sup></b>	47 <sup>b</sup>	5289	49	116	188	-	3816	384	144	110	218	248	13	29	28	66	215	bdl	23	25	17
<b>Mn (55)</b>	2837	2720	2383	1985	3340	2319	241	267	2734	2733	525	386	75	93	48	485	1725	45	278	317	281
<b>Cr (53)</b>	41	311	249	108	1022	689	124	92	40	55	231	169	30	69	56	44	746	15	720	1662	1107
<b>Co (59)</b>	34	33	33	40	103	72	bdl	bdl	150	146	36	bdl	bdl	bdl	bdl	30	93	bdl	166	69	84
<b>Ni (60)</b>	183	179	180	202	549	401	28	29	482	604	83	101	25	27	12	110	368	bdl	2639	1330	1689
<b>Cu (63)</b>	19	20	bdl	bdl	bdl	bdl	bdl	bdl	bdl	bdl	bdl	bdl	bdl	bdl	bdl	bdl	38	bdl	280	202	15
<b>Zn (66)</b>	207	172	159	152	225	161	16	14	198	180	40	29	bdl	bdl	bdl	25	108	bdl	1216	865	905
<b>V (51)</b>	172	241	156	134	473	405	45	18	209	164	35	39	bdl	bdl	bdl	66	198	bdl	29	29	26

1634 Analyses carried out at GeoRessources (Nancy, France) with a 193 nm GeoLas Pro ArF Excimer laser (Microlas, Göttingen, Germany) coupled with beam  
 1635 homogenization optics. Analyzed with an Agilent 7500c Quadrupole ICP-MS (Agilent, Santa Clara, USA) equipped with an octopole reaction system with  
 1636 enhanced sensitivity optional lenses (Cs type; Agilent). Internal standard: <sup>28</sup>Si, calibrated from the mean value of several chlorite microprobe analyses.

1637 <sup>a</sup> Element analyzed (isotope)

1638 <sup>b</sup> Concentrations in ppm calibrated against the NIST SRM 610 silica glass reference using values given in Pearce et al. (1997). Absolute concentrations (ppm)  
 1639 calculated from equations in Longerich et al. (1996).

1640

1641

1642

1643

1644 **Table S4.** Temperature of chlorite formation calculated from composition ( $R^{2+}$  and Si) of chlorite in equilibrium with quartz, with the thermometer  
 1645 of Bourdelle et al. (2013) for chlorites from matrix, clasts and both, in silicified samples.  
 1646

T (°C) in matrix and clasts	195	155	218ab	218c	173
Mean T	250	265	291	294	276
Median T	244	273	303	301	257
Minimum T	156	113	152	234	140
Maximum T	350	492	402	349	452
Standard deviation	49	88	61	36	75
Number of analyses	46	40	36	22	14
T (°C) in matrix	195	155	218ab	218c	173
Mean T	244	275	269		287
Median T	236	272	284		234
Minimum T	156	175	152		223
Maximum T	350	365	340		452
Standard deviation	48	63	64		96
Number of analyses	37	11	9		5
T (°C) in clasts	195	155	218ab	218c	173
Mean T	272	262	298	294	270
Median T	269	273	313	301	258
Minimum T	197	113	194	234	140
Maximum T	332	492	402	349	361
Standard deviation	50	96	59	36	66
Number of analyses	9	29	27	22	9

1647